A SYSTEM DYNAMICS MODELING METHODOLOGY FOR COMPRESSIBLE FLUID FLOW SYSTEMS WITH APPLICATIONS TO INTERNAL COMBUSTION ENGINES

DISSERTATION

Presented in Partial Fulfillment of the Requirements for the Degree Doctor of Philosophy

in the Graduate School of The Ohio State University

By

Kenneth Michael Follen, M.S.

Graduate Program in Mechanical Engineering

The Ohio State University

2010

Dissertation Committee:

Prof. Giorgio Rizzoni, Adviser

Prof. Yann Guezennec, Co-Advisor

Prof. Steve Yurkovich

Prof. Junmin Wang

Dr. Marcello Canova

Dr. Shawn Midlam-Mohler

ABSTRACT

The ability to develop physically consistent lumped-parameter models of compressible flow systems is a relevant and important aspect of designing control strategies for energy conversion systems. Such models can lead to a better system-level understanding of internal combustion engines, turbomachinery, fuel cell systems, Heat Ventilation and Air Conditioning (HVAC) and refrigeration systems. Furthermore, the models may be used for control systems development, optimization and validation leading to better performance and lower development costs. While improvements in computing technology have made it possible to use Computational Fluid Dynamic (CFD) simulations in a wide range of applications, 3-D and 1-D codes are not immediately useful in the design of control algorithms due to their complexity and high computational cost. However, the prediction of unsteady phenomena, particularly the characterization of pressure, temperature, velocity and flow rate at different locations of the system, is critical for several applications, ranging from design, and optimization, to control and diagnostics. The focus of the current research is to fill the void between the high-fidelity numerical simulation models originating from partial differential equations, and low-fidelity, control-oriented empirical models based on lumped parameter approximations such as are used today in industrial applications. The outcome of the research includes

two novel approaches for modeling compressible fluid systems for dynamic systems applications. The two methodologies have been developed to retain a high level of fidelity while preserving the simple structure and limited computation time of lumped-parameter models. The two approaches have been validated against a combination of experimental, analytical and high fidelity simulation results. The results validate that the two modeling techniques enable accurate, computationally efficient models suitable for control systems applications.

A.M.D.G.

ACKNOWLEDGMENTS

Thanks and acknowledgements are owed to a number of people and institutions, without whom this research would not have been possible. I would like first thank my advisors, Prof. Rizzoni and Prof. Guezennec for their support, enthusiasm and the opportunities they have provided for me. I would also like to thank the Center for Automotive Research and its community for their support and expertise. Two such gentleman, Dr. Marcello Canova and Dr. Shawn Midlam-Mohler have been instrumental in not only this research, but also in my total academic development and deserve more thanks and credit than can be listed in this short section. I would also like to thank Dr. Byungho Lee, Dr. Greg Matthews and General Motors for providing me generous support, technical guidance, expertise and an interesting research topic to pursue. I would like to thank the National Science Foundation for its generous support. Many thanks are owed to my fiancé and friends for their support, encouragement and understanding over this tenure. I would like to thank my family, particularly my parents for bestowing upon me the importance of, and providing me the opportunity to pursue higher education and to have a genuine love of learning.

VITA

May 19, 1983 ……. Born – Middleburg Heights, Ohio

June, 2005 …….. B.S. Mechanical Engineering,
The Ohio State University

August, 2007……..…. M.S. Mechanical Engineering,
The Ohio State University

September, 2005 to August 2010 ……..…. Graduate Research Associate,
The Ohio State University
Center for Automotive Research

PUBLICATIONS

Research Publications

1. K. Follen, M. Canova, S. Midlam-Mohler, Y. Guezennec, G. Rizzoni, B. Lee, G. Matthews, “A High Fidelity Lumped-Parameter Engine Model for Powertrain Control Design and Validation” ASME Dynamic Systems and Control Conference, 2010.

2. K. Follen, S. Midlam-Mohler, Y. Guezennec, F. Rinaldi, “Diesel Particulate Filter Regeneration with External Burner” Global Powertrain Conference, 2006.

3. D. Morr, J. Wiechel, C. Tanner, A. Bartsch, J. Bookwalter, K. Follen, A. Ratliff “Linear and Angular Accelerations of the Head During Activities of Daily Living. Part 1: Instrumentation and Methodology” Injury Biomechanics Research, 32nd International Workshop, 2005.

FIELDS OF STUDY

Major Field: Mechanical Engineering

TABLE OF CONTENTS

Page

LIST OF TABLES

Table Page

LIST OF FIGURES

NOMENCLATURE

SYMOBOLS

A	Area
a	Crank radius
C_d	Discharge coefficient
c_v	Specific heat
c	Speed of sound
h	Enthalpy per unit of mass
l	Connection rod length
J	Crankshaft inertia
m	Mass
$\dot{m}$	Mass flow
n	Engine speed
P	Pressure
Q_{LHV}	Lower heating value
$\dot{Q}$	Heat transfer rate
R	Gas constant
T	Temperature
u	Specific internal energy
v	Velocity
V	Volume
X	Mass fraction
$\dot{W}$	Rate of work
γ	Ratio of specific heats
η_v	Volumetric efficiency
ε	Wrist pin offset
θ	Crank angle
ρ	Density
θ	Crank angle

SUBSCRIPTS

1*D*	1-D simulation result
0	Ambient
air	Air
cyl	Cylinder
d	Displaced
ev	Exhaust valve
ex	Exhaust
f	Fuel
ht	Heat transfer
i	Indicated
im	Intake manifold
in	In
ip	Intake port
iv	Intake valve
ind	Indicated
IVC	Intake valve closing
IVO	Intake valve opening
l	Load
out	Out
p	Piston
th	Throttle

CHAPTER 1

INTRODUCTION

1.1 Motivation

Increasing demands for improved vehicle fuel economy and stringent government regulations provide an impetus for the development of complex engine architectures to meet the wide array of demands and standards. As the number of systems and components increase within a vehicle's powertrain, so does the complexity in coordinating system interactions, optimization of components and parameters and the development of the overall control system. Such complexity yearns for the development of simple, computationally efficient engine models to lighten the burden of costly hardware iterations and intensive experimental testing.

Specifically, the prediction of the thermodynamics and fluid dynamics in internal combustion engine gas flow systems under unsteady conditions is acquiring increasing importance for several reasons. First, optimization of engine volumetric efficiency is critical to optimize torque and power performance. In addition, the estimation of the trapped air mass inside the cylinder is essential to the derivation of robust air-fuel ratio

control laws, which in turn have significant effects on fuel economy, in-cylinder pollutant formation, and effectiveness of the catalytic conversion. Furthermore, the increasing role of boosting (turbo- and super-charging) as an aid in reducing engine displacement, poses further issues to the characterization, optimization and control of the engine air path.

It is well understood that such gains can only be achieved if improvements in engine design can be matched by the ability to closely control engine breathing and combustion performance. The ability to predict engine flows through low-order, physically based system dynamics models is therefore of critical importance to the development of model-based control algorithms that can be easily adapted to different engine platforms. Such models can lead not only to better fuel economy and emissions control, but can also significantly shorten the development of new engines, as well as to enable model-based control and diagnostic approaches. It is with these thoughts in mind that the research outlined in the following section has been carried out, with the objective of developing high fidelity, yet computationally efficient models to aid in coordinating, optimizing and controlling the increasingly complex engines that power our vehicles.

1.2 Thesis Overview

Within the world of modeling there are many paths. In focusing on internal combustion engines for performance and control-related applications, the modeler has the choice of a number of approaches ranging in fidelity and computational requirement to describe the torque, speed and subsequent dynamics of the system. Pertinent to these

applications is ability to describe the physics of the charge entering the engine's ducting, its combustion and its eventual expulsion from the system. A major underlying phenomenon governing these dynamics is the flow a compressible fluid through a system of interconnected ducts, plenums, resonators, and volumes.

The first step in the development of control oriented models of the gas exchange process within internal combustion engines is the evaluation of the state of the art. This analysis begins in Chapter Two with the fundamental equations describing compressible fluid systems. Different levels of fidelity are explored, ranging from three-dimensional models down to zero-dimensional representations. The governing equations of the different levels of models are presented, along with their application to internal combustion engines. The one- and zero-dimensional modeling methodologies presented in Chapter 2 are further analyzed and evaluated in a case study in the third chapter. The case study evaluates the accuracy and fidelity of the techniques as benchmarked against experimental data. The results of this case study outline that the one-dimensional and zero-dimensional cycle-resolved modeling techniques are well suited for their respective applications. However, a fundamental gap (in both fidelity and computation time) exists between these two methodologies. The zero-dimensional, crank-angle-resolved modeling technique could fill this void, save for its inability to predict wave dynamic effects. This deficiency is analyzed in Chapter Four and shown to have detrimental effects on gas exchange modeling. A novel empirical approach is presented in Chapter Four to capture the distributed effects not inherently modeled within the zero-dimensional structure. The

resulting model is suitable for control systems design applications requiring crank-angle-resolved cylinder pressure and torque fluctuations within a computationally efficient architecture.

Chapters Five and Six outline a second novel approach to fill the void between the one-dimensional and the zero-dimensional cycle-resolved models. This approach begins from the governing partial differential equations and applies a model order reduction technique to reduce the system to a low order set of ordinary differential equations. This modeling technique has the advantage of inherently predicting distributed effects, as opposed to data intensive empirical calibration. The methodology is evaluated against case studies selected to mimic engine intake and exhaust systems. The results are benchmarked against a combination of analytic and high fidelity numerical simulation results and shown to accurately model wave propagation effects within a control oriented model.

This dissertation contributes to the modeling and control community through identifying a void between one-dimensional and zero-dimensional cycle-resolved engine models and proposing two novel approaches to fill this void. The first employs empirical techniques to improve upon traditional zero-dimensional crank-angle-resolved models. The second presents a formal model order reduction approach for the development of a high-fidelity system dynamics approach for compressible fluid systems. The two approaches allow for the development of accurate, computationally efficient crank-angle-resolved engine models suitable for control systems design.

CHAPTER 2

THERMODYNAMICS AND FLUID DYNAMICS OF COMPRESSIBLE FLUID FLOW SYSTEMS

2.1 Introduction

The time evolution of a fluid flow system may be described in entirety through laws governing the conservation of three quantities: mass, momentum, and energy. These conservation laws, generally nonlinear in nature, take the form of partial differential equations and exemplify mathematically the following statement [16]:

> *The variation of the total amount of a quantity U inside a given domain is equal to the balance between the amount of that quantity entering and leaving the considered domain, plus the contributions from the eventual sources generating that quantity.*

The most general form of these equations as applied to viscous fluids includes that of the First Law of Thermodynamics, the Continuity equation and the Navier-Stokes equations. Under the approximation of an inviscid fluid, this equation set is known as the Euler equations. In the sections that follow, a review of mathematical modeling of

compressible fluid systems is presented, with a concentration on the governing equations, solution methodologies and applications to internal combustion engine modeling. Specific focus is placed upon models suitable for controls design, optimization and evaluation. However, for completeness, (while not specifically suited for controls design) the governing equations are presented starting from the most general three-dimensional form and reduced to one- and zero-dimensional formulations.

2.2 Fundamental Equations and their Application to Internal Combustion Engines

The equations governing compressible fluid systems may be formulated based upon numerous approximations, depending upon the desired application. Specifically, the governing equations may be cast as steady or unsteady, viscous or inviscid, multi- or zero-dimensional, and may describe a real or ideal gas. The unsteady equations are applicable for describing time varying phenomena, while the steady equations are reserved for applications where only the steady state solution is desired, resulting in a greatly simplified model structure. In systems where the viscosity and thermal conductivity of the fluid are significant, the phenomena of turbulence and shear stresses must be described through the viscous form of the equations. For situations where the fluid is sufficiently dilute for the internal stress to be ignored, the inviscid assumption may be employed. For the application of interest, gas exchange modeling within internal combustion engines, the equations will be presented starting from the most generally applicable form: unsteady, multi-dimensional, inviscid flow.

2.2.1 Fundamental Equations in Three Dimensions

The most general description of fluid flow is described by the unsteady conservation laws in three dimensions. For representation of these equations, an Eulerian approach has been chosen as shown in Figure 1.

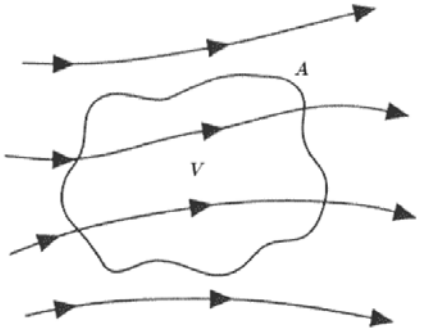

Figure 1: Eulerian Control Volume [9]

The control volume is fixed in space with the fluid travelling through the volume. Derivation of these equations can be found in standard fluid dynamic textbooks [129,9,11], with the resulting equations reiterated here for convenience.

2.2.1.1 Continuity Equation

The first and most intuitive of the three conservation laws is the continuity equation, which is simply a mathematical representation of the principle that mass can neither be created nor destroyed [11,16]. Under the assumption of chemically non-reacting

flow, the general integral form of the conservation equation is shown in (2.1), and is equally applicable to all flows, compressible or incompressible, viscous or inviscid [11,16].

$$\frac{\partial}{\partial t}\iiint_V \rho dV + \oiint_S \rho \vec{u} \bullet d\vec{S} = 0 \tag{2.1}$$

The above expression states that the time rate of change of mass within a control volume $\left(\frac{\partial}{\partial t}\iiint_V \rho dV\right)$ is equal to the net mass flow through the surface of the control volume $\left(\oiint_S \rho \vec{u} \bullet d\vec{S}\right)$ [11].

2.2.1.2 Momentum Equation

The second conservation law describes the unsteady nature of the specific momentum (product of density and velocity) within a control volume and is an application of Newton's second law [129,11,16]. The conservation of momentum is a mathematical representation of the statement that the time rate of change of momentum within a control volume is equal to the net forces exerted on it [11,16]. These forces may be categorized as *body* forces and *surface* forces. The body forces encompass those forces that act on the fluid inside of the control volume, such as gravitational and electromagnetic forces [11]. Surface forces, on the other hand, describe forces that act on the boundary of the control volume, such as pressure and shear stresses [11]. In the realm of viscous flows, it is important to characterize the shear stress. However, under the

assumption of inviscid flow, the shear stresses may be ignored, leaving only the surface force due to pressure. Summing up the body forces $\left(\iiint_V \rho \vec{f}_{body} dV - \iint_S P \cdot d\vec{S} \right)$, the unsteady momentum within the control volume $\left(\frac{\partial}{\partial t} \iiint_V \rho \vec{u} dV \right)$ and the flux of momentum through the surface $\left(\iint_S \rho \vec{u} \left(\vec{u} \bullet d\vec{S} \right) \right)$, yields the unsteady momentum equation for inviscid flows, shown in equation (2.2) [11].

$$\frac{\partial}{\partial t} \iiint_V \rho \vec{u} dV + \iint_S \rho \vec{u} \left(\vec{u} \bullet d\vec{S} \right) = \iiint_V \rho \vec{f}_{body} dV - \iint_S P \cdot d\vec{S} \tag{2.2}$$

2.2.1.3 Energy Equation

The final conservation law describes the dynamic nature of energy within the control volume and is a mathematical representation of the first law of thermodynamics applied to a fluid flowing through a fixed control volume [11]. This law states that energy can neither be created nor destroyed, but can only change form [10]. This statement is exemplified in equation (2.3), where the time rate of change of energy within a control volume $\left(\frac{\partial}{\partial t} \iiint_V (\rho e_0) dV \right)$ is shown to balance the net flux of energy through the surface $\left(\iint_S \rho e_0 \vec{u} \bullet d\vec{S} \right)$, the net rate of heat added from the surroundings $\left(\iiint_V \dot{q} \rho dV \right)$ and the rate

of work done on the fluid inside the control volume due to pressure and body forces $\left(\iiint_V \rho\left(\vec{f}\bullet\vec{u}\right)dV - \oiint_S p\vec{u}\cdot d\vec{S} \right)$ [11].

$$\frac{\partial}{\partial t}\iiint_V \left(\rho e_0\right)dV + \oiint_S \rho e_0 \vec{u}\bullet d\vec{S} = \iiint_V \dot{q}\rho dV - \oiint_S P\vec{u}\cdot d\vec{S} + \iiint_V \rho\left(\vec{f}\bullet\vec{u}\right)dV \qquad (2.3)$$

2.2.1.4 Constitutive Relations

A cursory analysis of the aforementioned conservation laws will show that the equation set constitutes five equations in six unknown quantities, and thus is an under-determined equation set. For closure and the existence of a unique solution, constitutive relations are required. These relations are generally algebraic in nature and specific to the application at hand. The first form of the constitutive relations is the equation of state, which specifies the type of fluid being modeled [17]. Under the temperatures and pressures generally encountered in compressible, inviscid flow, gas particles are widely separated, encouraging the intermolecular forces to be ignored [11]. Under this approximation, the equation of state can be taken as the ideal gas law:

$$P = \rho RT \qquad (2.4)$$

Equation (2.4) introduces additional variables, and thus additional relations are required to define the thermodynamic states of the system. For an equilibrium

chemically reacting mixture of an ideal gas, the thermodynamic states (internal energy, enthalpy) are a function of both the temperature and the pressure.

$$\begin{aligned} e &= e(T, P) \\ h &= h(T, P) \end{aligned} \tag{2.5}$$

Under the assumption of a non-chemically reacting perfect gas, it is sufficient for the thermodynamic properties to be assumed to be functions of temperature alone, and the system is said to be a thermally perfect gas [11]:

$$\begin{aligned} e &= e(T) \\ h &= h(T) \\ de &= c_v dT \\ dh &= c_p dT \end{aligned} \tag{2.6}$$

Furthermore, in applications where the pressure and temperature variations are sufficiently moderate, the specific heats may be defined as constant leading to a system of a calorically perfect gas [11]:

$$\begin{aligned} e &= c_v T \\ h &= c_p T \end{aligned} \tag{2.7}$$

The applicability of these approximations in the equation of state (real versus ideal) and thermodynamic properties, is very much application dependent and should be considered carefully prior to selection.

2.2.1.5 Solution Methodology and Applications

The system of conservation laws in three dimensions, together with the equation of state, constitutes a fully coupled, unsteady set of partial differential equations. The nonlinear nature of the equations can result in significant difficulties in generating numerical solutions. The dominant nonlinearity provided by the convection term within the momentum equation is responsible for the presence of spontaneous instabilities in flow, also known as turbulence [16]. Furthermore, the nonlinear products of density and velocity allow for the existence of discontinuities in the solutions of velocity, pressure and temperature, known as shock waves [16]. These difficulties, coupled with the significant order required to model three-dimensional flows, results in an extremely complex and computational intense numerical algorithm.

Several solution methodologies have been presented to tackle these complex equations, ranging in complexity and computational requirement and include the techniques of (in decreasing computational complexity): Direct Numerical Simulation (DNS), Large Eddy Simulation (LES) and the Reynolds Averaged Navier-Stokes (RANS) approach. The DNS algorithm targets the full time dependent conservation laws and aims to capture the large scale turbulent fluctuations and a portion of the small scale turbulent motion [16]. The next level of approximation includes the LES, where turbulent fluctuations are simulated directly, but restricted to larger time scales [16]. The model is based upon a filtered version of the conservation laws, where the equations are averaged over the portion not directly computed [16]. Yet one step down from this is the RANS

model, where only the averaged turbulent flow is calculated and remains one of the most widely used approaches [16].

While not applicable for control system design applications, three-dimensional simulation techniques have been employed within internal combustion engine research activities for simulation and analysis of intake port and cylinder assemblies [34], flow junctions [35], as well as for the simulation of full intake-cylinder-exhaust systems [31]. Such simulations utilize a numerical mesh in excess of 30,000 grid points, and require computation times on the order of days [31]. While both proprietary and commercially available 3-D software packages [33,31] are available, the computational requirements render such simulations inappropriate for control systems design applications, and thus attention is turned to one and zero-dimensional modeling methodologies.

2.2.2 Fundamental Equations in One Dimension

With the high level of complexity and computational requirement of the three-dimensional models in mind, the advantages of simplification to a one-dimensional scheme are intuitive. In true one-dimensional flow, however, the flow field variables are a function of the flow direction (x) alone, and thus true one-dimensional flow is restricted to constant area applications [11]. This stringent limitation may be alleviated in situations where the spatial area variation is gradual, permitting the assumption that the flow properties are uniform across any cross section.

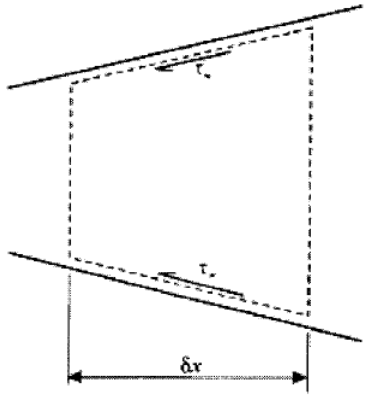

Figure 2: Control Volume for One-Dimensional Flow. Adapted from [12]

Such flow is defined as quasi-one-dimensional [11], and often supplemented with empirical or semi-empirical relations to capture the inherently multi-dimensional phenomena (such as abrupt area changes, frictional and heat transfer losses) within the quasi-one-dimensional model [12]. In the following sections, the three-dimensional equations described in Section 2.2.1 are reduced to the one-dimensional form through the assumption that the flow variables vary in only the flow direction. Furthermore, the equations are converted to their conservative differential form for ease of manipulation and application to numerical solution techniques. Note that the equations are presented for one-dimensional, inviscid flow with spatial area variation in the presence of frictional and heat transfer losses.

2.2.2.1 Continuity Equation

An equivalent form of the three-dimensional continuity equation from (2.1) is shown in (2.8), where the integral form has been converted to the conservative differential form [16,12].

$$\frac{\partial \rho}{\partial t} + \frac{\partial (\rho u_x)}{\partial x} + \frac{\partial (\rho u_y)}{\partial y} + \frac{\partial (\rho u_z)}{\partial z} = 0 \tag{2.8}$$

Assuming that the flow properties vary only in the flow direction (*i.e.* the partial derivatives with respect to x and y are zero), equation (2.8) reduces to the form in (2.9):

$$\frac{\partial \rho}{\partial t} + \frac{\partial (\rho u)}{\partial x} = 0 \tag{2.9}$$

In order to accurately account for gradual area variation within the one-dimensional context, (2.9) should be converted to the strong conservative form to yield [12,18]:

$$\frac{\partial (\rho A)}{\partial t} + \frac{\partial (\rho A u)}{\partial x} = 0 \tag{2.10}$$

An alternative conservative representation is often presented as [12,18]:

$$\frac{\partial \rho}{\partial t} + \frac{\partial (\rho u)}{\partial x} + \frac{\rho u}{A}\frac{dA}{dx} = 0 \tag{2.11}$$

2.2.2.2 Momentum Equation

The momentum equation previous shown in three-dimensional, integral representation in (2.2), is shown in (2.12) in the equivalent conservative differential form [12,16].

$$\begin{aligned}
&\frac{\partial(\rho u_x)}{\partial t}+\frac{\partial\left(\rho u_x{}^2+P\right)}{\partial x}+\frac{\partial\left(\rho u_x u_y\right)}{\partial y}+\frac{\partial\left(\rho u_x u_w\right)}{\partial z}+\rho f_x=0\\
&\frac{\partial\left(\rho u_y\right)}{\partial t}+\frac{\partial\left(\rho u_x u_y\right)}{\partial x}+\frac{\partial\left(\rho u_y{}^2+P\right)}{\partial y}+\frac{\partial\left(\rho u_y u_w\right)}{\partial z}+\rho f_y=0\\
&\frac{\partial\left(\rho u_w\right)}{\partial t}+\frac{\partial\left(\rho u_x u_z\right)}{\partial x}+\frac{\partial\left(\rho u_y u_z\right)}{\partial y}+\frac{\partial\left(\rho u_z{}^2+P\right)}{\partial z}+\rho f_z=0
\end{aligned} \tag{2.12}$$

Equation (2.12) can be converted to the one-dimensional conservative differential form through again assuming that the flow properties vary only in the flow direction to yield equation (2.13) [12,16,18].

$$\frac{\partial(\rho u)}{\partial t}+\frac{\partial\left(\rho u^2+P\right)}{\partial x}+\rho f=0 \tag{2.13}$$

Again, this form can be modified to include the affect of gradual area variation, to yield [12,18]:

$$\frac{\partial(\rho A u)}{\partial t}+\frac{\partial\left(\rho A u^2+PA\right)}{\partial x}-P\frac{\partial A}{\partial x}+\rho f A=0 \tag{2.14}$$

The force f may be defined as the shear forces acting on the control volume due to friction and can be modeled through (2.15), where f denotes the wall friction coefficient, a parameter determined through empirical relations [12].

$$f_{body} = \frac{1}{2} u|u| f \frac{4}{D} \tag{2.15}$$

An alternative conservative representation of the momentum equation is sometimes presented as [18]:

$$\frac{\partial(\rho A u)}{\partial t} + \frac{\partial(\rho A u^2)}{\partial x} + A\frac{\partial P}{\partial x} + \rho f_{body} A = 0 \tag{2.16}$$

2.2.2.3 Energy Equation

The energy equation shown in (2.3) can be converted to conservative differential form as shown in (2.17), where the work done on the control volume due to external forces is assumed to be zero [12,16,18].

$$\frac{\partial(\rho e_0)}{\partial t} + \frac{\partial\left[u_x(\rho e_0 + P)\right]}{\partial x} + \frac{\partial\left[u_y(\rho e_0 + P)\right]}{\partial y} + \frac{\partial\left[u_z(\rho e_0 + P)\right]}{\partial z} - \dot{q}\rho = 0 \tag{2.17}$$

Equation (2.17) can be converted to one-dimensional conservative differential form in a similar manner as the continuity and momentum equations, to yield [18]:

$$\frac{\partial(\rho e_0)}{\partial t} + \frac{\partial\left[u(\rho e_0 + P)\right]}{\partial x} - \dot{q}\rho = 0 \tag{2.18}$$

Including the effect of slight area variation, (2.18) is modified to yield [12,18]:

$$\frac{\partial(\rho A e_0)}{\partial t} + \frac{\partial\left[uA(\rho e_0 + P)\right]}{\partial x} - \dot{q}\rho A = 0 \tag{2.19}$$

An alternative expression can be developed through the definition of the total enthalpy $\left(h_0 = e_0 + \frac{P}{\rho}\right)$ to yield:

$$\frac{\partial(\rho A e_0)}{\partial t} + \frac{\partial(\rho A u h_0)}{\partial x} - \dot{q}\rho A = 0 \tag{2.20}$$

Additionally, the equation of state and thermodynamic properties should be specified as described in Section 2.2.1.4.

2.2.2.4 Solution Methodology and Applications

The one-dimensional conservation laws described in the previous section constitute a set of hyperbolic partial differential equations, requiring numerical techniques for solution. Notable contributions to this end include the Method of Characteristics (MOC) [87], and the Mesh Method of Characteristics [80,81,13]. The MOC is based upon converting the governing partial differential equations to ordinary differential equations and solving along the characteristic and path lines [13]. The Method of

Characteristics as applied to engine gas exchange modeling was used primarily in the 1960s-1980s [12,13,80,81]. As the method has difficulties in modeling large pressure wave propagation, as well in assuring conservation of primary variables, its popularity has been overtaken by the finite difference and finite volume methods.

The finite difference method begins from the differential form of the conservation laws and is based upon a truncation of the Taylor series expansion to approximate space and time derivatives [16]. The finite volume method is based upon the integral formulation of the conservation laws [16]. Where the finite difference method assigns states at mesh points, the finite volume method defines the states as cell averages within a volume [16]. These two methodologies have been shown to be more accurate and faster than the Method of Characteristics, and have the advantage of being inherently conservative with respect to mass and energy [12].

The finite difference and finite volume methods are further classified with respect to their spatial discretization method. Two notable approaches include the Adaptive (or Upwind) scheme and the Centered scheme. In particular, adaptive or upwind schemes denote a scheme where the flux leaving a control volume is a function of more points in the upwind direction of the flux location than the downwind direction [17]. A common form of the adaptive schemes is the first order upwind scheme where it is assumed that the flux leaving the control volume is a function of the state at the center of the volume. In the situation of wave direction reversal, the upwind scheme must become adaptive and modify which states are used in the computation of the flux since the upwind and

downwind directions have interchanged [17]. First order upwind methods provide a simple spatial discretization method, but are prone to smearing and dissipation due to the presence of a numerical diffusion inherent to the spatial discretization [15].

Conversely, a centered scheme employs an equal number of states upstream and downstream of the flux location in the computation of the flux [17]. The most popular form of centered schemes is the class of second order methods, which employ one state directly upstream and one state directly downstream of the flux location in the computation of the flux. While second order methods provide more accuracy in smooth solutions than that of first order upwind methods, a common deficiency of second order methods is the presence of spurious oscillations as a result of numerical dispersion inherent to the spatial discretization [15].

The solvers most commonly implemented are the second order two-step Lax-Wendroff method [88] or the MacCormack predictor-corrector method [89]. Due to the spurious oscillations present in these second order methods, flux averaging is generally employed [17]. Flux averaging is performed by combining first order and second order methods through flux liming, flux correcting or self adjusting hybrid methods [17]. The current trend is to employ a flux or slope limiter to allow for a shock capturing method and may also satisfy a nonlinear stability constraint [17]. In the presence of large gradients, these methods will reduce to first order [17]. An added complication in the case of the Euler equations is the presence of multiple wave speeds. In the case of subsonic flow, two of the wave speeds will be traveling in opposite directions, rendering it difficult

to determine the upwind direction. The schemes must then employ the use of either flux vector (or wave speed) splitting or Riemann solvers to determine the direction of propagation of information for the adaptive component of the flux [17]. Ultimately, these techniques operate a discretization of the PDEs on a pre-established grid, resulting in a set of nonlinear algebraic equations solved iteratively. It is worth mentioning that, even with numerical solvers, the Method of Characteristics is still commonly used for the satisfactory treatment of both simple and complex boundary conditions [12,13].

A critical aspect for the stability of these methods is that, at each mesh point, the domain of dependence of the PDEs must lie within the domain of dependence of the numerical scheme, which limits the choice of the discretization time step Δt and length Δx. The necessary condition (but not sufficient) for stability is given by the Courant-Friedrichs-Lewy stability criterion, where CFL is the criterion for stability [90]:

$$\left(a+|u|\right)\frac{\Delta t}{\Delta x} < CFL \tag{2.21}$$

Both commercially available [32,38] and proprietary [83] gas dynamic models based upon these approaches have been used in literature for detailed engine simulation and for engine control applications. A number of research studies have invoked the use of one-dimensional codes to engine simulation studies [91,92,93,94,74,37]. Arsie *et. al.* [37] have integrated the commercially available 1-D simulation code Wave by Ricardo North America [38] with Matlab/Simulink to simulate the unsteady gas flow in the intake and exhaust systems as well as for combustion studies. Furthermore, a number of research

activities have made use of the GT Power simulation software. Stobart [93] and Bromnick [94] have integrated GT Power and Matlab/Simulink for the purpose of control system design into an environment named CPower. In this simulation environment, GT Power was used for engine simulation and the outputs of the simulation were passed to Simulink through a "wiring harness" where Simulink was used to determine the control action [93]. The CPower environment has been shown to be applicable for diesel engine fuel injection and EGR control [93], as well as for SI engine applications of model predictive control of idle speed [94].

It is clear that the fidelity of the one-dimensional simulation technique is sufficient for gas exchange modeling and performance based control development, though the main shortcomings include the complexity and computational burden.

2.2.3 Approximations of One Dimensional Equations

The one-dimensional Euler equations presented in the previous section are instrumental in engine performance and control design applications due to their balance between fidelity and complexity. However, their nonlinear nature prohibits the derivation of a general analytic solution. This generates complications when one tries to evaluate one numerical algorithm against another, as save for a few exceptions, an analytic benchmark cannot be employed. For this reason, approximations to the 1-D Euler equations which do have known analytic solutions, yet retain a one-dimensional nature have been developed. In the sections that follow, two such approximations are

presented which can be utilized for evaluation of numerical and model order reduction algorithms.

2.2.3.1 Linear Euler Equations

An approximation to the 1-D Euler equations can be obtained through a linearization process under the assumption of isentropic flow with a non-zero bulk gas velocity. Such a derivation is presented in Appendix 8.1.1, with the results shown in (2.22) and (2.23).

$$\frac{\partial \rho}{\partial t} + u_0 \frac{\partial \rho}{\partial x} + \rho_0 \frac{\partial u}{\partial x} = 0 \tag{2.22}$$

$$\frac{\partial u}{\partial t} + u_0 \frac{\partial u}{\partial x} + \frac{c^2}{\rho_0} \frac{\partial \rho}{\partial x} = 0 \tag{2.23}$$

The equation set can be seen to be a function of the spatial and temporally varying quantities of density and velocity, as well as of the space- and time-independent values of the mean gas velocity, density and speed of sound. This equation set can be represented in vector notation as shown in (2.24) - (2.26).

$$\frac{\partial U}{\partial t} + \frac{\partial F}{\partial x} = 0 \tag{2.24}$$

$$U = \begin{bmatrix} \rho \\ u \end{bmatrix} \tag{2.25}$$

$$F = \begin{bmatrix} \rho_0 u + u_0 \rho \\ \dfrac{c^2}{\rho_0} \rho + u_0 u \end{bmatrix} \tag{2.26}$$

An alternative vector notation is presented in (2.27) and (2.28), where the Jacobian matrix defined in (2.28) is employed.

$$\frac{\partial U}{\partial t} + A \frac{\partial U}{\partial x} = 0 \tag{2.27}$$

$$A = \frac{\partial F}{\partial U} = \begin{bmatrix} u_0 & \rho_0 \\ \dfrac{c^2}{\rho_0} & u_0 \end{bmatrix} \tag{2.28}$$

The eigenvalues of the Jacobian matrix are shown in (2.29), and represent the two wave speeds intrinsic to the equation set. It can be seen that the linear Euler equations permit the propagation of two waves in either direction with the first travelling at the speed of sound plus the bulk gas velocity, while the second travels at the speed of sound minus the bulk gas velocity.

$$Eigenvalues = \lambda = \begin{bmatrix} u_0 - c \\ u_0 + c \end{bmatrix} \tag{2.29}$$

Utilizing the relation shown in (2.30) as presented in Appendix 8.1.1, the analytic solution of an initial spatial profile in terms of pressure is defined in (2.31). Since the

wave speeds are constant, the solution at any time, t , is simply the summation of half of the initial profile shifted spatially by the product of the two wave speeds and the time t .

$$P = c^2 \rho \tag{2.30}$$

$$P(x,t) = \frac{P_0}{2}\left(x - (u+c)t\right) + \frac{P_0}{2}\left(x - (u-c)t\right) \tag{2.31}$$

2.2.3.2 Linear Convection Equation

A further simplification of the Euler equations is the Linear Convection Equation as derived in Appendix 8.1.2. As shown in (2.32), this equation models captures the convective nature of the Euler equations in a single linear partial differential equation.

$$\frac{\partial u}{\partial t} + c\frac{\partial u}{\partial x} = 0 \tag{2.32}$$

The equation models the propagation of the velocity u, with a constant speed c. The analytic solution of this equation at any time, t , is simply the initial profile shifted spatially by the product of the wave speed and the time t .

$$u(x,t) = u_0\left(x - ct\right) \tag{2.33}$$

2.2.4 Equations in Zero Dimensions

The zero-dimensional modeling methodology is based upon spatial lumping of a fluid system in to macro elements. In the case of internal combustion engine modeling, the intake and exhaust systems are generally lumped into respective volumes, where a single pressure and temperature is computed for each system. This approach is sometimes referred to as the "filling and emptying" method [1,7], and can be further categorized into Crank Angle Resolved (CAR) and Cycle-Resolved (CR) models. Within CAR 0-D models, the resolution of the simulation is generally at about a single crank angle degree, allowing for the prediction of crank angle resolved pressures and temperatures within the intake, cylinder and exhaust systems. Cycle resolved models, on the other hand, have a much lower resolution and thus predict cycle-average quantities for each sub-system. A description of the equations employed within zero-dimensional models is presented in the next section, followed by a brief review of these zero-dimensional modeling methodologies as applied to internal combustion engine research.

2.2.4.1 Governing Equations

The zero-dimensional modeling methodology aims at capturing the storage and release of mass and energy through the application of the continuity and energy equations to components of significant volume [30]. The momentum equation, along with the prediction of distributed effects, is neglected within this modeling methodology and instead flow restrictions are modeled with a quasi-steady approach [30].

The zero-dimensional continuity and energy equations can be derived directly from the one-dimensional equations, under the assumption that the flow variables have no spatial dependence within the control volume. This is analogous to a spatial piecewise constant assumption of flow variables, and is sometimes referred to as the "well-mixed" assumption. The one-dimensional continuity equation from (2.10), can be converted to zero-dimensional form, to yield (2.34) (see Chapter 5 for more details on this derivation).

$$l\frac{d(\rho A)}{dt} = (\rho A u)_{in} - (\rho A u)_{out} \tag{2.34}$$

This equation can be converted to a more well known form, through the definition of the density $\left(\rho = \frac{m}{V}\right)$, the assumption that the area of the volume does not change as a function of time $\left(A \neq f(t)\right)$ and through defining the mass flux or mass flow rate as $\dot{m} = \rho A u$. Applications of these relations to (2.34) yields the zero-dimensional continuity equation, as shown below, and again is applicable for zero-dimensional flow with spatial area variation.

$$\frac{dm}{dt} = \dot{m}_{in} - \dot{m}_{out} \tag{2.35}$$

Together with the definition of mass flux, the one-dimensional energy equation from (2.20), can be converted to zero-dimensional form, to yield (2.36), where the total

internal energy is defined as $e_0 = e + \frac{u^2}{2}$ (see Chapter 5 for more details on this derivation).

$$\frac{d\left(me_0\right)}{dt} = \left(\dot{m}h_0\right)_{in} - \left(\dot{m}h_0\right)_{out} + \dot{Q}_{ht} \tag{2.36}$$

2.2.4.2 Crank-Angle-Resolved 0-D Applications

Zero-dimensional, crank angle resolved models have been implemented in internal combustion engine applications since the 1950's and 1960's [28]. The early models consisted of ideal cycle calculations and component matching models [28], while during the 1970's and 1980's full thermodynamic models developed with the advent of the personal computer. Complete 0-D CAR models, such as that described by Zeleznick and McBride [36], include the description of the individual breathing, combustion and pressure profiles for each cylinder. These models allow for the prediction of individual torque pulses and crankshaft fluctuations and have been developed in both the time and crank angle domain. Due to the simplified structure and good compromise between fidelity and computation time, 0-D CAR models have been utilized for control systems applications. Dawson developed a 0-D CAR model capable of predicting individual cylinder breathing and pressure profiles, while maintaining a structure and computational effort amenable to controls design [29]. Arsie *et. al.* developed a 0-D CAR model for the purpose of rapid calibration of a Cycle-Resolved engine model [37]. However, as discussed in [1,39], this level of model is incapable of capturing wave propagation effects,

which become important for gas exchange applications where the ducting lengths are much greater than their diameter (as is the case in modern engines). This deficiency leads to large inaccuracies in volumetric efficiency and torque prediction. Thus while the 0-D CAR modeling approach gained popularity in the 1970's and early 1980's, its popularity was displaced with the development of 0-D Cycle-Resolved models [40-45] and the advent of commercially available one-dimensional engine simulation software [32, 38].

2.2.4.3 Cycle-Resolved 0-D Applications

The application of models to predict cycle-resolved (or "mean value") engine outputs has been popular since the late 1970's [40] and early 1980's [41-45], with its popularity increasing up through the present [47,53,55,56,66,72]. The intent of 0-D CR models is the prediction of the mean, cycle-resolved engine outputs to a reasonable degree of accuracy with a computational effort commensurate with a control oriented model. To this extent, 0-D CR modeling has been a success in that models have been shown to achieve $\pm 5\%$ steady state accuracy [47,51,53] and have been used in a number of studies for control design [60,61,63,64].

The 0-D CR models are generally characterized as three state models (intake manifold pressure, fuel dynamics, and engine speed) with algebraic expressions to describe the air flow through the throttle and the torque production within the engine. The manifold dynamics are described through either a direct application of the zero-dimensional continuity and energy equations, as described in Section 2.2.3.1, or through

a further approximation thereof (calorically perfect gas, isothermal or adiabatic). The manifold dynamics equations are generally supplemented with the speed density equation (2.37) to describe the air flow out of the manifold and into the engine [47,51,53,56], where the volumetric efficiency (η_v) is an empirical parameter implemented within the model through regression or neural network based approaches [47,48,37].

$$\dot{m}_{eng} = \frac{V_d N}{2RT_{im}} \eta_v P_{im} \tag{2.37}$$

The calibration of the volumetric efficiency term is typically reliant upon either a large quantity of experimental data or a large quantity of virtual data [76,77]. Typical predictor variables for fitting of the volumetric efficiency parameter may include engine speed, manifold pressure, an exhaust gas recirculation metric, and valve timing and duration [53,75]. The validity of this approach has been confirmed in steady state and transient operation, where the complex fluid dynamic phenomena of inertial ramming (acquisition and release of kinetic energy by the mass of gas in the intake) and wave propagation have been shown to be captured adequately [56,74].

2.3 Conclusions

In the world of modeling, the application, and thus the desired balance between fidelity and computation time governs the appropriate model structure. For gas exchange modeling in internal combustion engine applications, the modeler has a wide arsenal of model structures to choose from: multi-, one-, or zero-dimensional; viscous or inviscid;

real or ideal gas; crank-angle-resolved or cycle-resolved; *etc*. For applications involving detailed cylinder or flow junction design, the multi-dimensional simulation approach is desirable. However, for control systems design, optimization, and evaluation, the one- and zero-dimensional approaches are more applicable due to their simplified model structure and computational efficiency. In fact, the most common choice for performance simulations and control applications are the one-dimensional and cycle-resolved zero-dimensional engine models [27]. The one-dimensional models can be used for steady state engine mapping and static look-up table generation, while the cycle-resolved engine models are sufficient for large scale parameter optimizations and transient simulations. However, for applications such as cylinder pressure feedback control, misfire detection algorithms, hardware in the loop (HIL), and high fidelity transient simulations, the two standard modeling approaches leave something to be desired. The one-dimensional models, on one hand, generate sufficient fidelity, but are computationally cumbersome. The cycle-resolved zero-dimensional models are sufficiently fast, but do not provide the bandwidth and fidelity required for these applications. The crank-angle-resolved zero-dimensional models provide a unique balance between fidelity and computation time, but lack the accuracy in gas exchange modeling. It is with these thoughts in mind, that the research outlined in the following chapters has been performed to fill the void between 1-D and 0-D CR models with novel approaches at generating a high fidelity, computationally efficient model structure designed for control oriented applications.

CHAPTER 3

INTERNAL COMBUSTION ENGINE SYSTEMS MODELING: A CASE STUDY

3.1 Introduction

As discussed in the previous chapter, control systems engineering applications employ the use of engine models to aid in controls design, optimization and evaluation. For performance applications, the one-dimensional simulation technique has become the industry standard, while for large scale control studies and optimizations, the zero-dimensional cycle resolve model is the prevalent choice. In the sections that follow, a comparative study is conducted employing these two modeling approaches to evaluate their respective accuracy, fidelity, and computational time. A four cylinder, port fuel injected, spark ignition engine has been selected for the case study where the two modeling approaches are validated against a set of steady state experimental data collected on a engine test stand.

3.2 Experimental Data Collection

A steady state experimental test setup, complete with engine dynamometer, appropriate sensors and data acquisition equipment was employed for the collection of a

large data set for the calibration and validation of the two modeling methodologies. In the sections that follow, an overview is presented of the engine, sensors and data acquisition utilized in the collection of the pertinent data, where the reader is referred to Hoops [95], for further details.

3.2.1 Experimental Setup

The experimental testing was conducted on a General Motors four cylinder, Eco-Tec engine, as described in Table 1. The engine is port fuel injected, spark ignited, where dual independent cam phasors are utilized to optimize volumetric efficiency and torque production across the engine operating range.

Model	2.4l PFI SI
Cylinders	Inline 4
Displacement	2.4l
Bore, Stroke	88mm, 98mm
Compression Ratio	10.3:1
valve timing	Dual independent cam phasors
Power	130kW @ 6200r/min
Torque	222Nm @ 4800r/min

Table 1: Overview of Engine Specifications

The engine was coupled to a 300 Hp AC dynamometer and outfitted with both high and low resolution sensors for the collection of temperature, pressure, mass air flow

and torque measurements. An overview of the major sensors and sensor locations is presented in Table 2 and Figure 3.

Sensor Location	Description	Resolution
2	Upstream Catalyst Temperature	Low
3	Downstream Catalyst Temperature	Low
5-8	Exhaust Runner Temperatures	Low
9	Exhaust Manifold Temperature	Low
13-16	Intake Runner Temperatures	Low
21	Intake Manifold Temperature	Low
26-29	Cylinder Pressure	High
30	Intake Manifold Pressure	High
31	Exhaust Manifold Pressure	High
37	Crankshaft Encoder	High
38	Engine Speed	Low
39	Engine Brake Torque	Low
40	Oxygen Sensor	Low
41	Emission Measurements	Low

Table 2: Description of Engine Sensors

Four piezoelectric pressure transducers implemented for individual cylinder pressure measurements were mounted in the spark plug bore. The sensor pegging operation was conducting based upon reference high resolution intake and exhaust manifold piezeoresistive pressure sensors, as described in [95]. The exhaust pressure sensor included a cooling jack to avoid thermal shock. The engine's air-fuel ratio was estimated with use of a Universal Exhaust Gas Oxygen (UEGO) sensor, while the engine out emissions were characterized through a Horiba Five Gas Analyzer.

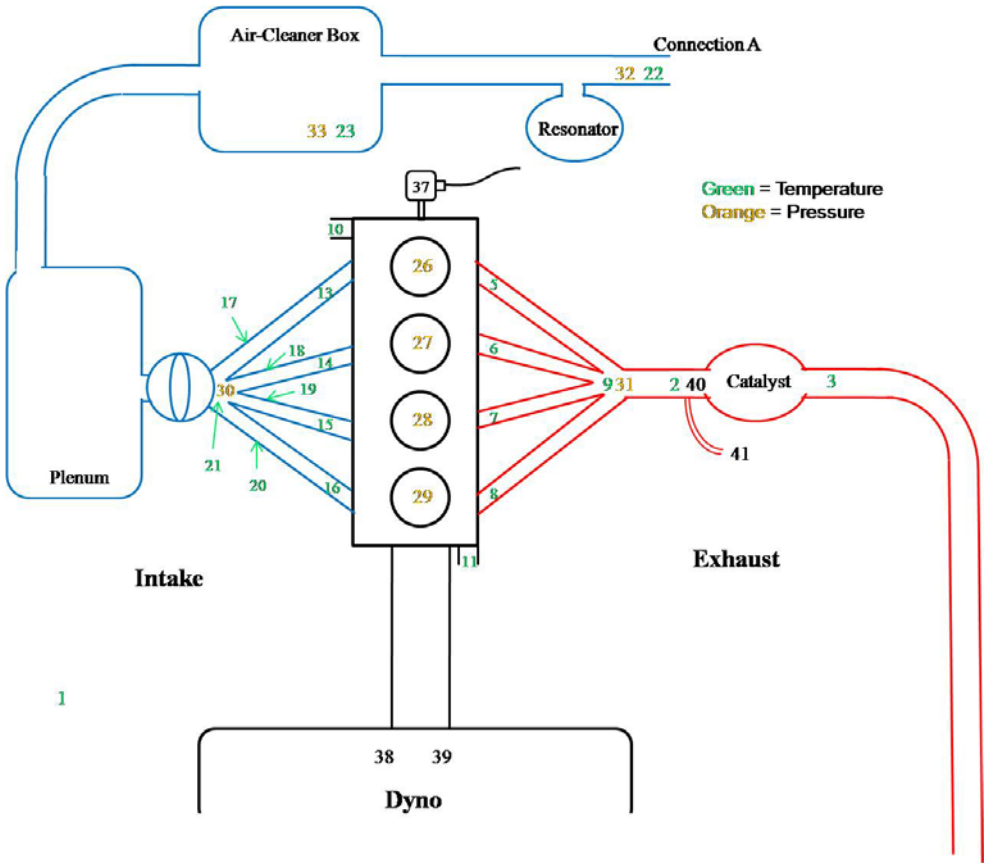

Figure 3: Overview of Engine Sensor Locations [95]

3.2.2 Data Acquisition and Post-Processing

The experimental setup outlined in the previous section was utilized to collect a data set of two-thousand steady state engine operating points for the calibration and validation of the model architectures. Twelve hundred of these points were dedicated to calibration, while the remaining eight-hundred points were utilized for validation of the models. The Design of Experiments (DoE) for the testing was done utilizing the Latin-

hypercube space filling method [96] in the dimensions of engine speed, load, intake and exhaust cam timing locations. Additionally, spark sweeps were performed at each operating point. The engine load was specified based upon the metric of the mass of air in the cylinder at intake valve closing and the DoE set points for load were obtained experimentally through throttle angle manipulation. The details of the data collection, including cylinder pressure pegging and data diagnostics may be found in [95].

3.3 One-Dimensional Gas Dynamic Modeling

A one-dimensional gas dynamic model representing the engine configuration defined in the previous section has been developed in the commercial software GT Power [32] for gas exchange and combustion performance analysis. The engine model's gas exchange and combustion models have been calibrated based upon the steady state experimental data. In the sections that follow, the model architecture, calibration and validation results are outlined.

3.3.1 Model Architecture

A representation of the engine's intake, cylinders and exhaust systems has developed utilizing the graphical interface provided in the GT Power software. This representation is shown in Figure 4, and includes a one-dimensional representation of the intake and exhaust systems, and a zero-dimensional representation of the cylinders, where a single-zone thermodynamic combustion model is employed.

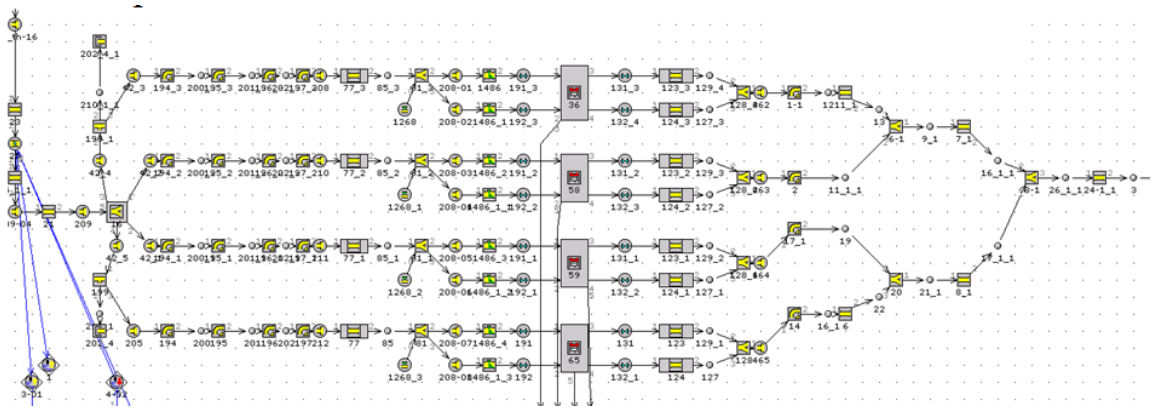

Figure 4: One-Dimensional Model Implementation

3.3.2 Model Calibration

The subsystems that require significant calibration include the discharge coefficients of the throttle and the valves, the combustion parameters for the heat-release model, and the frictional and heat transfer losses within the intake and exhaust systems.

The valve lift profiles and discharge coefficients have been found through experimental testing on a flow bench [1,2]. The throttle discharge coefficient has been identified through correlating the isentropic orifice equations to experimental data collected on a steady state test bench. For optimal results, the throttle discharge coefficient has been modeled as a function of throttle angle and speed and implemented as a static look-up table, as shown in the normalized Figure 5.

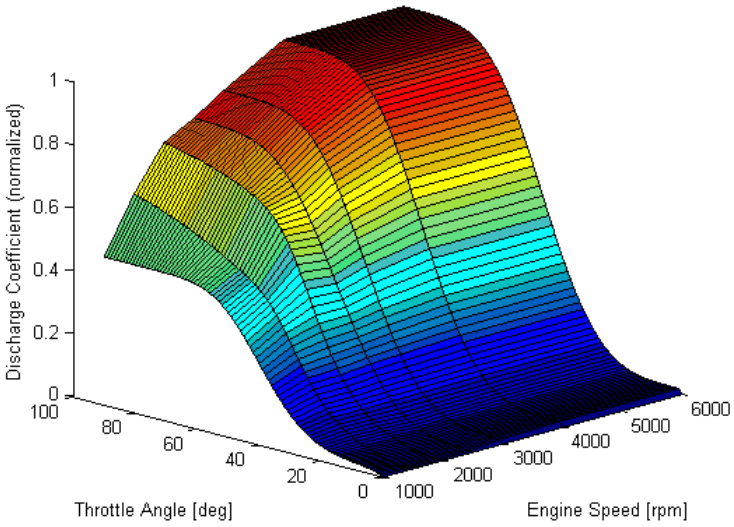

Figure 5: Throttle Discharge Coefficient (Normalized to One)

The intake and exhaust system's heat transfer and frictional parameters have been tuned to eliminate systematic errors in temperature and mass air flow prediction. As a validation of these parameters (as well as of the intake and exhaust geometrical parameters), the prediction of volumetric efficiency during a speed sweep is shown to be predicted within +-5% error bounds in Figure 6.

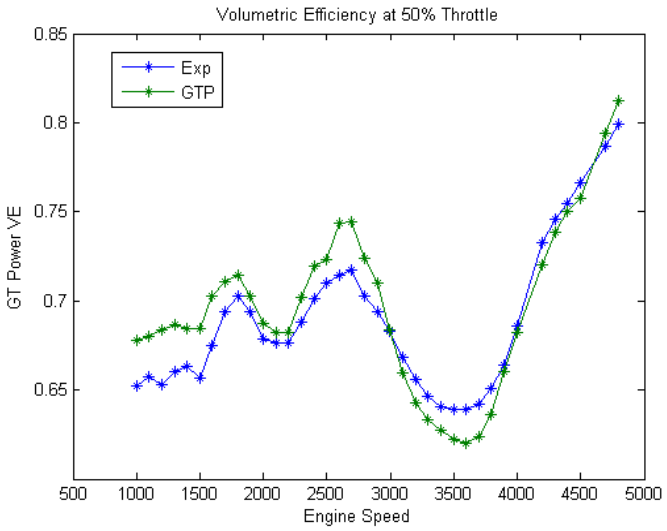

Figure 6: Volumetric Efficiency Prediction at 50% Throttle

The combustion model has been calibrated first by identification of the burn rate through an inverse thermodynamic calculation based upon the experimental cylinder pressure. Next, the Wiebe function shown in (3.1) is fit to the burn rate through a least squares curve fit.

$$
\begin{aligned}
x_b &= \alpha\left(1-e^{-WC_1(\theta-SOC_1)^{E_1+1}}\right) \\
WC_1 &= \left[\frac{D_1}{BEC^{\frac{1}{E_1+1}}-BSC^{\frac{1}{E_1+1}}}\right]^{-(E_1+1)} \\
SOC_1 &= AA_1-\frac{D_1\cdot(BMC)^{\frac{1}{E_1+1}}}{BEC^{\frac{1}{E_1+1}}-BSC^{\frac{1}{E_1+1}}}
\end{aligned}
\tag{3.1}
$$

Finally, the identified Wiebe function parameters are modeled through neural network approaches to extend the combustion model throughout the entire engine operating range. As an example of this, the surface modeling of the burn duration is shown in Figure 7, as a function of speed and load at parked cam timing.

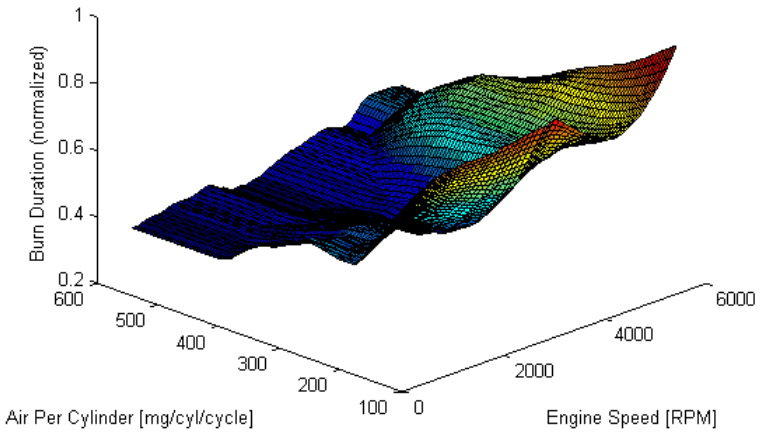

Figure 7: Burn Duration at Parked Cam Timing (Normalized to One)

3.3.3 Model Validation

The one-dimensional model was simulated over the eight-hundred steady-state validation points and is compared against the experimental data in the following figures. For performance predictions, the plot on the left of Figure 8 shows that the 1-D model adequately predicts the gas exchange process and wave dynamic effects leading to an

accurate representation of volumetric efficiency. The plot on the right of Figure 8 displays that the combustion parameters have been adequately modeled such that, when coupled to an accurate gas exchange prediction, the cylinder model captures the heat release and cylinder pressure profile sufficiently to model the net brake torque.

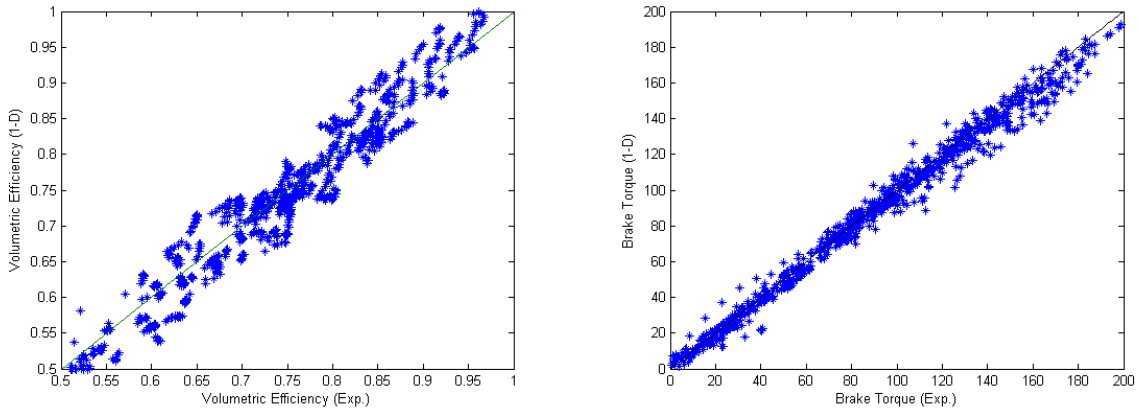

Figure 8: Performance Prediction of 1-D Model; Left: Volumetric Efficiency; Right: Brake Torque

In Figure 9, it is shown that the gas exchange portion of the 1-D model captures the mean pressures in both in the intake and the exhaust systems over the four dimensional operating space.

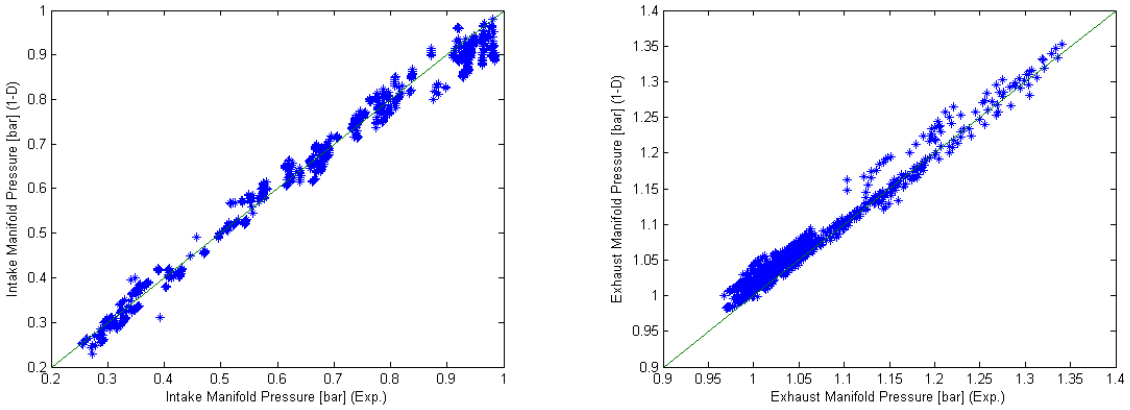

Figure 9: Manifold Pressure Prediction of 1-D Model; Left: Intake Manifold Pressure; Right: Exhaust Manifold Pressure

Furthermore, the crank-angle-resolved prediction capability of the one-dimensional model is exemplified in Figure 10, where it can be seen that the model is capable of capturing the experimental traces of intake manifold and cylinder pressure to high degree of resolution.

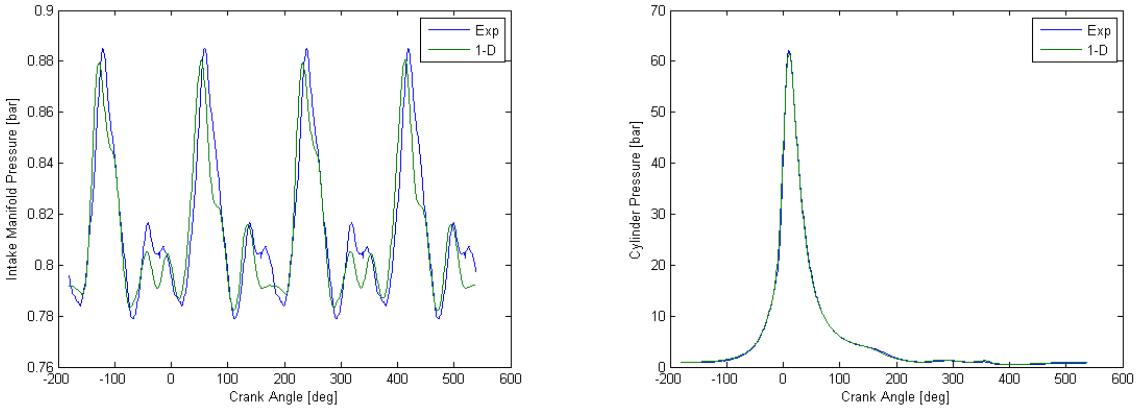

Figure 10: Crank-Angle-Resolved Prediction of 1-D Model; Left: Intake Manifold Pressure; Right: Cylinder Pressure; 4200 RPM, 46^{o} Throttle Opening, -26^{o} Spark

3.4 Cycle-Resolved Zero-Dimensional Modeling

3.4.1 Model Architecture

Cycle-Resolved, zero-dimensional models are often employed for low-fidelity, control-oriented applications [60,61,63,64]. As discussed in Chapter 2, this level of model results in a cycle-resolved prediction of states and is described through a combination of a low-order set of differential and algebraic relations. Such a model structure is exemplified in Figure 11.

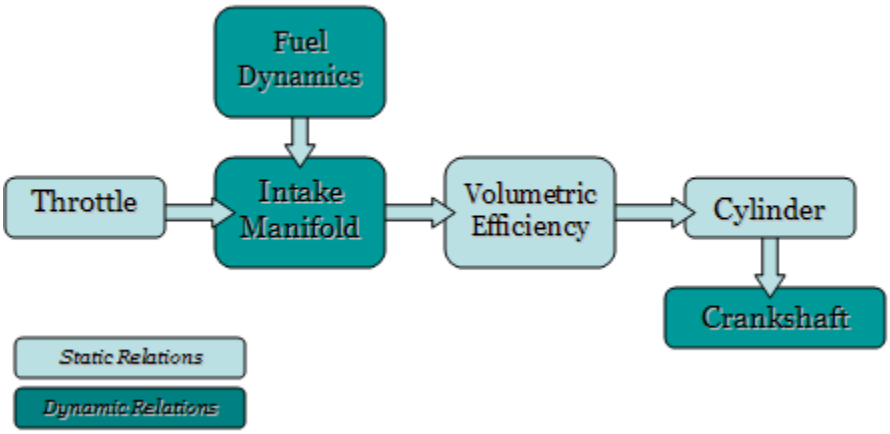

Figure 11: Cycle-Resolved, Zero-Dimensional Model Structure

It can be seen that the model consists of states for the intake manifold, fuel dynamics and crankshaft, and is influenced significantly by the empiric static relations for volumetric efficiency and torque production. The differential relations follow the zero-dimensional methodology discussed in Chapter 2, while the static relations require significant calibration, as discussed in the next section.

3.4.2 Model Calibration

The empiric relations supporting the 0-D CR model structure require a vast amount of data for calibration. For this case study, this data has been generated utilizing a combination of experimental data and virtual engine mapping techniques [28,77,97]. The volumetric efficiency parameter requires dependent variables that affect the gas exchange process and thus is a function of the engine speed, intake manifold pressure, and intake and exhaust cam timing. The brake torque relation requires dependent variables that

affect the combustion process, and thus is a function of the engine speed, air per cylinder, spark timing and intake and exhaust cam timing. Utilizing the techniques described in [28,77,97], these parameters are calibrated from the 1-D model described in the previous section and implemented as look-up tables. The surfaces at parked cam timing and fixed spark timing are shown in Figure 12.

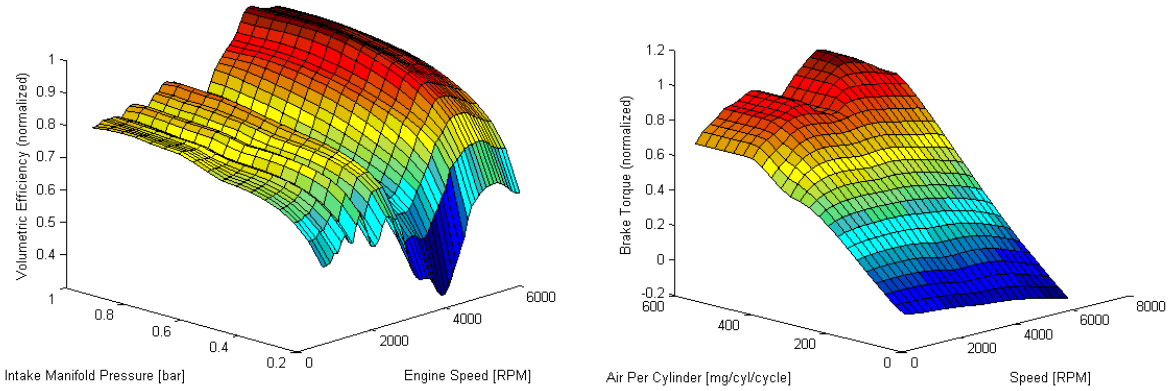

Figure 12: Empiric Relations within Zero-Dimensional, Cycle-Resolved Model

(Normalized to One)

3.4.3 Model Validation

Analogous to the one-dimensional model validation, the 0-D CR model was simulated over the eight-hundred steady-state validation points and compared against the experimental data. The plot on the left of Figure 13 shows that the 0-D CR model with its low frequency intake system and empirical relations, is capable of capturing the cycle-

resolved gas exchange process and wave dynamic effects with a similar accuracy to that of the 1-D model. The plot on the right of Figure 13 displays that the empiric torque model has been sufficiently calibrated to model the net brake torque over the entire engine map.

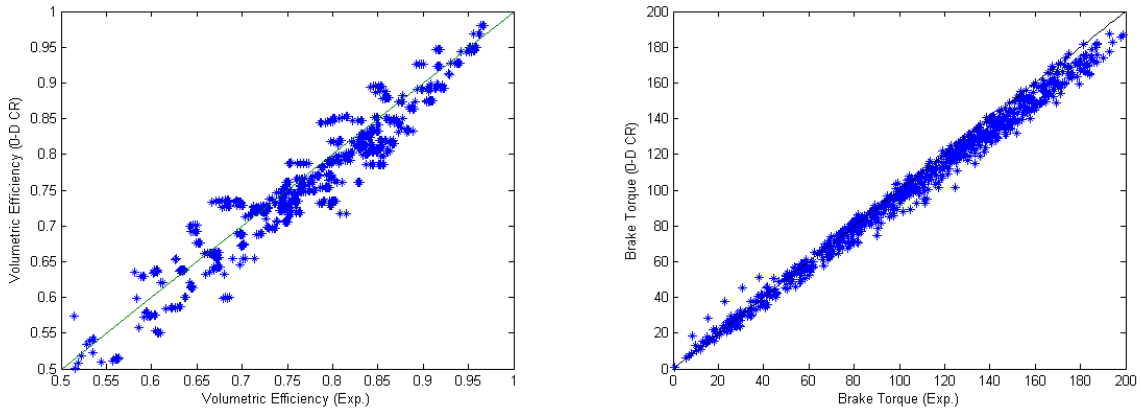

Figure 13: Performance Prediction of 0-D CR Model; Left Volumetric Efficiency; Right: Brake Torque

In Figure 14, it can be seen that the gas exchange portion of the 0-D CR model captures the mean pressures in both in the intake and the exhaust systems over the four dimensional operating space.

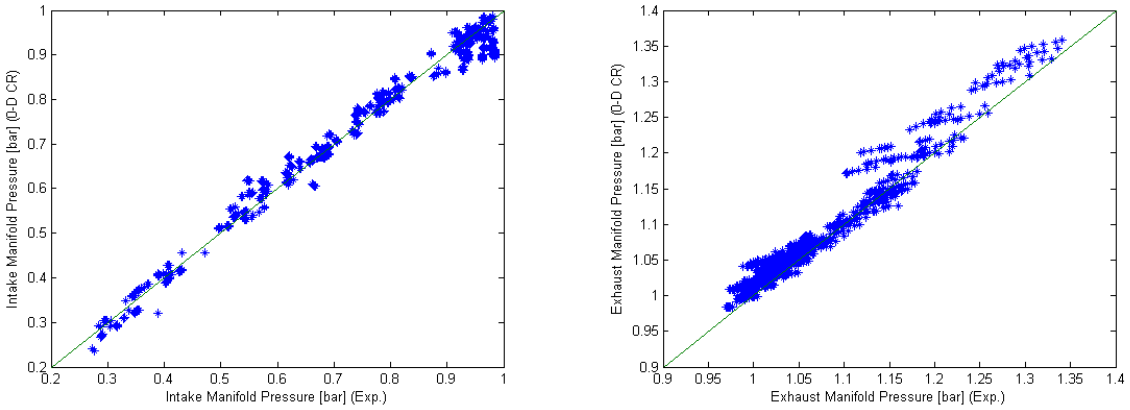

Figure 14: Manifold Pressure Prediction of 0-D CR Model; Left: Intake Manifold Pressure; Right: Exhaust Manifold Pressure

3.5 Conclusions

The structure and accuracy of the one-dimensional and zero-dimensional cycle-resolved modeling techniques have been explored against steady-state experimental data in the case study of a four cylinder spark ignited engine.

It has been shown that the 1-D simulation model is capable of describing not only the cycle-resolved variables of the gas exchange and combustion process well with respect to experimental data, but is also capable of capturing high resolution crank angle resolved states of manifold and cylinder pressures. Thus it is clear that the 1-D simulation approach can provide sufficient fidelity for valve timing parameter

optimizations, steady-state engine mapping, static look-up table generation and perhaps even sensor placement studies.

The results have also shown that the 0-D CR model, when calibrated with sufficient data, can achieve similar accuracy in cycle-resolved prediction of gas exchange and torque variables as the one-dimensional approach. Due to the simplicity and computational efficiency of this method, this model structure is more amenable for model-based control systems design, large scale parameter optimizations and for lengthy transient simulations.

However, for applications requiring both a high level of fidelity (crank-angle-degree resolution of states) and a low computational effort, these two approaches leave something to be desired. Such applications may include hardware in the loop (HIL), full vehicle drivability simulations, or the development and evaluation of transient cylinder pressure feedback control or cylinder misfire detection algorithms.

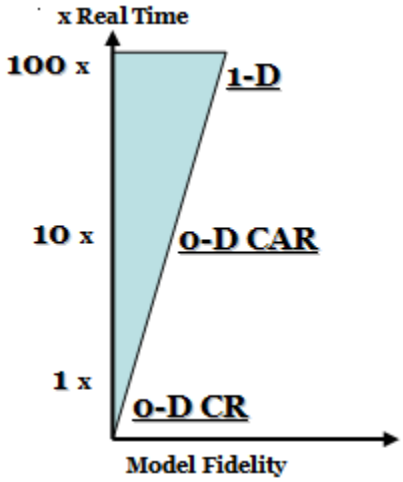

Figure 15: Model Fidelity vs. Computation Time

The one-dimensional approach may provide sufficient resolution in states, but as Figure 15 displays, requires computational times on the order of one-hundred times real time. The 0-D CR methodology provides more than sufficient computational times, but lacks the desired bandwidth. This level of model provides cycle-resolved states and thus is inappropriate for applications where crank angle degree resolution of states is required. As exemplified in Figure 15, the crank-angle-resolved zero-dimensional models would provide a better balance between fidelity and computation time for these applications. However, as discussed in the previous chapter, this level of model lacks accuracy in gas exchange modeling. In the following chapter, the zero-dimensional crank-angle-resolved model structure is explored in detail against the same case study used in this chapter to highlight the strengths and weaknesses of its approach. Furthermore, based upon this

analysis, a novel technique is developed for improving the accuracy of the approach such that it is both sufficiently fast and accurate for the aforementioned applications.

CHAPTER 4

EMPIRICALLY BASED COMPRESSIBLE FLUID SYSTEMS MODELING

4.1 Introduction

As discussed in the previous chapter, traditional modeling approaches for engine system simulation and control activities include that of the one-dimensional gas-dynamic and zero-dimensional cycle-resolved dynamic models. These modeling methodologies have been shown to be appropriate for their respective applications, but somewhat lacking for applications requiring both crank angle degree resolution and a low computational effort. Research activities [29,36,37] have made use of the zero-dimensional crank-angle-resolved modeling methodology for such application areas, but as discussed in [1,39], this level of model is incapable of capturing wave propagation effects, leading to large inaccuracies in volumetric efficiency and torque prediction. This deficiency has detracted engine researchers from utilizing this approach.

In the following sections, this modeling methodology is explored in detail, beginning with the model structure, assumptions and governing equations. The methodology is then applied to the case study four cylinder spark ignited engine utilized

in the previous chapter, with an emphasis on an analysis of the steady state simulation results. Based upon this analysis, a novel technique is developed to overcome the deficiency of this approach by incorporating wave dynamic effects within the lumped parameter architecture to permit a model that not only provides accurate crank-angle-degree resolution of states, but remains computationally efficient.

4.2 Traditional Crank-Angle-Resolved Zero-Dimensional Models

As discussed in Chapter 2, the 0-D CAR methodology is based upon spatial lumping of a system into macro elements, where the conservations of mass and energy are applied to characterize the storage and release of mass and energy. Such a methodology neglects the inherently distributed effects of wave propagation described in part by the conservation of momentum, and instead applies a quasi-steady approximation for elements representing large flow losses. Utilizing these assumptions, the model structure and equations employed within a 0-D CAR model are presented in the following section in detail.

4.2.1 Model Structure and Governing Equations

The model structure considered to characterize the engine dynamics is based on the input/system/output representation, which allows one to isolate the most important engine system components, and represent them as interconnected dynamic models.

Figure 16 shows the system decomposition methodology applied to a four cylinder engine.

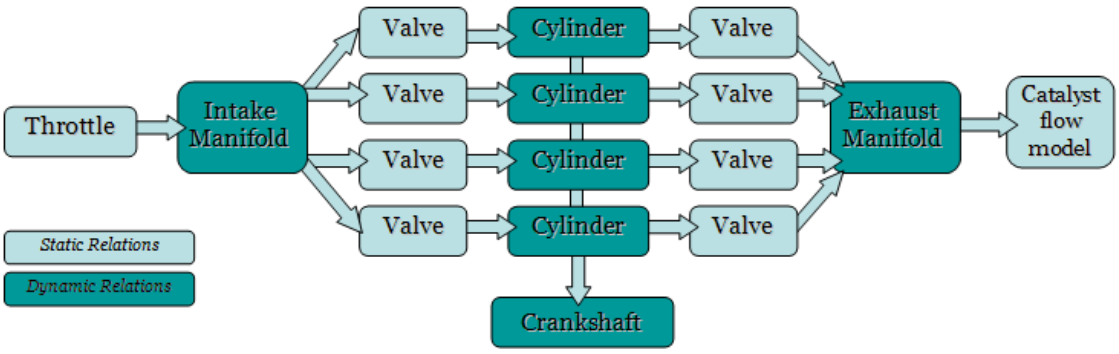

Figure 16: Zero-Dimensional Crank Angle Resolved Model Structure

With reference to Figure 16, the components comprising significant volume and thus lumped in to macro fluid elements include that of the cylinders and the intake and exhaust manifolds. The components representing significant flow losses include the throttle, the intake and exhaust valves, and the losses associated to the catalyst. Within the volume elements, the model predicts pressure, temperature, mass, and species concentration states, while within the flow restriction elements, the model predicts velocity and mass flow rate states.

4.2.1.1 Flow Restriction Elements

The flow restriction elements are characterized through a quasi-steady approximation, where the mass and energy conservation laws are simplified by eliminating the dependence on time, leading to quasi-static (purely algebraic) model. A derivation of this model can be found in [1], with the result presented in (4.1). Note the use of total conditions for the upstream location.

$$\dot{m} = C_d A \frac{p_{t,in}}{\sqrt{RT_{t,in}}} \sqrt{\frac{2\gamma}{\gamma - 1}\left[\left(\frac{p_{out}}{p_{t,in}}\right)^{\frac{2}{\gamma}} - \left(\frac{p_{out}}{p_{t,in}}\right)^{\frac{\gamma+1}{\gamma}}\right]} \tag{4.1}$$

The maximum mass flow rate will occur when the gas velocity reaches the speed of sound. This condition is referred to as choked flow and occurs when the pressure at the throat exceeds the critical pressure defined in (4.2).

$$p_{crit} = p_{t,in}\left(\frac{2}{\gamma+1}\right)^{\frac{\gamma}{\gamma-1}} \tag{4.2}$$

When the upstream pressure exceeds the critical pressure, equation (4.1) is modified to the form shown in (4.3) to properly account for the chocked condition.

$$\dot{m} = C_d A \frac{p_{t,in}}{\sqrt{RT_{t,in}}} \sqrt{\left(\frac{2}{\gamma+1}\right)^{\frac{\gamma+1}{\gamma-1}}} \tag{4.3}$$

The product C_dA shown in the above equations represents the effective flow area, an empirical function of the valve opening. Such a parameter is generally determined from calibration, for instance using data from a component flow bench or an engine test bench as described in Section 3.2.2.

The above equations are applicable to each of the static flow restriction elements shown in Figure 16. However, in order to account for reverse flow, the inlet conditions (p_{in}, T_{in}) must be chosen so that p_{in} is the greatest between the upstream and downstream pressure across the restriction. The specific heat ratio γ depends on the gas temperature and is calculated with respect to the inlet thermodynamic conditions.

4.2.1.2 Volume Elements

The components shown in Figure 16 that are characterized by mass or energy storage are modeled using the unsteady mass and energy equations, assuming uniform distribution of the thermodynamic properties within the volume, as described in Section 2.2.3.1. The details of the equations will be presented as applied to the intake manifold and the cylinder, where an extension to the exhaust manifold is straight forward. The model of the volumes are characterized by the total mass contained in the volume, the bulk temperature and the composition. The composition terms accounts for the various species that are present in the mixture, in this case: air, residuals from the exhaust gases and fuel vapor.

Intake Manifold Mass and Concentration Dynamics:

The zero-dimensional mass conservation law defined previously in (2.35), can be applied directly to the intake manifold volume shown in Figure 16, to yield (4.4).

$$\frac{dm_{im}}{dt} = \dot{m}_{th} - \sum_{1}^{num_{cyl}} \dot{m}_{iv}(i) \tag{4.4}$$

Conservation equations can be defined for each of the species found in the intake manifold (air, residual exhaust gas, vaporized fuel) under the assumption of non-reacting flows through defining mass fractions for each species as shown in Appendix 8.2.2. The results of this derivation are repeated here in equations (4.5), (4.6) and (4.7), where it can be seen that dynamic equations are defined for the mass fractions of fuel and exhaust gas, while a static relation is defined for the mass fraction of air.

$$\frac{dX_{ex,im}}{dt} = \frac{1}{m_{im}}\left\{\dot{m}_{th}K_{th,im,ex} - \sum_{1}^{num_{cyl}}\left\{\dot{m}_{iv}(i)\cdot K_{iv,im,ex}(i)\right\} - X_{ex,im}\frac{dm_{im}}{dt}\right\} \tag{4.5}$$

$$\frac{dX_{fuel,im}}{dt} = \frac{1}{m_{im}}\left\{\dot{m}_{th}K_{th,im,fuel} + \dot{m}_{fi} - \sum_{1}^{num_{cyl}}\left\{\dot{m}_{iv}(i)\cdot K_{iv,im,fuel}(i)\right\} - X_{fuel,im}\frac{dm_{im}}{dt}\right\} \tag{4.6}$$

$$X_{air,im} = 1 - X_{ex,im} - X_{fuel,im} \tag{4.7}$$

The 'K' parameters shown in equations (4.5) and (4.6) allow for flow reversal conditions, and are defined in Table 3.

$For\ \dot{m}_{th} > 0$	$For\ \dot{m}_{th} < 0$	$For\ \dot{m}_{iv} > 0$	$For\ \dot{m}_{iv} < 0$
$K_{th,im,ex} = 0$	$K_{th,im,ex} = X_{ex,im}$	$K_{iv,im,ex} = X_{ex,im}$	$K_{iv,im,ex} = X_{ex,cyl}$
$K_{th,im,fuel} = 0$	$K_{th,im,fuel} = X_{fuel,im}$	$K_{iv,im,fuel} = X_{fuel,im}$	$K_{iv,im,fuel} = X_{fuel,cyl}$

Table 3: Parameter Definition for Intake Manifold Species Concentration Equations

Intake Manifold Temperature and Pressure Dynamics:

The temperature dynamics within the manifold are described as a form of the zero-dimensional conservation of energy equation, originally defined in (2.36). This equation is modified in Appendix 8.2.1, to yield the result shown in (4.8).

$$\frac{dT_{im}}{dt} = \frac{1}{m_{im} c_{v,im}} \begin{Bmatrix} \dot{m}_{th}\left(K_{th,im} - e_{im}\right) - \sum_{1}^{num_{cyl}} \left\{ \dot{m}_{iv}(i) \cdot \left(K_{iv,im}(i) - e_{im}\right) \right\} - \dot{Q}_{ht,im} + \ldots \\ \left(e_{air,im} - e_{ex,im}\right) m_{im} \frac{dX_{ex,im}}{dt} + \left(e_{air,im} - e_{fuel,im}\right) m_{im} \frac{dX_{fuel,im}}{dt} \end{Bmatrix} \quad (4.8)$$

Where again the 'K' parameters are defined for flow reversal conditions as shown in Table 4.

$For\ \dot{m}_{th} > 0$	$For\ \dot{m}_{th} < 0$	$For\ \dot{m}_{iv} > 0$	$For\ \dot{m}_{iv} < 0$
$K_{th,im} = h_0$	$K_{th,im} = h_{im}$	$K_{iv,im} = h_{im}$	$K_{iv,im} = h_{cyl}$

Table 4: Parameter Definition for Intake Manifold Energy Equation

Furthermore, it is possible to determine the pressure within the manifold by applying the ideal gas law:

$$P_{im} = \frac{m_{im} R_{im} T_{im}}{V_{im}} \tag{4.9}$$

Cylinder Mass and Concentration Dynamics:

Again, the zero-dimensional mass conservation law defined previously in (2.35), can be applied directly to the cylinder volume shown in Figure 16, to yield (4.10).

$$\frac{dm_{cyl}}{dt} = \sum_{1}^{num_{cyl}} \dot{m}_{iv}(i) - \sum_{1}^{num_{cyl}} \dot{m}_{ev}(i) \tag{4.10}$$

The conservation equations for each of the species found in the cylinder can be defined in a similar fashion as the intake manifold, except that care must be taken to account for the conversion of fuel and air into exhaust gas during combustion, as outlined in Appendix 8.2.2. The results of this derivation are repeated here in equations (4.11), (4.12) and (4.13).

$$\frac{dX_{ex,cyl}}{dt} = \frac{1}{m_{cyl}} \left\{ \sum_{1}^{num_{cyl}} \left\{ \dot{m}_{iv}(i) \cdot K_{iv,cyl}(i) \right\} - \sum_{1}^{num_{cyl}} \left\{ \dot{m}_{ev}(i) \cdot K_{ev,cyl}(i) \right\} + m_{charge,IVC} \frac{dX_b}{dt} - X_{ex,cyl} \frac{dm_{cyl}}{dt} \right\} \tag{4.11}$$

$$\frac{dX_{fuel,cyl}}{dt} = \frac{1}{m_{cyl}} \left\{ \sum_{1}^{num_{cyl}} \left\{ \dot{m}_{iv}(i) \cdot K_{ivf,cyl}(i) \right\} - \sum_{1}^{num_{cyl}} \left\{ \dot{m}_{ev}(i) \cdot K_{evf,cyl}(i) \right\} + m_{fuel,IVC} \frac{dX_b}{dt} - X_{fuel,cyl} \frac{dm_{cyl}}{dt} \right\} \tag{4.12}$$

$$X_{air,cyl} = 1 - X_{ex,cyl} - X_{fuel,cyl} \tag{4.13}$$

Again, the 'K' parameters shown in equations (4.11) and (4.12) allow for flow reversal conditions, and are defined in Table 5.

$For\ \dot{m}_{iv} > 0$	$For\ \dot{m}_{iv} < 0$	$For\ \dot{m}_{ev} > 0$	$For\ \dot{m}_{ev} < 0$
$K_{iv,cyl} = X_{ex,im}$	$K_{iv,cyl} = X_{ex,cyl}$	$K_{ev,cyl} = X_{ex,cyl}$	$K_{ev,cyl} = X_{ex,em}$
$K_{ivf,cyl} = X_{fuel,im}$	$K_{ivf,cyl} = X_{fuel,cyl}$	$K_{evf,cyl} = X_{fuel,cyl}$	$K_{evf,cyl} = X_{fuel,em}$

Table 5: Parameter Definition for Cylinder Species Concentration Equations

Cylinder Thermodynamics:

The temperature dynamics within the cylinder are described as a form of the zero-dimensional conservation of energy equation, originally defined in (2.36). This equation is modified in Appendix 8.2.1 to include the effects of the work done by the change in volume of the cylinder and to include the heat released during combustion. The resulting cylinder temperature dynamics equation is shown in (4.14).

$$\frac{dT_{cyl}}{dt} = \frac{1}{m_{cyl}c_{v,cyl}}\left\{\begin{array}{l} \dfrac{dQ_{com}}{dt} - \dfrac{dQ_{ht,cyl}}{dt} - P_{cyl}\dfrac{dV_{cyl}}{dt} + \sum_{1}^{num_{cyl}}\left\{\dot{m}_{iv}(i)\left(K_{iv,cyl}(i) - e_{cyl}\right)\right\} - \ldots \\ \sum_{1}^{num_{cyl}}\left\{\dot{m}_{ev}(i)\left(K_{ev,cyl}(i) - e_{cyl}\right)\right\} + \left(e_{air,cyl} - e_{ex,cyl}\right)m_{cyl}\dfrac{dX_{ex,cyl}}{dt} + \ldots \\ \left(e_{air,cyl} - e_{fuel,cyl}\right)m_{cyl}\dfrac{dX_{fuel,cyl}}{dt} \end{array}\right\} \qquad (4.14)$$

The 'K' parameters are defined for flow reversal conditions as shown in Table 6.

$For\ \dot{m}_{iv} > 0$	$For\ \dot{m}_{iv} < 0$	$For\ \dot{m}_{ev} > 0$	$For\ \dot{m}_{ev} < 0$
$K_{iv,cyl} = h_{im}$	$K_{iv} = h_{cyl}$	$K_{ev} = h_{cyl}$	$K_{ev} = h_{em}$

Table 6: Parameter Definition for Cylinder Energy Equation

The term shown in (4.14) accounting for the heat released during the combustion process is modeled through the use of the burn rate, the lower heating value of the fuel, and the mass of fuel present when combustion occurs.

$$\frac{dQ_{com}}{dt} = m_{f,cyl} Q_{LHV} \frac{dX_b}{dt} \tag{4.15}$$

It should be noted that the mass of fuel utilized in equation (4.15) should be limited based upon the quantity of available air for combustion by assuming that the excess fuel in rich conditions does not participate in the heat release:

$$m_{f,cyl} = \min\left[m_{f,IVC}, \frac{m_{air,IVC}}{AFR_s} \right] \tag{4.16}$$

The burn rate is modeled through the use of a Wiebe function [1].

$$x_b = 1 - \exp\left(-a \left(\frac{\theta - \theta_{sp}}{\Delta\theta} \right)^{m+1} \right) \tag{4.17}$$

Differentiating (4.17) with respect to the crank angle (θ) yields:

$$\frac{dx_b}{d\theta} = \frac{a(m+1)}{\Delta\theta}\left(\frac{\theta-\theta_{sp}}{\Delta\theta}\right)^m \exp\left(-a\left(\frac{\theta-\theta_{sp}}{\Delta\theta}\right)^{m+1}\right) \tag{4.18}$$

The derivative of the burn rate with respect to time can then be inferred to be:

$$\frac{dx_b}{dt} = \frac{d\theta}{dt}\cdot\frac{dx_b}{d\theta} = \omega\frac{dx_b}{d\theta} = \omega\frac{a(m+1)}{\Delta\theta}\left(\frac{\theta-\theta_{sp}}{\Delta\theta}\right)^m \exp\left(-a\left(\frac{\theta-\theta_{sp}}{\Delta\theta}\right)^{m+1}\right) \tag{4.19}$$

The cylinder heat transfer model calculates the heat loss due to the heat transfer occurring between the gas and the cylinder walls. A few well established approaches are available, including the Woschni [130] and the Bargende [131] correlations to estimate the heat transfer coefficient. The Woschni [130] correlation is presented here.

$$\frac{dQ_{ht}}{dt} = h_{ht,cyl}A_{cyl}\left(T_{cyl}-T_w\right) \tag{4.20}$$

$$h_{ht,cyl} = \frac{3.26\left(\frac{P_{cyl}}{1000}\right)^{.8} w^{.8}}{B^{.2}T_{cyl}^{\ .546}} \tag{4.21}$$

$$w = C_1\overline{S}_p + C_2\frac{V_d T_{ref}}{P_{ref}V_{ref}}\left(P_{cyl}-P_{motor}\right) \tag{4.22}$$

For intake and exhaust:	*For compression:*	*For combustion and expansion:*
$C_1 = 6.18$	$C_1 = 2.28$	$C_1 = 2.28$
$C_2 = 0$	$C_2 = 0$	$C_2 = 3.24\cdot10^{-3}$

The pressure within the cylinder is described by applying the ideal gas law:

$$P_{cyl} = \frac{m_{cyl} R_{cyl} T_{cyl}}{V_{cyl}} \tag{4.23}$$

4.2.1.3 Thermodynamic Properties

As discussed in Chapter 2, the thermodynamic properties may be defined as thermally or calorically perfect. For the present application, the properties are defined as thermally perfect and are calculated using a six species equilibrium calculation to estimate the composition of the products. The chemical species considered are O_2, N_2, CO_2, CO, H_2 and H_2O, while the fuel used is gasoline ($C_{8.26}H_{15.5}$). The thermodynamic properties are fitted with the routines proposed by Gordon and McBride [98], based on the tabulated JANAF data [99]:

$$\begin{aligned}
\frac{c_p}{R} &= a_1 + a_2 T + a_3 T^2 + a_4 T^3 + a_5 T^4 \\
\frac{h}{RT} &= a_1 + \frac{a_2}{2} T + \frac{a_3}{3} T^2 + \frac{a_4}{4} T^3 + \frac{a_5}{5} T^4 + a_6 \frac{1}{T} \\
\frac{s}{R} &= a_1 \ln T + \frac{a_2}{2} T + \frac{a_3}{3} T^2 + \frac{a_4}{4} T^3 + \frac{a_5}{5} T^4 + a_7
\end{aligned} \tag{4.24}$$

The reactions considered in the model are the combustion balance:

$$C_n H_m + \frac{n + m/4}{\varphi}\left(O_2 + 3.773 N_2\right) \rightarrow n_p \left(x_{CO_2} CO_2 + x_{CO} CO + x_{H_2O} H_2O + x_{H_2} H_2 + x_{O_2} O_2 + x_{N_2} N_2\right) \tag{4.25}$$

and the water-gas shift:

$$CO_2 + H_2 \leftrightarrow CO + H_2O \tag{4.26}$$

The equilibrium of the water-gas shift reaction is determined by:

$$K_t = \frac{x_{CO} x_{H_2O}}{x_{CO_2} x_{H_2}} \tag{4.27}$$

The equilibrium constant K_t (generally, a function of temperature), is assumed constant and equal to 3.5 [1].

By solving the equations above, it is possible to estimate the gas composition and thermodynamic properties, in relation with temperature and equivalence ratio ϕ. Examples for air and combustion products are shown in the figures below.

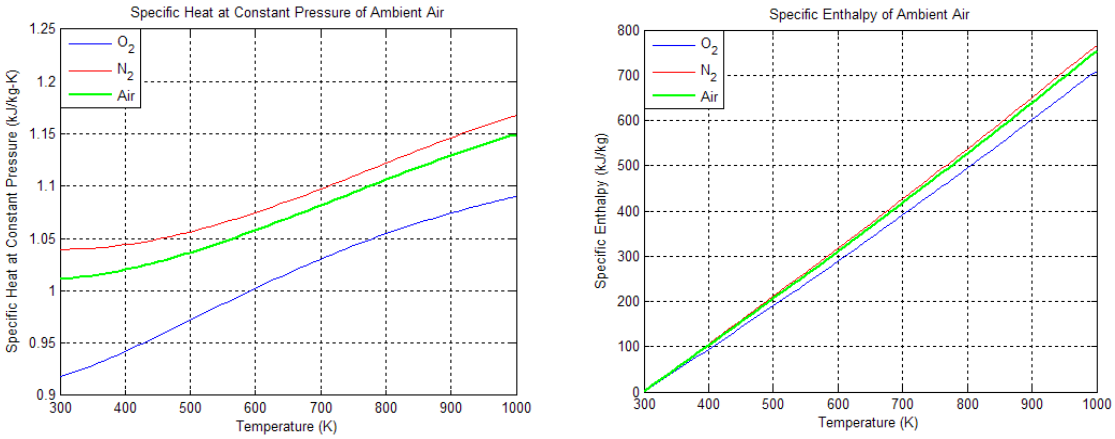

Figure 17: Specific Heat and Enthalpy for Air.

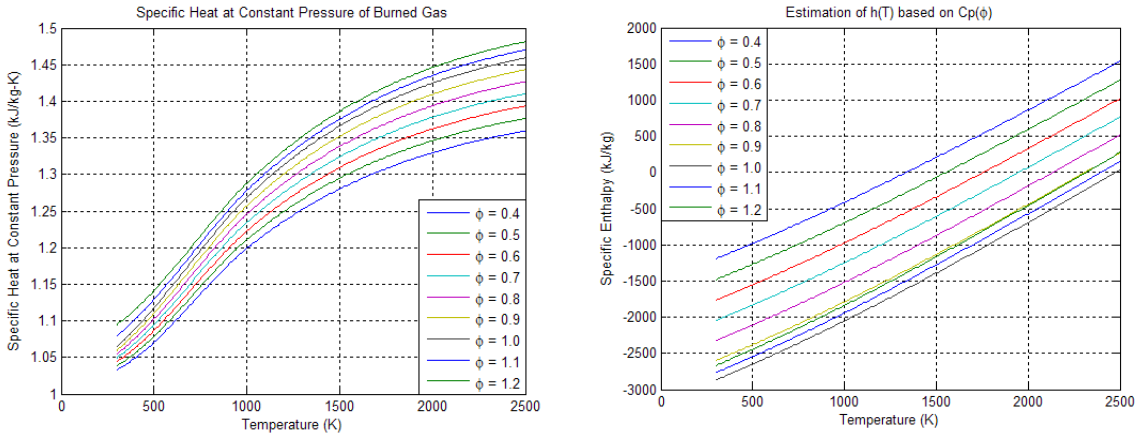

Figure 18: Specific Heat and Enthalpy for Combustion Products.

4.2.1.4 Mechanical Elements

Additional relations are required for the engine's mechanical and geometrical elements, such as the evolution of the volume within the cylinder, the torque produced by the force of the pressure on the piston, the engine's frictional losses and the dynamics of the crankshaft.

Cylinder Volume

The cylinder volume model calculates the volume of the cylinder as a function of crank angle and the cylinder geometrical parameters. The volume of the cylinder is presented in (4.28), with the inclusion of the wrist pin offset parameter ε.

$$V_{cyl}(\theta) = \frac{\pi B^2}{4}\left\{\left(\frac{L}{r_c - 1}\right) + \sqrt{(l+a)^2 - \varepsilon^2} - \sqrt{l^2 - \left(a\sin(\theta) + \varepsilon\right)^2} - a\cos(\theta)\right\} \quad (4.28)$$

For inclusion within the cylinder energy equation, the derivative of the cylinder volume is required as shown in (4.29), with initial condition defined in (4.30).

$$\frac{dV_{cyl}}{dt} = \frac{d\theta}{dt} \cdot \frac{dV_{cyl}}{d\theta} = \omega \frac{\pi B^2}{4} \left\{ a \sin(\theta) + \frac{(a \sin(\theta) + \varepsilon) a \cos(\theta)}{\sqrt{l^2 - (a \sin(\theta) + \varepsilon)^2}} \right\} \tag{4.29}$$

$$V_{cyl}(\theta = \theta_0) = \frac{\pi B^2}{4} \left\{ \left(\frac{L}{r_c - 1} \right) + \sqrt{(l + a)^2 - \varepsilon^2} - \sqrt{l^2 - (a \sin(\theta_0) + \varepsilon)^2} - a \cos(\theta_0) \right\} \tag{4.30}$$

It should be noted that the crank radius parameter generally described as $a = L/2$, is defined as shown in (4.31) to include the effect of the wrist pin offset.

$$a = \frac{L}{2} \frac{\sqrt{-L^2 + 4l^2 - 4\varepsilon^2}}{\sqrt{-L^2 + 4l^2}} \tag{4.31}$$

Indicated Torque:

The torque produced by the force of the gas on the piston is described by the indicated torque relation shown in (4.32) and can be seen to be a function of the difference between the cylinder and crank case (ambient) pressure.

$$T_i(i) = (P_{cyl}(i) - P_0) A_p a \sin(\theta) \left\{ 1 + \frac{a \sin(\theta) + \varepsilon}{\tan(\theta) \sqrt{l^2 - (a \sin(\theta) + \varepsilon)^2}} \right\} \tag{4.32}$$

Friction Torque:

The friction model describes the engine torque losses due to mechanical friction. The modeling approach followed is based upon the Chen-Flynn [100] correlation for estimating the friction mean effective pressure (FMEP) and is a function of the peak cylinder pressure, the mean piston speed and the mean piston speed squared. The coefficients $\{PF, MPSF, MPSSF\}$ are fit to experimental data.

$$T_f = num_{cyl}\left(\frac{V_d}{4\pi}\right)\left\{C + PF \cdot P_{\max} + MPSF \cdot \bar{S}_L + MPSSF \cdot \bar{S}_L{}^2\right\} \tag{4.33}$$

Where the mean piston speed is defined as:

$$\bar{S}_L = \frac{L \cdot \omega}{\pi} \tag{4.34}$$

Crankshaft Dynamics:

For simplicity, the engine crankshaft dynamics is described through a single degree of freedom dynamic model:

$$J\frac{d\omega}{dt} + B\omega = \sum_{i=1}^{Num\_cyl} T_{ind}(i) - T_f - T_l \tag{4.35}$$

4.2.2 Model Implementation and Calibration

The equations described in Section 4.2.1 are implemented in Matlab / Simulink. The implementation employs a modular structure to allow for a flexible modeling environment, easily adaptable to a wide range of engine designs. An important aspect of this structure is to develop a frame work with universal inputs and outputs to enable a *'plug-n-play'* architecture. To this end, the equations are coded in subsystems describing the major engine components (throttle, intake manifold, etc) and connected such that the model maintains a close relation to the original system. The universal input/output structure is obtained through the use of *'bus connectors'* such that each block has only two inputs (upstream and downstream conditions) and a single output. Additionally, within each subsystem block, *goto* and *from* blocks are used for signal management, but are only defined as *scoped* variables and are thus (except for a few exceptions) defined only as local variables within each subsystem. The *'plug-n-play'* architecture is further developed by *Masking* each subsystem block (a graphical user interface masking the contents of each block for the user to define the parameters of the subsystem) and creating a *Simulink Library* of the engine components. Post processing of the simulation results is facilitated through careful data management by saving the simulation results in organized fashion within *structures*.

The model calibration, simulation, validation, and post-processing of simulation results is facilitated through a comprehensive suite of graphical user interfaces (GUIs)

designed in the Matlab environment, as outlined in Appendix 8.3. To facilitate calibration of the model, the GUIs aid in calibrating the intake, cylinder and exhaust systems as described below.

Calibration of Flow Restriction Elements

The flow restriction elements shown in Figure 16 are calibrated through solving equations (4.1) - (4.3) for the effective area of the element based upon steady-state calibration data. This calibration data may contain a combination of experimental data and data generated from a higher fidelity model. For the throttle and valve flow restriction elements, the calibration has been performed utilizing experimental data, exactly as described in Section 3.3.2 for the one-dimensional model. The exhaust flow restriction element has been calibrated through employing a Virtual Engine Mapping technique [28,77,97] to calibrate the exhaust system flow losses to match that of the experimentally calibrated one-dimensional model described in Section 3.3. The results of this exhaust flow restriction calibration procedure are shown in a normalized plot at parked cam timing in Figure 19.

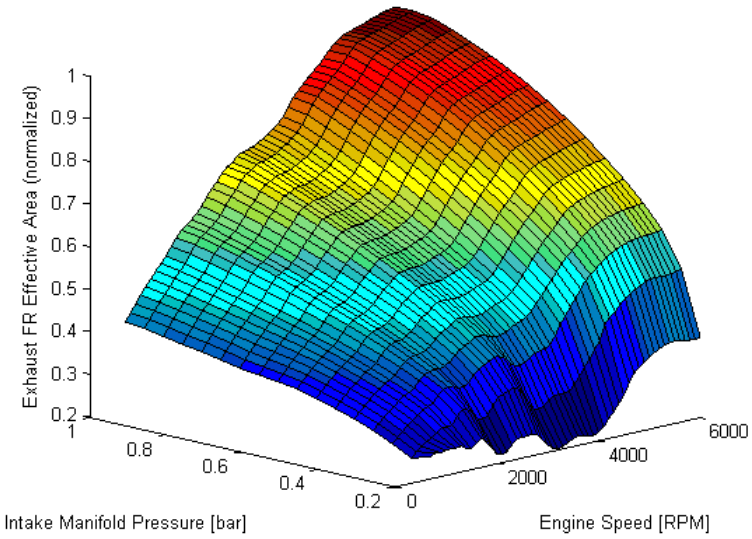

Figure 19: Exhaust Flow Restriction Effective Area at Parked Cam Timing (Normalized to One)

Calibration of Combustion Parameters

The combustion model has been calibrated in the same fashion as was done for the one-dimensional model described in Section 3.3.2, where an inverse thermodynamic model is used for calculation of the burn rate from experimentally determined cylinder pressure. The burn rate is fit to the Wiebe function model described in equation (4.17), and the resulting Wiebe function parameters are fit through regression and neural network approaches for use throughout the entire engine map.

Calibration of Manifold Wall Temperature and Heat Transfer Models:

The intake, cylinder and exhaust manifold wall temperature models, as well as the heat transfer models, have been calibrated to match the results of the experimentally calibrated one-dimensional simulation model. Specifically, intake and cylinder wall temperatures have been modeled as constant values. Since the exhaust system's wall temperature varies significantly with operating conditions, it has been described through a static look-up table as a function of engine speed and load. The heat transfer models of the intake and exhaust manifolds have subsequently been calibrated to match experimental and simulation results through applying global heat transfer modifiers to the heat transfer convection coefficients.

4.2.3 Analysis of Modeling Assumptions and Simulation Results

As a means of analyzing the predictive capability of the 0-D CAR approach, a simulation study is presented in the following, where results from the experimentally calibrated one-dimensional model from Section 3.3 are compared against results from the 0-D CAR modeling approach. The two models have been simulated over an engine speed sweep at Wide Open Throttle (WOT) to evaluate the predictive capability of the lumped parameter model. The discharge coefficients of the throttle and valves and the parameters of the Wiebe function combustion model are the same for both the 1-D and the 0-D model. In this context, it is assumed that the quasi-static phenomena that contribute to the determination of the engine volumetric efficiency, such as the

concentrated flow losses, the average heat transfer within the manifolds and the cylinder, and the choking of the flow through the throttle, intake and exhaust valves, should be equally captured by the two models. Additionally, the two models predict the low-frequency filling and emptying dynamics of the intake and exhaust systems.

Figure 20 shows the volumetric efficiency and brake torque predicted by the 0-D CAR and the 1-D gas dynamic model. At low engine speeds, the 0-D CAR is capable of accurately predicting the volumetric efficiency and thus the brake torque. However at mid and high engine speeds, the resonance peaks due to wave dynamic effects seen in the 1-D simulation results are absent from the 0-D results. Although the quasi-steady and low-frequency phenomena and their effects on the engine charge and its thermodynamic conditions are characterized in the 0-D context, it is evident that the neglected distributed and high-frequency effects considerably limit the accuracy of the lumped-parameter model.

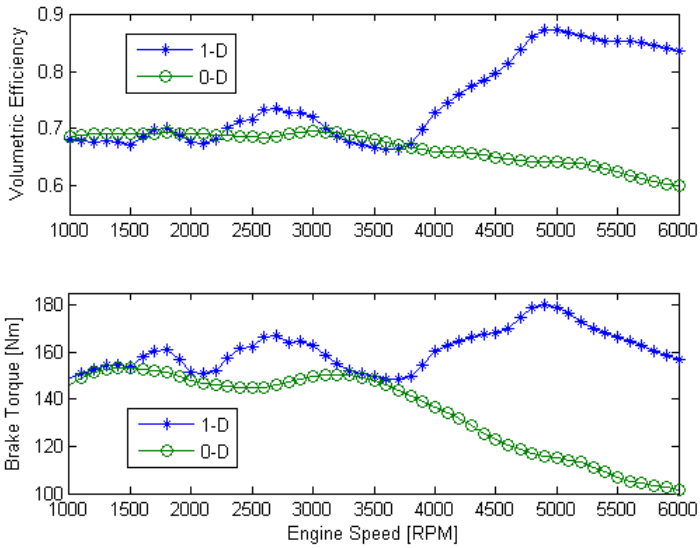

Figure 20: Volumetric Efficiency and Brake Torque Prediction at Wide Open Throttle, 0-D CAR vs. 1-D Model

The inaccuracies in volumetric efficiency prediction seen in Figure 20 in the 0-D model stem from an inaccurate prediction of the valve flows, as described by the isentropic flow relations (4.1) - (4.3). These relations can be seen to be a function of the cylinder pressure and pressure directly upstream of the intake valve. In the 1-D representation, the gas dynamic equations are solved within numerous volumes, yielding a distributed prediction of intake pressures. In the 0-D approach, on the other hand, a single lumped intake volume is used, yielding the prediction of only a single intake pressure. Figure 21 displays the intake manifold and intake port (pressure directly upstream of the valve) pressures during one engine cycle at 4900 RPM, WOT, as predicted by the 1-D gas dynamic model. Although the cycle-averaged value of the two

pressures are similar (since there is no major flow restriction between the intake manifold and the intake port), the amplitude of the fluctuations in the intake port are much greater than in the manifold. This figure can serve as a simplified analysis of the deficiencies of the 0-D approach.

Within the 1-D simulator, the pressure used to calculate the intake valve flow is the port pressure shown in Figure 21. However, in the 0-D CAR approach, only the manifold pressure shown in Figure 21 is predicted, and thus is used in the valve flow calculation. It is apparent that using the intake manifold pressure from Figure 21 as the valve upstream pressure will yield significantly different valve flows than if the port pressure is used. Thus in order to accurately predict the valve flow and ultimately the volumetric efficiency, a better representation of in the intake port conditions is required within the 0-D model. The following section describes a methodology for representing the intake port conditions in order to accurately model volumetric efficiency and torque within a lumped parameter framework.

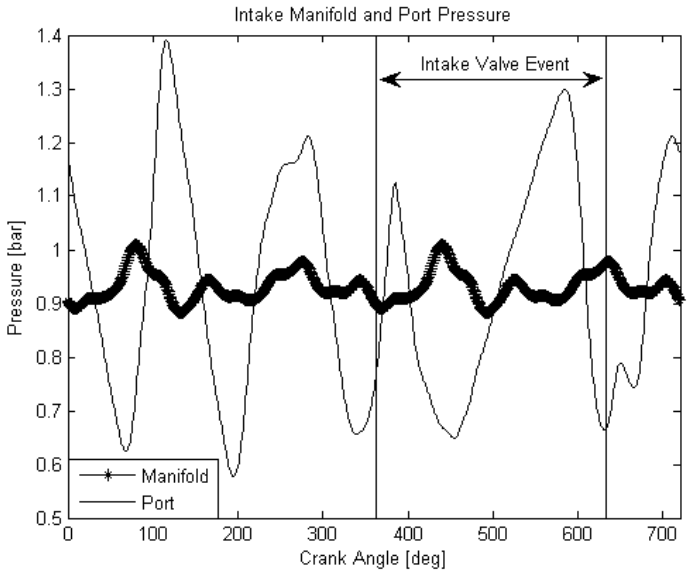

Figure 21: Intake Manifold and Port Pressure (4900 RPM, WOT)

4.3 Empirically Based Wave Dynamic Compensation

4.3.1 Improved Model Structure and Governing Equations

The 0-D model structure has the advantage of providing prediction of the in-cylinder pressure, as well as the intake and exhaust manifold pressures, with a resolution of one (or less) crank-angle degree. However, the prediction of intake and exhaust air flows is rather poor, as several phenomena (which are intrinsically high-frequency and spatially dependent) are not explicitly accounted for within a lumped-parameter framework. For control applications, such as engine torque control or air-fuel ratio

control, the cycle-averaged value of the engine cylinder charge and its composition (fresh air, fuel and residuals) is relevant.

From the above consideration, a calibration procedure has been defined to capture the phenomena not explicitly accounted for in the 0-D context. Specifically, the procedure takes into account the effects of charge heating, backflows and wave dynamics on the cycle averaged cylinder charge mass and composition, and on the mixture thermodynamic conditions at intake valve closing. This, in turn, allows for improving the prediction of the in-cylinder pressure and instantaneous engine indicated torque.

The calibration procedure begins by defining a pseudo-volume located between the intake manifold and the valves, to represent the intake port, as shown in Figure 22.

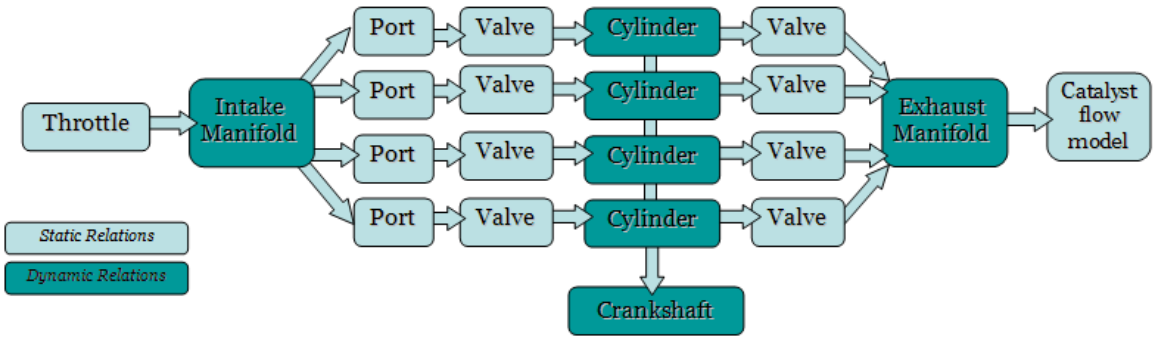

Figure 22: Advanced System Decomposition for Engine Dynamics Model

The port volumes are termed pseudo-volumes since the standard mass and energy equations (as described above) are not applied. Instead, states within the port are

modeled as cycle-averaged states (assumed to be constant within a cycle) and defined by the equations below:

$$P_{ip}^{*} = K_p \cdot \frac{1}{\theta_{IVO} - \theta_{IVC}} \cdot \int_{IVO}^{IVC} P_{IM}(\theta)\, d\theta \tag{4.36}$$

$$T_{ip}^{*} = \frac{1}{\theta_{IVO} - \theta_{IVC}} \cdot \int_{IVO}^{IVC} T_{ip}(\theta)\, d\theta \tag{4.37}$$

$$X_{exh,ip}^{*} = \frac{1}{\theta_{IVO} - \theta_{IVC}} \cdot \int_{IVO}^{IVC} X_{exh,ip}(\theta)\, d\theta \tag{4.38}$$

where the averages are taken over the crank-angle interval where the intake valve is open. Note that, in the case of the intake port pressure, a multiplier parameter K_p is defined, hence referencing to the averaged intake manifold pressure.

In order to account for the effects of charge heating, backflow, and wave dynamics, the following effects should be predicted by the 0-D model to match the results of the 1-D model:

1. *The cylinder temperature at intake valve closing.*

$$T_{cyl,IVC} = T_{cyl,IVC_{1D}} \tag{4.39}$$

2. *The mass fraction of exhaust in the cylinder at intake valve closing.*

$$X_{ex,cyl,IVC} = X_{ex,cyl,IVC_{1D}} \tag{4.40}$$

3. *The mass of air that flows through the intake valve over one cycle.*

$$\int_{IVO}^{IVC} \dot{m}_{iv} X_{air}^{*} dt = \int_{IVO}^{IVC} \dot{m}_{iv_{1D}} X_{air_{1D}} dt \tag{4.41}$$

where $X_{air}^{*} = 1 - X_{ex,ip}^{*}$.

The constraints specified above can be used to calibrate the three states within the intake port pseudo-volume. Though the above equations form a system with three equations and three unknowns, the equations depend on the cylinder pressure and hence the resulting set of equations is a set of nonlinear, differential-algebraic relations and a closed form solution is unable to be obtained. For this reason, the procedure to identify the three states involves solving the equations simultaneously by iteration.

The three pseudo-volume states are calibrated at each engine operating point and defined as constant within each engine cycle. The intake port states may be modeled for each cylinder so as to describe cylinder flow imbalances. However, for a well distributed intake systems (as in the present example) the intake port states may be modeled identically for each cylinder.

The engine speed sweep simulation is revisited here, where the algorithm described above is implemented to yield intake port states shown in Figure 23.

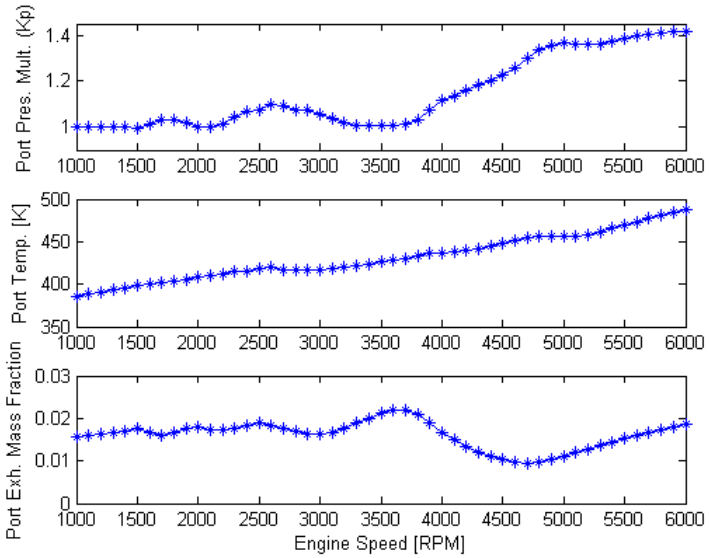

Figure 23: Calibrated Values of the Port Pressure Multiplier, Port Temperature and Port Mass Fraction of Exhaust

The intake port states may be implemented within the lumped parameter model through regression or neural network approaches as a function of the parameters affecting volumetric efficiency (engine speed, load, cam timing, etc.). The results are compared to the one dimensional gas dynamic model in Figure 24. It can be seen that the model now captures the cycle averaged parameters of volumetric efficiency and torque accurately.

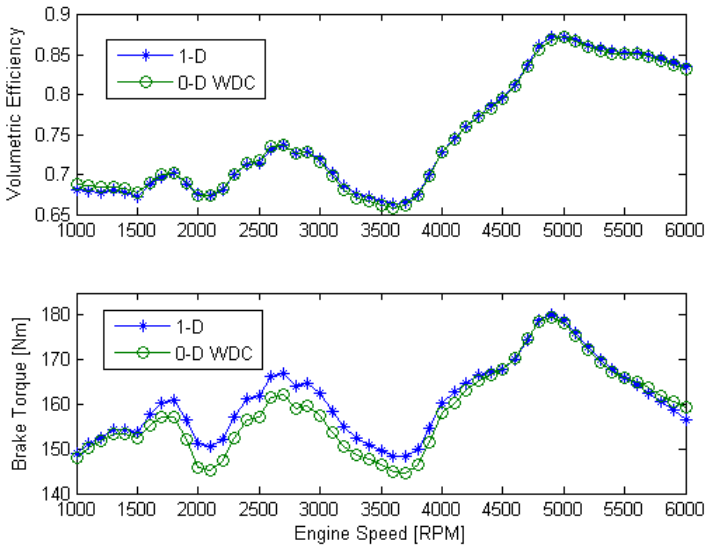

Figure 24: Volumetric efficiency and Brake Torque prediction at wide open throttle, 0-D CAR Model with Wave Dynamic Compensation (WDC) VS 1-D Model

Furthermore, Figure 25 shows that the 0-D model also captures the crank angle resolved cylinder pressure accurately.

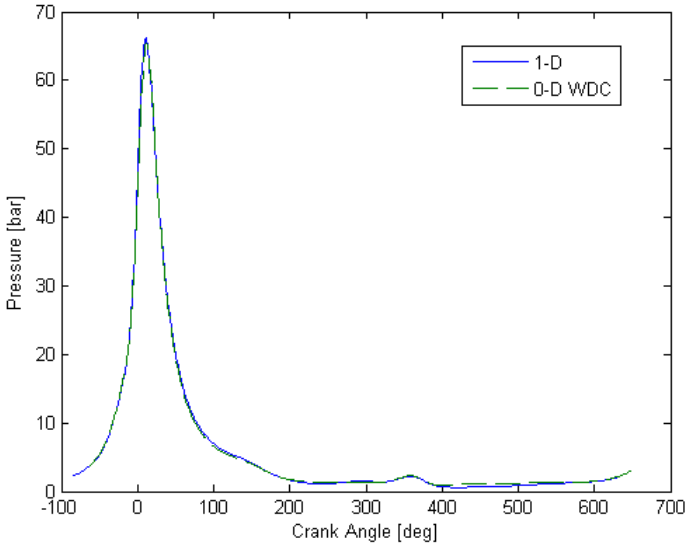

Figure 25: Cylinder Pressure Prediction [4900 RPM, WOT]

The resulting 0-D model estimates the cycle averaged variables of volumetric efficiency and mean effective pressure as well as the crank angle resolved variables of cylinder pressure and indicated torque within the accuracy of the 1-D gas dynamic model, and with computation time of an order of magnitude less.

4.3.2 Steady State Simulation Results

The proposed methodology has been applied to the full operating range of the engine described in Section 3.2. The model calibration is done by utilizing a virtual engine mapping approach, where the experimentally calibrated 1-D gas dynamic model is used in place of experiments [28,77,97]. The procedure is structure as follows:

1. The 1-D gas dynamic engine model is calibrated and validated against the set of experimental points collected on the engine;

2. Using the 1-D simulator, a full-factorial DOE is generated in the four dimensional space of engine speed, intake manifold pressure, intake and exhaust cam timing, covering the entire engine operating range.

3. Using the data generated from simulation, the 0-D model is calibrated at each point to within +-2% absolute error in volumetric efficiency.

4. The response of the 0-D model is validated first against the 1-D simulator, and then on an additional set of experimental data, different from the calibration set used in (1).

Following the procedure outlined above, the calibrated port parameters were then implemented in the model as a four dimensional look-up table, as functions of engine speed, intake manifold pressure, intake and exhaust cam timing. Figure 26 shows the map of the intake pressure parameter at parked cam timing, while Figure 27 shows the intake port temperature and mass fraction of exhaust.

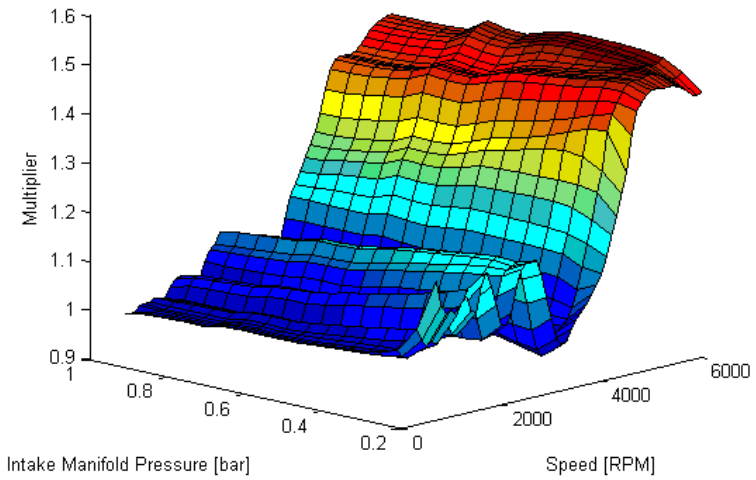

Figure 26: Intake Port Pressure Multiplier at Parked Cam Timing

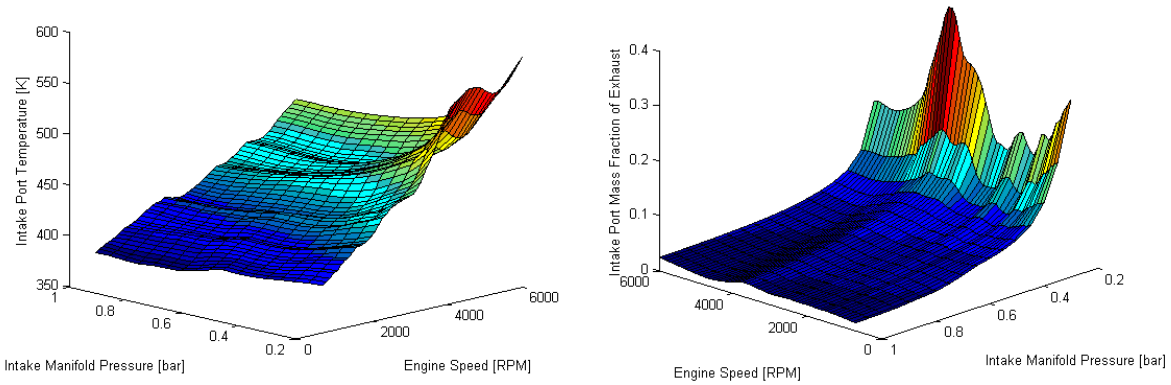

Figure 27: Intake Port Parameters; Left: Temperature, Right: Mass Fraction of Exhaust

For the final validation phase, the 0-D model was compared against 800 experimental operating points obtained in steady-state conditions. The results of the advanced 0-D CAR model as applied to these validation points are compared against the

1-D gas dynamic model and experimental data in Figure 28 and Figure 29. Figure 28 shows that the zero-dimensional, lumped-parameter model predicts volumetric efficiency in the entire validation range with good agreement to the one-dimensional model, within a 3% error. It can be seen in Figure 29, that the zero-dimensional, lumped-parameter model predicts volumetric efficiency accurately with respect to the experimental data. The increase in error can be attributed to the modeling error of the 1-D gas dynamic model from which the 0-D model was calibrated against.

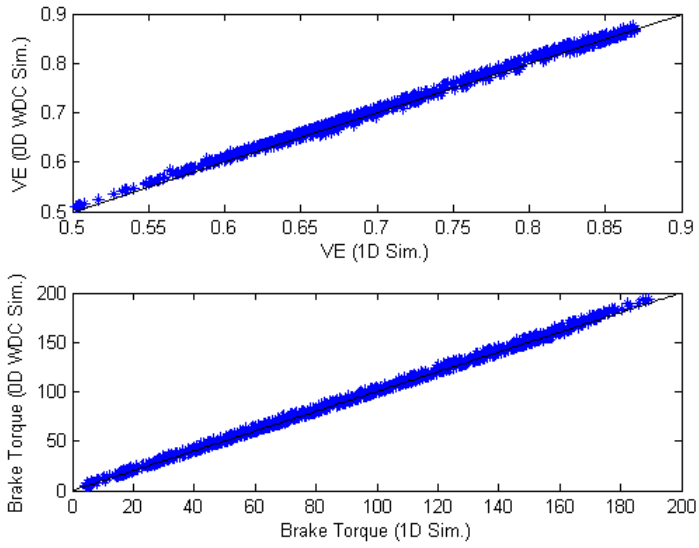

Figure 28: Comparison of volumetric efficiency and brake Torque between 1-D model and 0-D Model with Wave Dynamic Compensation (WDC)

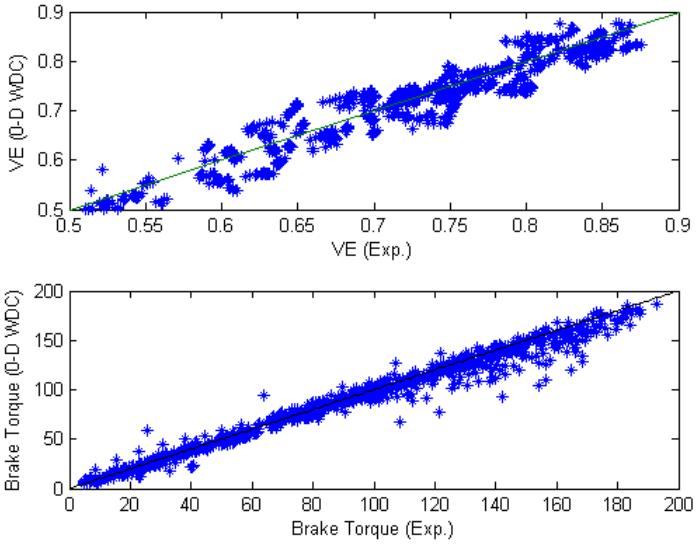

Figure 29: Comparison of Volumetric Efficiency and Brake Torque Between 0-D Model with Wave Dynamic Compensation and Experimental Data

4.4 Conclusions

The crank angle resolved, zero-dimensional modeling methodology has been described in detail and evaluated on a case study of a four cylinder, spark ignited engine. In comparison to simulation results from a one-dimensional gas dynamic model, it is clear that the 0-D methodology provides a simpler, more computationally efficient architecture, but is incapable of predicting wave dynamic effects within the engine's intake and exhaust systems. This deficiency can lead to errors in prediction of volumetric efficiency and brake torque as high as 30%, significantly reducing the attractiveness of the approach.

To compensate for the deficiency of the 0-D CAR mode, a novel empirical approach has been developed to allow the 0-D model to achieve cycle-resolved values of volumetric efficiency, manifold pressure and brake torque as well as crank angle resolved values of cylinder pressure and brake torque to within an accuracy level of a one-dimensional model, while maintaining a simple and computational efficient model architecture. The approach has been applied to the full operating map of an engine with variable valve timing and shown to match both one-dimensional simulation and experimental results with a high level accuracy.

CHAPTER 5

METHODOLOGY FOR FORMAL MODEL ORDER REDUCTION OF COMPRESSIBLE FLUID SYSTEMS

5.1 Introduction

The modeling study described in the previous chapter presented a novel technique for modeling the gas dynamics of engine intake systems using zero-dimensional modeling supplemented by specific empirical calibration. The result is a computationally efficient, crank angle resolved model suitable for control systems design. In the present chapter, similar goals are achieved through a formal model order reduction procedure, beginning from the full set of conservation laws. In this approach, the compressible fluid flow system is modeled through the use of a low order set of ordinary differential equations, allowing for a high level of fidelity yet with a simple model structure and low computational effort.

The chapter is structured such that the model order reduction procedure is presented first, followed by a description of basis functions evaluated within the context of the reduction procedure. Finally, in-depth equations are presented detailing the model

order reduction process as applied to the equations of gas dynamics and their approximations.

5.2 Model Order Reduction Procedure

The model order reduction procedure begins from the governing, one dimensional, hyperbolic partial differential equations and utilizes a defined Spatial Basis Function (SBF) to permit a reduction from a distributed parameter model to a lumped volume-based model. Such an approach (with the appropriate SBF) allows for a low order ODE-based description of the distributed parameter model, hence more amenable to control systems applications.

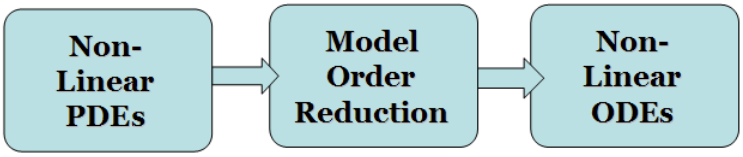

Figure 30: Model Order Reduction Process

Specifically, the model order reduction procedure follows the following algorithm:

1. Beginning from the differential form of the governing partial differential equation, define a generic control volume encompassing a portion of the system and perform a spatial integration about the control volume.

2. Through the spatial integration and definition of volume average variables, the partial differential equation is converted to an ordinary differential equation in terms of the spatial average variable and fluxes entering and leaving the control volume.

3. A definition of the Spatial Basis Function closes the equation set, coupling the known volume average state with that of the unknown flux quantities.

5.3 Definition of Spatial Basis Functions

The simple procedure defined in the previous section may be applied to one-dimensional hyperbolic partial differential equations or equation sets with a variety of Spatial Basis Functions. Candidate basis functions can be defined through mathematical convenience, relevance to the underlying physics, or experimental or simulation-based techniques. Examples of such basis functions include that of a polynomial, trigonometric or wavelet representation. For the purpose of the present study, the evaluation will be limited to polynomial-based representations due to their inherent mathematical convenience, with extensions to more elaborate basis functions left as future work.

5.3.1 Piecewise Constant

Within a polynomial representation, the simplest implementation is that of a piecewise constant representation. Such a representation assumes that the volume average states are defined to be spatially constant within a volume, with a jump discontinuity at

volume boundaries, where care must be taken to define the value at the boundary. This assumption is analogous to that of the conventional System Dynamics approach, whereby a “well mixed” assumption of states is employed to define that “what leaves the volume is that which is at the center of the volume”. A simple analysis of this approach leads to the understanding that the method must be adapted to the direction of propagation, in that in the event of flow reversal, the flux must be defined following an upwind mentality.

5.3.2 Piecewise Linear

Intuitively, the next representation is that of a piecewise linear model. This method will result in the definition of the flux at the boundaries as the average of the upstream and downstream volume average states (for constant spatial discretizations).

5.3.3 Piecewise Quadratic

The third basis function is that of a quadratic representation. This implementation requires the knowledge of three volume averages (two upstream, one down) for determination of a volume’s exiting flux. Like the constant basis function, this method will require an adaptive implementation based upon the direction of propagation.

5.3.4 Piecewise Cubic

The final basis function explored in the present study is that of the cubic function. This representation requires the knowledge of two volume average states upstream and

two downstream of the flux location. This method, like the linear representation, has the advantage of not requiring an adaptive representation.

5.4 Application to Fundamental Equations and Their Approximations

The four chosen basis functions (constant, linear, quadratic, cubic) are implemented in the present section on the gas dynamic equations and their approximations, following the model order reduction procedure defined in Section 5.2. Specifically, the model order reduction procedure will be applied to one-dimensional versions of the Linear Convection Equation, linear Euler equations and the full Euler equations based upon these four basis functions. A mathematical derivation will be included for each of the equation sets with a constant basis function, while the remainder of the derivations are included in Appendix 8.4, with the final results summarized for convenience.

5.4.1 Linear Convection Equation

The Linear Convection Equation, previously defined in Chapter 2, is reiterated in equation (5.1) below.

$$\frac{\partial u(x,t)}{\partial t} + c \cdot \frac{\partial u(x,t)}{\partial x} = 0 \tag{5.1}$$

The model order reduction process from Section 5.2 can be applied to this equation, by first performing a spatial integration about (5.1) within a generic control volume of length L:

$$\int_0^L \frac{\partial u(x,t)}{\partial t} \cdot dx + \int_0^L c \cdot \frac{\partial u(x,t)}{\partial x} \cdot dx = 0 \tag{5.2}$$

The spatial integration eliminates the partial derivative with respect to distance, allowing equation (5.2) to be simplified to:

$$\int_0^L \frac{\partial u(x,t)}{\partial t} \cdot dx = c\left(u(t, x=0) - u(t, x=L)\right) \tag{5.3}$$

Next, we can define the spatial average value of the state u within the control volume i as shown in (5.4). Note that the superscript asterisk denotes a spatial average variable assigned to the control volume denoted by the subscript (in this case: control volume i). The spatial averaging, performed through a definite integral and assigned to specific control volume permits the state u to now only be a function of time.

$$u_i^*(t) = \frac{1}{L}\int_0^L u(x,t) \cdot dx \tag{5.4}$$

Differentiating (5.4) with respect to time, yields the relation shown in (5.5).

$$\frac{du_i^*(t)}{dt} = \frac{1}{L}\int_0^L \frac{\partial u(x,t)}{\partial t} \cdot dx \tag{5.5}$$

This relation can be applied to (5.3) to yield the ordinary differential equation shown below.

$$\frac{du_i^*(t)}{dt} = \frac{c}{L}\left(u(t, x=0) - u(t, x=L)\right) \tag{5.6}$$

Equation (5.6) relates the spatial average state within our control volume i to the fluxes entering and leaving the control volume. Note that this equation applied to a series of control volumes is not sufficient for obtaining a solution; a relation has not yet been defined between the state calculated from (5.6) and that of the fluxes entering and leaving the control volume. The definition of the basis function establishes the link between the spatial average state and that of the fluxes.

Also note that the flux leaving control volume i must, by definition, be the same as the flux entering the adjacent control volume in the flow direction (*i.e.* in the case of forward traveling flow: the flux leaving control volume i is equal to the flux entering control volume $i+1$). Subsequently, defining the spatial basis function and establishing a correlation for the flux leaving the control volume in terms of spatial average variables is sufficient (it is not necessary to define the relationship for the flux entering the control volume since it is simply the flux leaving the upstream control volume). With this in mind, the following derivation will establish a link between the flux leaving the control volume as a function of spatial average variables.

In the simplest representation, we assume a piecewise constant basis function (with respect to the longitudinal direction x) as defined in (5.7) to establish the relationship between the spatial average state and that of the exiting flux.

$$u(x,t)\Big|_0^L = \alpha_1(t) \tag{5.7}$$

We can then establish an analytic relationship for the spatial average state by applying equation (5.7) to (5.4):

$$u_i^*(t) = \frac{1}{L}\int_0^L u(x,t)\cdot dx = \frac{1}{L}\int_0^L \alpha_1(t)\cdot dx = \alpha_1(t) \tag{5.8}$$

Summarizing, the basis function (and thus the state u) can be written as:

$$u(x,t)\Big|_0^L = u_i^*(t) \tag{5.9}$$

Using this relationship, the flux exiting the control volume can now be written as a function of the spatial average variables:

$$u(t, x = L) = u_i^*(t) \tag{5.10}$$

Similar derivations are presented in Appendix 8.4.1 for the linear, quadratic and cubic basis functions. The results can be summarized as follows:

The ordinary differential equation governing the spatial average state within a control volume is defined as a function of the fluxes entering and leaving the control volume through the relationship in (5.11).

$$\frac{du_i^*(t)}{dt} = \frac{c}{L}\left(u(t, x=0) - u(t, x=L)\right) \tag{5.11}$$

This relationship is completely defined through identifying the flux leaving the control volume (as discussed previously, the definition of the flux entering the control volume is not needed). This relationship is summarized in Table 7 for polynomial basis functions.

Spatial Basis Function	**Exiting Flux**
Constant	$u(t, x=L) = u_i^*$
Linear	$u(t, x=L) = \frac{u_i^* + u_{i+1}^*}{2}$
Quadratic	$u(t, x=L) = -\frac{1}{6}u_{i-1}^* + \frac{5}{6}u_i^* + \frac{1}{3}u_{i+1}^*$
Cubic	$u(t, x=L) = -\frac{1}{12}u_{i-1}^* + \frac{7}{12}u_i^* + \frac{7}{12}u_{i+1}^* - \frac{1}{12}u_{i+2}^*$

Table 7: Flux Exiting Control Volume i of Linear Convection Equation with Polynomial Basis Functions

5.4.2 Linear Euler Equations

A similar derivation can be performed for the linear version of the Euler equations, previously introduced in Chapter 2. The linear set is shown in differential

form in equations (5.12) and (5.13). It can be seen that the equation set is a function of two space and time dependent states: density (ρ) and velocity (u).

$$\frac{\partial \rho(x,t)}{\partial t} + u_0 \frac{\partial \rho(x,t)}{\partial x} + \rho_0 \frac{\partial u(x,t)}{\partial x} = 0 \tag{5.12}$$

$$\frac{\partial u(x,t)}{\partial t} + u_0 \frac{\partial u(x,t)}{\partial x} + \frac{c^2}{\rho_0} \frac{\partial \rho(x,t)}{\partial x} = 0 \tag{5.13}$$

Beginning with the linear continuity equation (5.12), we again apply the model order reduction process from Section 5.2, where we first perform a spatial integration within a generic control volume.

$$\int_0^L \frac{\partial \rho(x,t)}{\partial t} \cdot dx + \int_0^L u_0 \frac{\partial \rho(x,t)}{\partial x} \cdot dx + \int_0^L \rho_0 \frac{\partial u(x,t)}{\partial x} \cdot dx = 0 \tag{5.14}$$

Again, the spatial integration eliminates the partial derivative with respect to the coordinate x, allowing equation (5.14) to be simplified to:

$$\int_0^L \frac{\partial \rho(x,t)}{\partial t} \cdot dx = u_0 \left(\rho(t, x=0) - \rho(t, x=L) \right) + \rho_0 \left(u(t, x=0) - u(t, x=L) \right) \tag{5.15}$$

We can define the spatial average value of the density (ρ) within volume i as:

$$\rho_i^*(t) = \frac{1}{L} \int_0^L \rho(x,t) \cdot dx \tag{5.16}$$

Differentiating (5.16) with respect to time yields:

$$\frac{d\rho_i^*(t)}{dt} = \frac{1}{L}\int_0^L \frac{\partial \rho(x,t)}{\partial t}\cdot dx \tag{5.17}$$

Relation (5.17) can be applied to (5.15) to yield an ordinary differential equation for the spatial average value of the density within control volume i.

$$\frac{d\rho_i^*(t)}{dt} = \frac{u_0}{L}\left(\rho(t,x=0)-\rho(t,x=L)\right)+\frac{\rho_0}{L}\left(u(t,x=0)-u(t,x=L)\right) \tag{5.18}$$

Next, integrating the momentum equation about a control volume that is staggered with respect to the continuity volume yields:

$$\int_{.5L}^{1.5L}\frac{\partial u(x,t)}{\partial t}\cdot dx + \int_{.5L}^{1.5L} u_0\frac{\partial u(x,t)}{\partial x}\cdot dx + \int_{.5L}^{1.5L}\frac{c^2}{\rho_0}\frac{\partial \rho(x,t)}{\partial x}\cdot dx = 0 \tag{5.19}$$

This relation simplifies to:

$$\int_{.5L}^{1.5L}\frac{\partial u(x,t)}{\partial t}\cdot dx = u_0\left(u\left(t,x=\frac{L}{2}\right)-u\left(t,x=\frac{3L}{2}\right)\right)+\frac{a^2}{\rho_0}\left(\rho\left(t,x=\frac{L}{2}\right)-\rho\left(t,x=\frac{3L}{2}\right)\right) \tag{5.20}$$

The spatial average value of velocity (u) within volume j can be defined as:

$$u_j^*(t) = \frac{1}{L}\int_{.5L}^{1.5L} u(x,t)\cdot dx \tag{5.21}$$

Differentiating (5.21) with respect to time yields:

$$\frac{du_j^*(t)}{dt} = \frac{1}{L}\int_{.5}^{1.5L} \frac{\partial u(x,t)}{\partial t} \cdot dx \tag{5.22}$$

Equation (5.22) can be applied (5.20) to yield:

$$\frac{du_j^*(t)}{dt} = u_0\left(u\left(t, x=\frac{L}{2}\right) - u\left(t, x=\frac{3L}{2}\right)\right) + \frac{c^2}{\rho_0}\left(\rho\left(t, x=\frac{L}{2}\right) - \rho\left(t, x=\frac{3L}{2}\right)\right) \tag{5.23}$$

We now have two governing ordinary differential equations for the control volumes i and j, but require the relationship between the spatial average variables and that of the fluxes. Beginning again from the simplest representation, piecewise constant basis functions for the two staggered volumes can be defined within their respective control volumes as:

$$\rho(x,t)\Big|_0^L = \alpha_1(t) \tag{5.24}$$

$$u(x,t)\Big|_{.5L}^{1.5L} = \beta_1(t) \tag{5.25}$$

Based upon these basis functions, the spatial average variables can be defined as:

$$\rho_i^*(t) = \frac{1}{L}\int_0^L \alpha_1(t) \cdot dx = \alpha_1(t) \tag{5.26}$$

$$u_j^*(t) = \frac{1}{L}\int_{.5L}^{1.5L} \beta_1(t) \cdot dx = \beta_1(t) \tag{5.27}$$

Thus the basis functions can be written as:

$$\rho(x,t)\Big|_0^L = \rho_i^*(t) \tag{5.28}$$

$$u(x,t)\Big|_{.5L}^{1.5L} = u_j^*(t) \tag{5.29}$$

The fluxes of density and velocity leaving control volumes i and j can now be found:

$$u(t, x = L) = u_j^*(t) \tag{5.30}$$

$$u\left(t, x = \frac{3L}{2}\right) = u_j^*(t) \tag{5.31}$$

$$\rho(t, x = L) = \rho_i^*(t) \tag{5.32}$$

$$\rho\left(t, x = \frac{3L}{2}\right) = \rho_{i+1}^*(t) \tag{5.33}$$

Summarizing, the ordinary differential equations governing the spatial average states of density and velocity within the staggered control volumes i and j are defined as a function of the fluxes entering and leaving the control volumes through the relationships in (5.34) and (5.35).

$$\frac{d\rho_i^*(t)}{dt} = \frac{u_0}{L}\left(\rho(t, x = 0) - \rho(t, x = L)\right) + \frac{\rho_0}{L}\left(u(t, x = 0) - u(t, x = L)\right) \tag{5.34}$$

$$\frac{du_j^*(t)}{dt} = u_0\left(u\left(t, x=\frac{L}{2}\right) - u\left(t, x=\frac{3L}{2}\right)\right) + \frac{a^2}{\rho_0}\left(\rho\left(t, x=\frac{L}{2}\right) - \rho\left(t, x=\frac{3L}{2}\right)\right) \quad (5.35)$$

These relationships are completely defined through the definition of the flux leaving the control volume. This relationship is summarized in Table 8 and Table 9 for polynomial basis functions.

Basis Function	**Flux Exiting Mass and Energy Volume**	**Flux Exiting Momentum Volume**
Constant	$\rho(t, x=L) = \rho_i^*$	$\rho\left(t, x=\frac{3L}{2}\right) = \rho_{i+1}^*$
Linear	$\rho(t, x=L) = \frac{\rho_i^* + \rho_{i+1}^*}{2}$	$\rho\left(t, x=\frac{3L}{2}\right) = \rho_{i+1}^*$
Quadratic	$\rho(t, x=L) = -\frac{1}{6}\rho_{i-1}^* + \frac{5}{6}\rho_i^* + \frac{1}{3}\rho_{i+1}^*$	$\rho\left(t, x=\frac{3L}{2}\right) = -\frac{1}{24}\rho_{i-1}^* + \frac{1}{12}\rho_i^* + \frac{23}{24}\rho_{i+1}^*$
Cubic	$\rho(t, x=L) = -\frac{1}{12}\rho_{i-1}^* + \frac{7}{12}\rho_i^* + \frac{7}{12}\rho_{i+1}^* - \frac{1}{12}\rho_{i+2}^*$	$\rho\left(t, x=\frac{3L}{2}\right) = -\frac{1}{24}\rho_i^* + \frac{13}{12}\rho_{i+1}^* - \frac{1}{24}\rho_{i+2}^*$

Table 8: Density Flux Exiting Control Volumes i and j of Linear Euler Equations with Polynomial Basis Functions

Basis Function	Flux Exiting Mass and Energy Volume	Flux Exiting Momentum Volume
Constant	$u\left(t, x=L\right)=u_j^*$	$u\left(t, x=\frac{3L}{2}\right)=u_j^*$
Linear	$u\left(t, x=L\right)=u_j^*$	$u\left(t, x=\frac{3L}{2}\right)=\frac{u_j^*+u_{j+1}^*}{2}$
Quadratic	$u\left(t, x=L\right)=-\frac{1}{24}u_{j-1}^*+\frac{13}{12}u_j^*-\frac{1}{24}u_{j+1}^*$	$u\left(t, x=\frac{3L}{2}\right)=-\frac{1}{6}u_{j-1}^*+\frac{5}{6}u_j^*+\frac{1}{3}u_{j+1}^*$
Cubic	$u\left(t, x=L\right)=-\frac{1}{24}u_{j-1}^*+\frac{13}{12}u_j^*-\frac{1}{24}u_{j+1}^*$	$u\left(t, x=\frac{3L}{2}\right)=-\frac{1}{12}u_{j-1}^*+\frac{7}{12}u_j^*+\frac{7}{12}u_{j+1}^*-\frac{1}{12}u_{j+2}^*$

Table 9: Velocity Flux Exiting Control Volumes i and j of Linear Euler Equations with Polynomial Basis Functions

5.4.3 Euler Equations

The model order reduction process is repeated here for the one-dimensional, constant area Euler Equations shown in differential form in equations (5.36) - (5.38) below. This version of the equation set can be seen to be a function of five space and time varying quantities: density $\left(\rho\right)$, total internal energy $\left(e_0\right)$, velocity $\left(u\right)$, total enthalpy $\left(h_0\right)$ and pressure $\left(P\right)$.

$$\frac{\partial\left(\rho\left(x,t\right)A\right)}{\partial t}+\frac{\partial\left(\rho\left(x,t\right)Au\left(x,t\right)\right)}{\partial x}=0 \tag{5.36}$$

$$\frac{\partial\left(\rho\left(x,t\right)Au\left(x,t\right)\right)}{\partial t}+\frac{\partial\left(\rho\left(x,t\right)Au\left(x,t\right)^2+P\left(x,t\right)A\right)}{\partial x}=0 \tag{5.37}$$

$$\frac{\partial\left(\rho(x,t)\,Ae_0(x,t)\right)}{\partial t}+\frac{\partial\left(\rho(x,t)\,Au(x,t)\,h_0(x,t)\right)}{\partial x}=0 \tag{5.38}$$

For ease of analysis, these equations are modified by defining the mass flux of gas traveling within the components, the pressure and the enthalpy as follows :

$$\dot{m}(x,t)=\rho(x,t)\,Au(x,t) \tag{5.39}$$

$$P(x,t)=(\gamma-1)\rho(x,t)\left(e_0-\frac{\dot{m}(x,t)^2}{2\rho(x,t)^2A^2}\right) \tag{5.40}$$

$$h_0(x,t)=e_0(x,t)+\frac{P(x,t)}{\rho(x,t)}=\gamma e_0(x,t)+(1-\gamma)\frac{\dot{m}(x,t)^2}{2\rho(x,t)^2A^2} \tag{5.41}$$

Applying the relations in (5.39) - (5.41) to equations (5.36) - (5.38) yields a version of the Euler equations in three space and time varying quantities: density (ρ), total internal energy (e_0), and mass flux $(\dot{m})$.

$$\frac{\partial\left(\rho(x,t)\,A\right)}{\partial t}+\frac{\partial\dot{m}(x,t)}{\partial x}=0 \tag{5.42}$$

$$\frac{\partial\dot{m}(x,t)}{\partial t}+\frac{\partial\left((\gamma-1)\rho(x,t)\,Ae_0(x,t)+\dfrac{\dot{m}(x,t)^2(3-\gamma)}{2\rho(x,t)\,A}\right)}{\partial x}=0 \tag{5.43}$$

$$\frac{\partial\left(\rho(x,t)Ae_0(x,t)\right)}{\partial t}+\frac{\partial\left(\gamma\dot{m}(x,t)e_0(x,t)+(1-\gamma)\dfrac{\dot{m}(x,t)^3}{2\rho(x,t)^2A^2}\right)}{\partial x}=0 \qquad (5.44)$$

Beginning first with the continuity equation and applying the model order reduction process from Section 5.2, we perform a spatial integration within the generic control volume:

$$\int_0^L \frac{\partial\left(\rho(x,t)A\right)}{\partial t}\cdot dx+\int_0^L \frac{\partial\dot{m}(x,t)}{\partial x}\cdot dx=0 \qquad (5.45)$$

The spatial integration eliminates the partial derivatives with respect to distance, simplifying (5.45) to:

$$\int_0^L \frac{\partial\left(\rho(x,t)A\right)}{\partial t}\cdot dx=\dot{m}(t,x=0)-\dot{m}(t,x=L) \qquad (5.46)$$

The spatial average value of the density (ρ) within control volume i can be defined as:

$$\rho_i^*(t)=\frac{1}{L}\int_0^L \rho(x,t)\cdot dx \qquad (5.47)$$

Differentiating (5.47) with respect to time yields:

$$\frac{d\rho_i^*(t)}{dt}=\frac{1}{L}\int_0^L \frac{\partial\rho(x,t)}{\partial t}\cdot dx \qquad (5.48)$$

Relation (5.48) can be applied to (5.46) to yield an ordinary differential equation for the spatial average variable of the density within control volume i:

$$AL\frac{d\rho_i^*(t)}{dt} = \dot{m}(t, x=0) - \dot{m}(t, x=L) \tag{5.49}$$

We next turn our attention to the conservation of energy and integrate about the same control volume:

$$\int_0^L \frac{\partial\left(\rho(x,t)Ae_0(x,t)\right)}{\partial t}\cdot dx + \int_0^L \frac{\partial\left(\gamma\dot{m}(x,t)e_0(x,t) + (1-\gamma)\dfrac{\dot{m}(x,t)^3}{2\rho(x,t)^2A^2}\right)}{\partial x}\cdot dx = 0 \tag{5.50}$$

Again, the integration eliminates terms such that equation (5.50) simplifies to:

$$\begin{aligned}\int_0^L \frac{\partial\left(\rho(x,t)Ae_0(x,t)\right)}{\partial t}\cdot dx &= \gamma\dot{m}(t,x=0)e_0(t,x=0) + (1-\gamma)\frac{\dot{m}(t,x=0)^3}{2\rho(t,x=0)^2A^2} - \ldots \\ &\gamma\dot{m}(t,x=L)e_0(t,x=L) - (1-\gamma)\frac{\dot{m}(t,x=L)^3}{2\rho(t,x=L)^2A^2}\end{aligned} \tag{5.51}$$

The spatial average value of the product of the density and the total internal energy (ρe_0) within control volume i can be defined as:

$$(\rho e_0)_i^*(t) = \frac{1}{L}\int_0^L \rho(x,t)e_0(x,t)\cdot dx \tag{5.52}$$

Differentiating (5.52) with respect to time yields:

$$\frac{d\left(\rho e_0\right)_i^*(t)}{dt}=\frac{1}{L}\int_0^L\frac{\partial\left(\rho(x,t)e_0(x,t)\right)}{\partial t}\cdot dx \tag{5.53}$$

Relation (5.53) can be applied to (5.51) to yield an ordinary differential equation for the spatial average variable of the product of density and energy within control volume i:

$$\begin{aligned}AL\frac{d\left(\rho e_0\right)_i^*(t)}{dt}&=\gamma\dot{m}(t,x=0)e_0(t,x=0)+(1-\gamma)\frac{\dot{m}(t,x=0)^3}{2\rho(t,x=0)^2A^2}-\ldots\\&\gamma\dot{m}(t,x=L)e_0(t,x=L)-(1-\gamma)\frac{\dot{m}(t,x=L)^3}{2\rho(t,x=L)^2A^2}\end{aligned} \tag{5.54}$$

Finally, concentrating on the momentum equation, we integrate about a control volume that is staggered with respect to the continuity and energy volume to yield:

$$\int_{.5L}^{1.5L}\frac{\partial\dot{m}(x,t)}{\partial t}\cdot dx+\int_{.5L}^{1.5L}\frac{\partial\left((\gamma-1)\rho(x,t)Ae_0(x,t)+\frac{\dot{m}(x,t)^2(3-\gamma)}{2\rho(x,t)A}\right)}{\partial x}\cdot dx=0 \tag{5.55}$$

The integration eliminates derivatives such that equation (5.55) simplifies to:

$$\begin{aligned}\int_{.5L}^{1.5L}\frac{\partial\dot{m}(x,t)}{\partial t}\cdot dx&=(\gamma-1)\rho\left(t,x=\frac{L}{2}\right)Ae_0\left(t,x=\frac{L}{2}\right)+\frac{\dot{m}\left(t,x=\frac{L}{2}\right)^2(3-\gamma)}{2\rho\left(t,x=\frac{L}{2}\right)A}-\ldots\\&(\gamma-1)\rho\left(t,x=\frac{3L}{2}\right)Ae_0\left(t,x=\frac{3L}{2}\right)-\frac{\dot{m}\left(t,x=\frac{3L}{2}\right)^2(3-\gamma)}{2\rho\left(t,x=\frac{3L}{2}\right)A}\end{aligned} \tag{5.56}$$

The spatial average value of mass flux $(\dot{m})$ within control volume j can be defined as:

$$\dot{m}_j^*(t) = \frac{1}{L}\int_{.5L}^{2.5L} \dot{m}(x,t)\cdot dx \tag{5.57}$$

Differentiating (5.57) with respect to time yields:

$$\frac{d\dot{m}_j^*(t)}{dt} = \frac{1}{L}\int_{.5L}^{2.5L} \frac{\partial \dot{m}(x,t)}{\partial t}\cdot dx \tag{5.58}$$

Equation (5.58) can be applied to (5.56) to yield an ordinary differential equation for the spatial average variable of the mass flux within control volume i:

$$\begin{aligned} L\frac{d\dot{m}_j^*(t)}{dt} = (\gamma-1)\rho\left(t,x=\frac{L}{2}\right)Ae_0\left(t,x=\frac{L}{2}\right) + \frac{\dot{m}\left(t,x=\frac{L}{2}\right)^2(3-\gamma)}{2\rho\left(t,x=\frac{L}{2}\right)A} - \ldots \\ (\gamma-1)\rho\left(t,x=\frac{3L}{2}\right)Ae_0\left(t,x=\frac{3L}{2}\right) - \frac{\dot{m}\left(t,x=\frac{3L}{2}\right)^2(3-\gamma)}{2\rho\left(t,x=\frac{3L}{2}\right)A} \end{aligned} \tag{5.59}$$

We now have three governing ordinary differential equations for the control volumes i and j and require the relationship between the spatial average variables and that of the fluxes. Starting from the simplest representation, piecewise constant basis functions are defined within two separate sets of control volumes: the first contains a single control

volume where basis functions are defined for the density and for the total internal energy; the second, staggered from the first, contains a single control volume for the mass flux basis function:

$$\rho(x,t)\Big|_0^L = \alpha_1(t) \tag{5.60}$$

$$e_0(x,t)\Big|_0^L = \beta_1(t) \tag{5.61}$$

$$\dot{m}(x,t)\Big|_{.5L}^{1.5L} = \chi_1(t) \tag{5.62}$$

Based upon these basis functions, the spatial average variables can be defined as:

$$\rho_i^*(t) = \frac{1}{L}\int_0^L \alpha_1 \cdot dx = \alpha_1(t) \tag{5.63}$$

$$(e_0)_i^*(t) = \frac{1}{L}\int_0^L \beta_1 \cdot dx = \beta_1(t) \tag{5.64}$$

$$\dot{m}_j^*(t) = \frac{1}{L}\int_{.5L}^{1.5L} \chi_1 \cdot dx = \chi_1(t) \tag{5.65}$$

Thus the basis functions can be written as:

$$\rho(x,t)\Big|_0^L = \rho_i^*(t) \tag{5.66}$$

$$e_0(x,t)\Big|_0^L = e_{0,i}^*(t) \tag{5.67}$$

$$\dot{m}\left(x,t\right)\Big|_{.5L}^{1.5L} = \dot{m}_j^*\left(t\right) \tag{5.68}$$

Furthermore, we can see that spatial average quantity of the product of the density and the internal energy can be written as:

$$\left(e_0\rho\right)_i^*\left(t\right) = \frac{1}{L}\int_0^L \alpha_1\left(t\right)\cdot\beta_1\left(t\right)\cdot dx = \alpha_1\left(t\right)\cdot\beta_1\left(t\right) \tag{5.69}$$

Such that:

$$\left(e_0\rho\right)_i^*\left(t\right) = e_{0,i}^*\left(t\right)\cdot\rho_i^*\left(t\right) \tag{5.70}$$

The fluxes of density, velocity, and internal energy leaving control volumes i and j can now be found:

$$\rho\left(t, x = L\right) = \rho_i^*\left(t\right) \tag{5.71}$$

$$\rho\left(t, x = \frac{3L}{2}\right) = \rho_{i+1}^*\left(t\right) \tag{5.72}$$

$$e_0\left(t, x = L\right) = e_{0,i}^*\left(t\right) \tag{5.73}$$

$$e_0\left(t, x = \frac{3L}{2}\right) = e_{0,i+1}^*\left(t\right) \tag{5.74}$$

$$\dot{m}\left(t, x = L\right) = \dot{m}_j^*\left(t\right) \tag{5.75}$$

$$\dot{m}\left(t, x=\frac{3L}{2}\right)=\dot{m}_j^*(t) \tag{5.76}$$

Summarizing, the ordinary differential equations governing the spatial average states of density, total internal energy, and mass flux within the staggered control volumes i and j are defined as a function of the fluxes entering and leaving the control volumes through the relationships in (5.77) - (5.79).

$$AL\frac{d\rho_i^*(t)}{dt}=\dot{m}(t,x=0)-\dot{m}(t,x=L) \tag{5.77}$$

$$\begin{aligned} AL\frac{d\left(\rho e_0\right)_i^*(t)}{dt}&=\gamma\dot{m}(t,x=0)e_0(t,x=0)+(1-\gamma)\frac{\dot{m}(t,x=0)^3}{2\rho(t,x=0)^2A^2}-\ldots \\ &\gamma\dot{m}(t,x=L)e_0(t,x=L)-(1-\gamma)\frac{\dot{m}(t,x=L)^3}{2\rho(t,x=L)^2A^2}\end{aligned} \tag{5.78}$$

$$\begin{aligned} L\frac{d\dot{m}_j^*(t)}{dt}&=(\gamma-1)\rho\left(t,x=\frac{L}{2}\right)Ae_0\left(t,x=\frac{L}{2}\right)+\frac{\dot{m}\left(t,x=\frac{L}{2}\right)^2(3-\gamma)}{2\rho\left(t,x=\frac{L}{2}\right)A}-\ldots \\ &(\gamma-1)\rho\left(t,x=\frac{3L}{2}\right)Ae_0\left(t,x=\frac{3L}{2}\right)-\frac{\dot{m}\left(t,x=\frac{3L}{2}\right)^2(3-\gamma)}{2\rho\left(t,x=\frac{3L}{2}\right)A}\end{aligned} \tag{5.79}$$

These relationships are fully defined through the definition of the flux leaving the control volumes. This relationship is summarized in Table 10 - Table 13 for polynomial basis functions.

Basis Function	Flux Exiting Continuity Volume	Flux Exiting Momentum Volume
Constant	$\rho\left(t, x = L\right) = \rho_i^*$	$\rho\left(t, x = \frac{3L}{2}\right) = \rho_{i+1}^*$
Linear	$\rho\left(t, x = L\right) = \frac{\rho_i^* + \rho_{i+1}^*}{2}$	$\rho\left(t, x = \frac{3L}{2}\right) = \rho_{i+1}^*$
Quadratic	$\rho\left(t, x = L\right) = \frac{-\rho_{i-1}^* + 5\rho_i^* + 2\rho_{i+1}^*}{6}$	$\rho\left(t, x = \frac{3L}{2}\right) = -\frac{1}{24}\rho_{i-1}^* + \frac{1}{12}\rho_i^* + \frac{23}{24}\rho_{i+1}^*$
Cubic	$\rho\left(t, x = L\right) = \frac{-\rho_{i-1}^* + 7\rho_i^* + 7\rho_{i+1}^* - \rho_{i+2}^*}{12}$	$\rho\left(t, x = \frac{3L}{2}\right) = -\frac{1}{24}\rho_i^* + \frac{13}{12}\rho_{i+1}^* - \frac{1}{24}\rho_{i+2}^*$

Table 10: Density Flux Exiting Control Volumes i and j of Euler Equations with Polynomial Basis Functions

Basis Function	Flux Exiting Continuity Volume	Flux Exiting Momentum Volume
Constant	$e_0\left(t, x = L\right) = e_{0,i}^*$	$e_0\left(t, x = \frac{3L}{2}\right) = e_{0,i+1}^*$
Linear	$e_0\left(t, x = L\right) = \frac{e_{0,i}^* + e_{0,i+1}^*}{2}$	$e_0\left(t, x = \frac{3L}{2}\right) = e_{0,i+1}^*$
Quadratic	$e_0\left(t, x = L\right) = \frac{-e_{0,i-1}^* + 5e_{0,i}^* + 2e_{0,i+1}^*}{6}$	$e_0\left(t, x = \frac{3L}{2}\right) = -\frac{1}{24}e_{0,i-1}^* + \frac{1}{12}e_{0,i}^* + \frac{23}{24}e_{0,i+1}^*$
Cubic	$e_0\left(t, x = L\right) = \frac{-e_{0,i-1}^* + 7e_{0,i}^* + 7e_{0,i+1}^* - e_{0,i+2}^*}{12}$	$e_0\left(t, x = \frac{3L}{2}\right) = -\frac{1}{24}e_{0,i}^* + \frac{13}{12}e_{0,i+1}^* - \frac{1}{24}e_{0,i+2}^*$

Table 11: Energy Flux Exiting Control Volumes i and j of Euler Equations with Polynomial Basis Functions

Basis Function	Flux Exiting Continuity Volume	Flux Exiting Momentum Volume
Constant	$\dot{m}\left(t, x=L\right)=\dot{m}_j^*$	$\dot{m}\left(t, x=\frac{3L}{2}\right)=\dot{m}_j^*$
Linear	$\dot{m}\left(t, x=L\right)=\dot{m}_j^*$	$\dot{m}\left(t, x=\frac{3L}{2}\right)=\frac{\dot{m}_j^*+\dot{m}_{j+1}^*}{2}$
Quadratic	$\dot{m}\left(t, x=L\right)=-\frac{1}{24}\dot{m}_{j-1}^*+\frac{13}{12}\dot{m}_j^*-\frac{1}{24}\dot{m}_{j+1}^*$	$\dot{m}\left(t, x=\frac{3L}{2}\right)=-\frac{1}{6}\dot{m}_{j-1}^*+\frac{5}{6}\dot{m}_j^*+\frac{1}{3}\dot{m}_{j+1}^*$
Cubic	$\dot{m}\left(t, x=L\right)=-\frac{1}{24}\dot{m}_{j-1}^*+\frac{13}{12}\dot{m}_j^*-\frac{1}{24}\dot{m}_{j+1}^*$	$\dot{m}\left(t, x=\frac{3L}{2}\right)=-\frac{1}{12}\dot{m}_{j-1}^*+\frac{7}{12}\dot{m}_j^*+\frac{7}{12}\dot{m}_{j+1}^*-\frac{1}{12}\dot{m}_{j+2}^*$

Table 12: Mass Flux Exiting Control Volumes i and j of Euler Equations with Polynomial Basis Functions

Basis Function	Spatial Average Product of Density and Energy
Constant	$\left(e_0\rho\right)_i^*=e_{0,i}^*\cdot\rho_i^*$
Linear	$\left(e_0\rho\right)_i^*=\left(\frac{13}{12}\rho_i^*-\frac{1}{12}\rho_{i+1}^*\right)e_{0,i}^*+\left(-\frac{1}{12}\rho_i^*+\frac{1}{12}\rho_{i+1}^*\right)e_{0,i+1}^*$
Quadratic	$\left(e_0\rho\right)_i^*=\left(\frac{1}{45}\rho_{i-1}^*-\frac{1}{360}\rho_i^*-\frac{7}{360}\rho_{i+1}^*\right)e_{0,i-1}^*+\left(-\frac{1}{360}\rho_{i-1}^*+\frac{181}{180}\rho_i^*-\frac{1}{360}\rho_{i+1}^*\right)e_{0,i}^*+\ldots$ $\left(-\frac{7}{360}\rho_{i-1}^*-\frac{1}{360}\rho_i^*+\frac{1}{45}\rho_{i+1}^*\right)e_{0,i+1}^*$
Cubic	$\left(e_0\rho\right)_i^*=\left(\frac{59}{6048}\rho_{i-1}^*+\frac{59}{5040}\rho_i^*-\frac{53}{2016}\rho_{i+1}^*+\frac{73}{15120}\rho_{i+2}^*\right)e_{0,i-1}^*+\ldots$ $\left(\frac{59}{5040}\rho_{i-1}^*+\frac{10391}{10080}\rho_i^*-\frac{257}{5040}\rho_{i+1}^*+\frac{17}{2016}\rho_{i+2}^*\right)e_{0,i}^*+\ldots$ $\left(-\frac{53}{2016}\rho_{i-1}^*-\frac{257}{5040}\rho_i^*+\frac{941}{10080}\rho_{i+1}^*-\frac{9}{560}\rho_{i+2}^*\right)e_{0,i+1}^*+\ldots$ $\left(\frac{73}{15120}\rho_{i-1}^*+\frac{17}{2016}\rho_i^*-\frac{9}{560}\rho_{i+1}^*+\frac{17}{6048}\rho_{i+2}^*\right)e_{0,i+2}^*$

Table 13: Spatial Average Product of Density and Energy of Euler Equations

5.5 Conclusions

A formal model order reduction procedure has been defined whereby sets of hyperbolic partial differential equations can be reduced to volume-based ordinary differential equations. The procedure begins by defining a generic control volume and spatially integrating about that control volume to define ordinary differential equations in the spatial average variables. The reduction process then employs the use of Spatial Basis Functions to establish a relationship between the spatial average quantities and that of the fluxes entering and leaving the control volumes. The SBF may be defined based upon mathematical convenience, relevance to the underlying physics, or experimental or simulation-based techniques. Within the context of the present work, polynomial-based representations have been evaluated due to their inherent mathematical convenience, with extensions to more elaborate basis functions left as future work.

In depth derivations of this approach have been presented in this chapter and in the Appendix for the Linear Convection equation, linear Euler equations, and Euler equations based upon the polynomial basis functions of constant, linear, quadratic and cubic. In the following chapter, the model order reduction approach and the corresponding basis functions will be evaluated against analytic and simulation results as to their ability to model the underlying physical processes while maintaining a low order ordinary differential equation structure.

CHAPTER 6

APPLICATION OF FORMAL MODEL ORDER REDUCTION OF COMPRESSIBLE FLUID SYSTEMS

6.1 Introduction

The model order reduction procedure introduced in the previous chapter is evaluated in following sections with respect to its ability to employ a low order, ordinary differential equation structure to adequately model the underlying distributed phenomena of the governing partial differential equations. The evaluation will be performed by identifying prototype scenarios to evaluate the gas dynamic equations and their approximations. These case studies have been selected to mimic conditions of engine intake and exhaust systems, while having either analytic or high fidelity computational results to benchmark against. Specifically, the Linear Convection and linear Euler equations will be evaluated on a simple traveling wave scenario against analytic solutions. The four basis functions introduced in the previous chapter will be evaluated for these scenarios against standard numerical methods and amongst themselves to highlight the advantages of the model order reduction technique. The final validation employs the full set of Euler equations evaluated on a simplified engine platform,

benchmarked against computational results from a well established, high-fidelity commercial software package, due to the absence of an analytic solution.

6.2 Case Studies and Simulation Results

6.2.1 Linear Convection Equation

As a means to evaluate the model order reduction technique on the Linear Convection equation, a case study of a simple traveling wave is devised. The case study is designed to model a single wave travelling at the speed of sound within a straight pipe of infinite length. The speed of sound, and thus the speed of the wave, is calculated assuming air at ambient temperature through equation (6.1).

$$c = \sqrt{\gamma RT} = \sqrt{1.4 \cdot 287\left[\frac{J}{kg \cdot K}\right] \cdot 298[K]} = 346\left[\frac{m}{s}\right] \tag{6.1}$$

For simplicity, the amplitude of the wave has been set to one, while the frequency of the wave has been selected to approach the upper limit of frequency relevant to a performance simulation for a defined engine platform.

The fundamental frequency of an engine at a given speed is defined in equation (6.2). It can be seen that the maximum fundamental frequency will be at the highest engine speed.

$$f_{fund} = \frac{N \cdot Num_{cyl}}{120} \tag{6.2}$$

For a four cylinder engine, taking 6000 RPM as the upper limit of engine speed, the fundamental frequency can be seen to be $f_{fund} = 200[Hz]$. For a detailed performance simulation, the fundamental frequency and its subsequent harmonics can be relevant. However, for the present case study we will use the first harmonic of the fundamental frequency at 6000 RPM of a four cylinder engine, $f = 400[Hz]$, as the wave frequency to approximate the bandwidth required for an engine performance simulation.

Additional parameters must be specified for the case study, as outlined in Table 14. This includes parameters such as the distance the wave travels within the simulation, the Courant number, and the spatial discretization. To mimic the travel of a wave through an engine's intake and exhaust system, the distance travelled has been defined to be five meters. The Courant number and the spatial discretization have been chosen to be consistent with that used by standard numerical methods [16].

Parameter	Value
Wave Speed	346 m/s
Amplitude	1
Frequency	400 Hz
Wave length	.865 m
Distance travelled	5 m
Courant (CFL) number	.8
Spatial discretization	.0346 m
Volumes per Wavelength	25

Table 14: Linear Convection Equation Case Study Parameters

As discussed in Chapter 2, the Linear Convection equation has a simple analytic solution for a defined initial spatial profile, as shown in (6.3). Since the wave speed is constant for the simulation, the solution at any time, t, is simply the initial profile shifted spatially by the product of the wave speed and the time t.

$$u(x,t) = u_0(x - ct) \tag{6.3}$$

Utilizing the parameters and the known solution from above, the benchmark for the simulations is the analytic solution shown in Figure 31, for the initial and final simulation times.

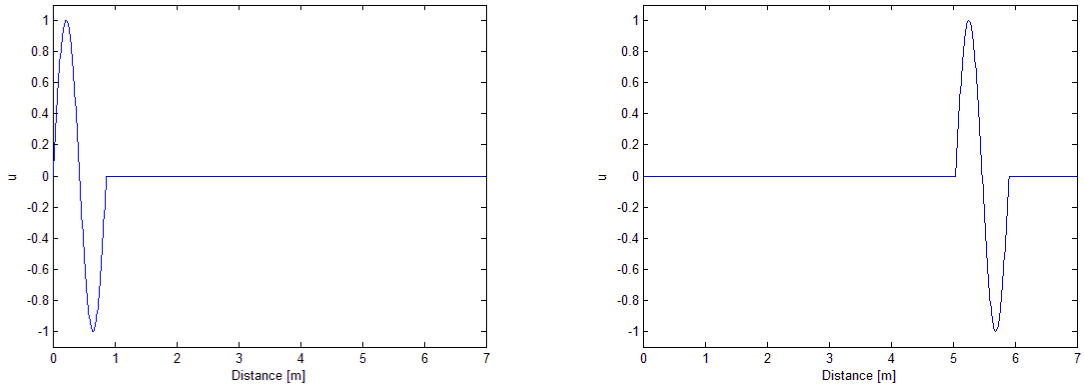

Figure 31: Linear Convection Equation Case Study Analytic Solution; Left: Initial Time; Right: Final Time

For comparison purposes, results are presented first for two standard numerical methods: the first order upwind method and the second order Lax-Wendroff method. Derivations

of these two approaches as applied to the Linear Convection equation may be found in Appendix 8.5.1. It should be noted that, unlike the proposed model order reduction technique, these two methods are derived specifically to be used with their own time stepping algorithms. Thus the simulation results presented in Figure 32 and Figure 34 are performed using their respective time stepping algorithms, while the simulations with the SBFs are performed with a fourth order Runge-Kutta time stepping algorithm [132].

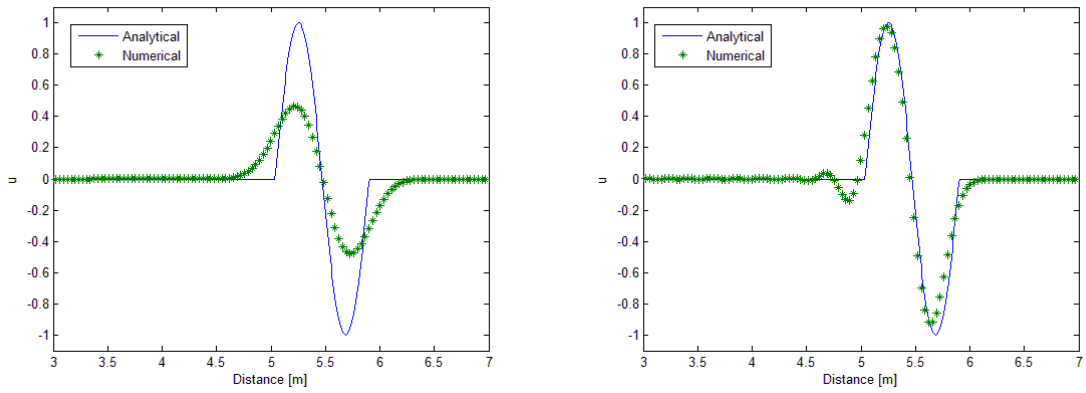

Figure 32: Linear Convection Equation Case Study Numeric Solution; Left: First Order Upwind Numerical Method; Right: Lax-Wendroff Numerical Method

Figure 32 exemplifies the characteristics of first and second order methods. The first order upwind method on the left displays significant smearing. The smearing is caused by numerical dissipation, which is a consequence of the numerical approximations inherent to the algorithm[15]. The second order Lax-Wendroff method on the right matches the analytical results better but contains dispersion with spurious oscillations.

Since these two methods have been devised with a specific time stepping algorithm in mind, they do not lend themselves to be described neither through ordinary differential equations, nor through conventional ODE solvers. The methods have been derived through a combined space and time discretization, yielding a set of discrete equations (see Appendix 8.5.1). If one then converts these equations to an equivalent differential equation and applies a conventional ODE solver (Fourth Order Runge-Kutta [132]), the dissipation and dispersion seen previously are magnified, as shown in Figure 33.

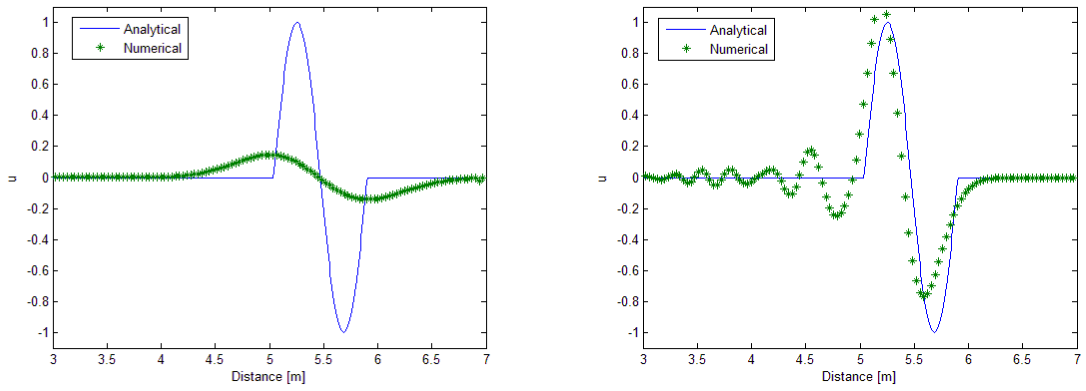

Figure 33: Linear Convection Equation; Left: First Order Upwind Method with 4th Order Runge-Kutta; Right: Lax-Wendroff Method with 4th Order Runge-Kutta

In conjunction with this, these two methods have been derived as a function of the Courant number. Thus using their intended time stepping algorithms, the accuracy of the simulation results will be dependent upon the Courant number. Intuitively, for a fixed time step, the accuracy of the simulation results will increase for a decreasing spatial

discretization (assuming the Courant condition is satisfied). This also means that for a fixed spatial discretization, the simulation results will change based upon the time step. This yields the unintuitive results shown in Figure 34, where the accuracy of the simulation results for both the first order upwind and the Lax-Wendroff method worsen as the time step is decreased.

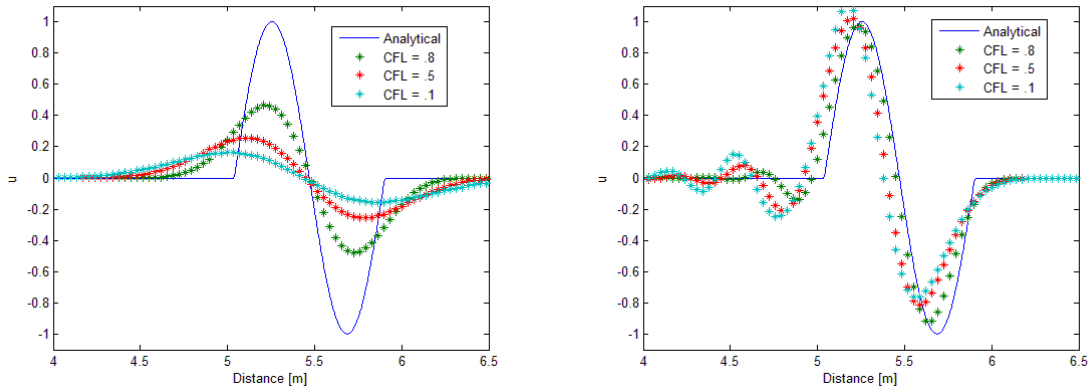

Figure 34: Linear Convection Equation Case Study Numeric Solution; Left: First Order Upwind Method with Varying CFL; Right: Lax-Wendroff Method with Varying CFL

The unintuitive results shown in Figure 33 and Figure 34 stem from the fact that these methods have been developed with a combined space and time discretization and with an intended (fixed) Courant number. These stipulations do not lend themselves to an ordinary differential equation structure, and thus run contrary to the system dynamics approach.

The next set of simulation results have been performed using the proposed model order reduction technique with the basis functions of constant, linear, quadratic and cubic. These simulations have been performed with a Fourth Order Runge-Kutta [132] time stepping algorithm. The results are presented in Figure 35, for the constant and linear basis functions.

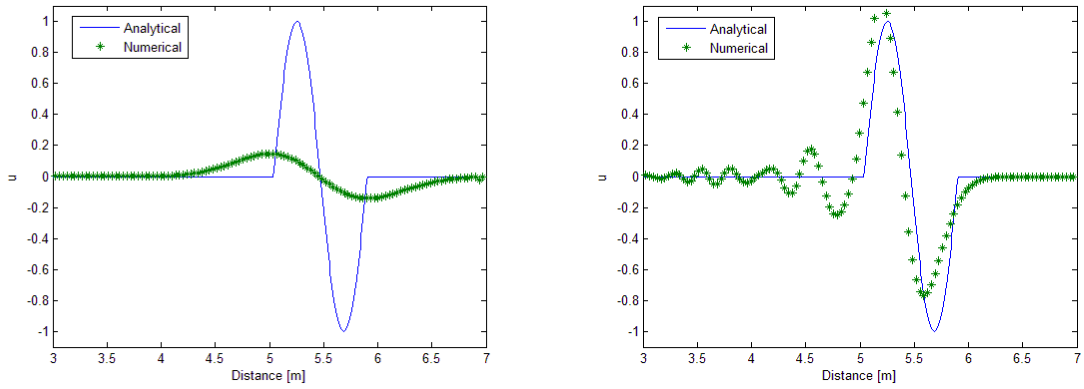

Figure 35: Linear Convection Equation Case Study Numeric Solution; Left: Constant Basis Function; Right: Linear Basis Function

Figure 35 shows that the constant and linear basis functions perform analogously to that of the first order upwind and the Lax-Wendroff method with the higher order time stepping algorithm. The constant basis function method contains significant dissipation, while the linear method contains spurious oscillations.

Figure 36, however, displays the benefits of the model order reduction technique and the sensitivity to the basis functions. The results in Figure 36 with the quadratic and

cubic basis functions can be seen to be a great improvement over the constant and linear basis functions. Both the quadratic and the cubic methods match the analytic results well, with the cubic method showing slightly less dissipation.

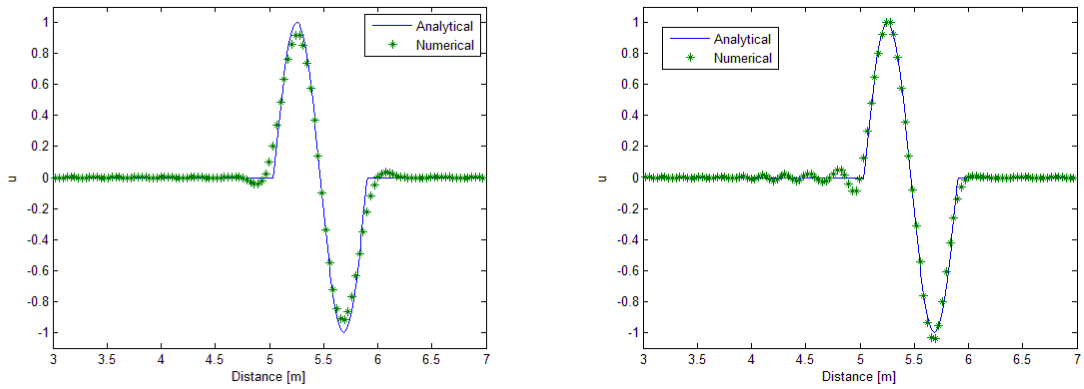

Figure 36: Linear Convection Equation Case Study Numeric Solution; Left: Quadratic Basis Function; Right: Cubic Basis Function

Furthermore, the results in Figure 37 show that since the model order reduction technique is based upon ordinary differential equations and conventional ODE solvers, the simulation results are insensitive to changes in the time step, assuming that the Courant criterion is satisfied.

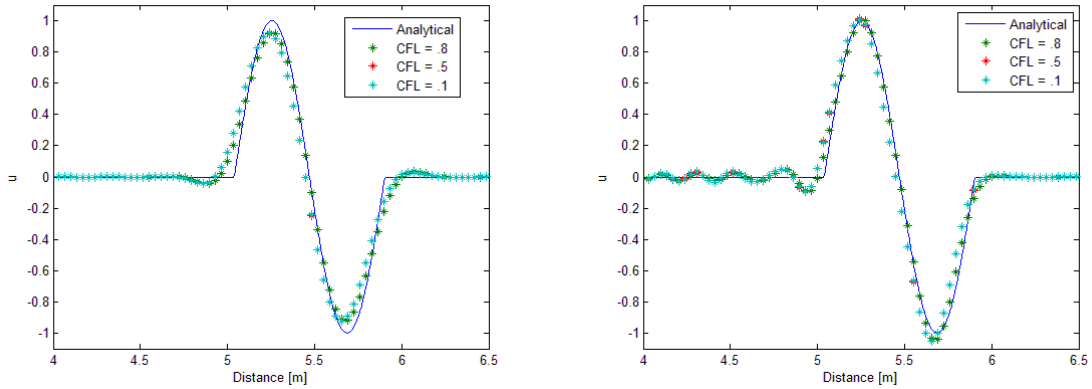

Figure 37: Linear Convection Equation Case Study Numeric Solution; Left: Quadratic Basis Function with Varying CFL; Right: Cubic Basis Function with Varying CFL

The above results have been presented showing the effect of varying the time step and the time stepping algorithm for the methods of interest with a defined simulation time (and thus a defined distance that the wave has travelled). The next case study evaluates the methods for varying distance travelled by the wave, as well as for varying spatial discretizations.

After some consideration, it is clear that the further the wave travels, the more error will accumulate in the numerical solution. Also intuitive, is that as the spatial discretization is decreased, the accuracy of the numerical simulation increases. These hypotheses are explored in the following case study for each of the basis function methods and the two standard numerical methods.

The previous case study is modified such that the simulation time is lengthened to permit the wave to travel 50 meters and the simulation is repeated for different spatial discretizations. The details of the second case study are shown in Table 15.

Parameter	Value
Wave Speed	346 m/s
Amplitude	1
Frequency	400 Hz
Wave length	.865 m
Distance travelled	50 m
Courant (CFL) number	.8
Spatial discretization	[.0346, .0432 .0721 .0692] m
Volumes per Wavelength	[25, 20, 15, 12.5]

Table 15: Linear Convection Equation Case Study II Parameters

The results of the second case study are shown in the following figures, where the Root Mean Square of the percent error, as defined in (6.4), is plotted as a function of the distance travelled by the wave and the spatial discretization. The RMS percent error has been chosen as a metric to evaluate how closely the numerical results match the analytic results at a given distance the wave has travelled.

$$RMS_{PE} = \sqrt{\frac{\sum\left[100\left(\frac{u_{analytical} - u_{numerical}}{\max\left(\left|u_{analytical}\right|\right)}\right)\right]^2}{N}} \tag{6.4}$$

In Figure 38, the results are plotted for the first order upwind and the Lax-Wendroff methods. It can be seen that the RMS error decreases for decreasing spatial

discretization, the error accumulates as the wave travels. The first order upwind method, even with a smaller discretization, only yields low RMS error for a very short period of wave travel. The Lax-Wendroff method can be seen to be an improvement upon this method in that the error grows more slowly with wave travel.

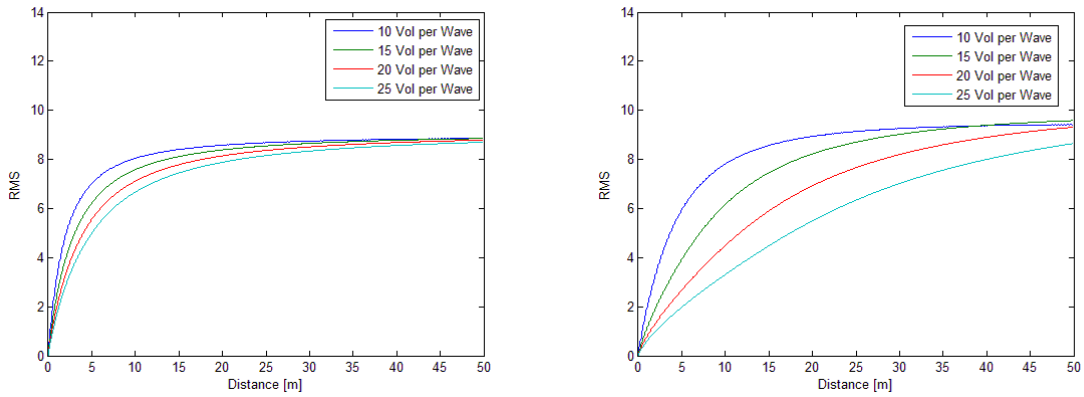

Figure 38: Linear Convection Equation Case Study II: RMS Percent Error vs. Distance Travelled; Left: First Order Upwind Method; Right: Lax-Wendroff Method

The results for the constant and linear basis functions are shown in Figure 39. These two methods perform slightly worse than the first order upwind and Lax-Wendroff methods, though if a 4^{th} order Runge-Kutta time stepping algorithm were used for the two numerical methods, the results would be identical.

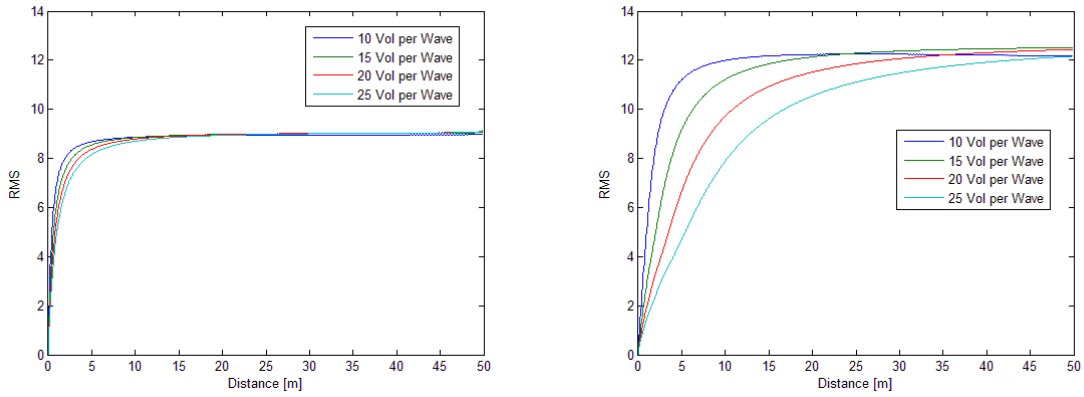

Figure 39: Linear Convection Equation Case Study II: RMS Percent Error vs. Distance Travelled; Left: Constant Basis Function; Right: Linear Basis Function

The results for the quadratic and cubic basis functions are shown in Figure 40. These results validate the superiority of these two basis functions over the constant and linear basis functions, as well as over the first order upwind and Lax-Wendroff methods. It can be seen that, particularly for the smaller spatial discretizations, the error accumulates much slower with these two basis functions, than was seen in the previous results. An alternative way of looking at these results is that for a system of defined length (and thus defined wave travel) the quadratic or cubic basis functions can be used with a larger spatial discretization to yield the same error level as the previous methods.

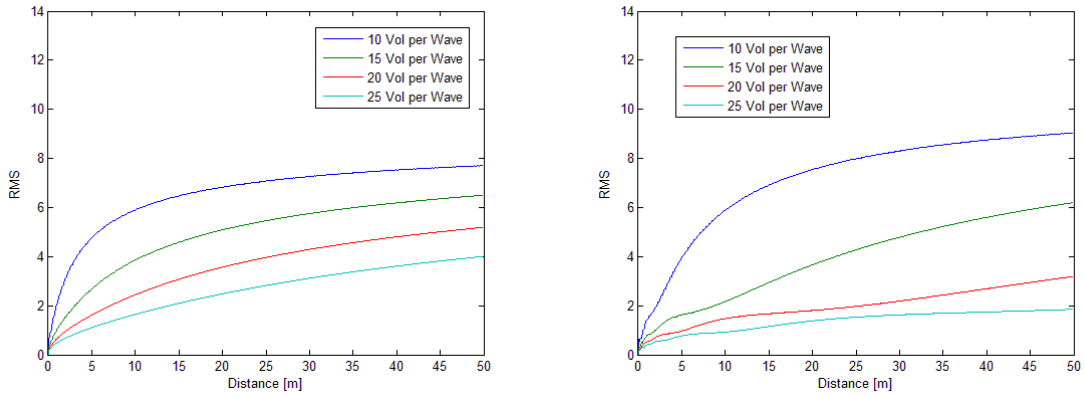

Figure 40: Linear Convection Equation Case Study II: RMS Percent Error vs. Distance Travelled; Left: Quadratic Basis Function; Right: Cubic Basis Function

6.2.2 Linear Euler Equations

Similar case studies are repeated here for the linear Euler equations. The linear Euler equations, as discussed in Chapter 2, model a pair of waves travelling in opposite directions. The first wave travels at the bulk gas velocity plus the speed of sound, while the second travels at the bulk gas velocity minus the speed of sound. For the first case study, again a straight pipe of infinite length is envisioned, where the gas initially has the mean pressure, density and velocity as defined in Table 16, with a single pressure wave superimposed on the mean pressure. The speed of sound, frequency, wavelength, Courant number, and spatial discretization are the same as in the Linear Convection case study. The amplitude of the pressure wave has been chosen as 200 Pa (in correspondence with the assumptions in the linearization process). The simulation time is the same as in

the Linear Convection case study, though the distance travelled by the waves is different due to the non-zero bulk gas velocity.

Parameter	Value
Speed of Sound	346 m/s
Mean Pressure	1 bar
Mean Density	1.1692 kg/m^3
Mean Velocity	100 m/s
Amplitude	200 Pa
Frequency	400 Hz
Wave length	.865 m
Distance travelled	6.47 m, -3.57 m
Courant (CFL) number	.8
Spatial discretization	.0346 m
Volumes per Wavelength	25

Table 16: Linear Euler Equations Case Study Parameters

As discussed in Chapter 2, the linear Euler equations have a simple analytic solution for a defined initial spatial profile, as shown in (6.5). Since the wave speed is constant for the simulation, the solution at any time, t , is simply the summation of half of the initial profile shifted spatially by the product of the two wave speeds and the time t .

$$P(x,t) = \frac{P_0}{2}\left(x-(u+c)t\right) + \frac{P_0}{2}\left(x-(u-c)t\right) \tag{6.5}$$

Utilizing the parameters and the known solution from above, the benchmark for the linear Euler equation simulations is the analytic solution shown in Figure 41, for the initial and final simulation times.

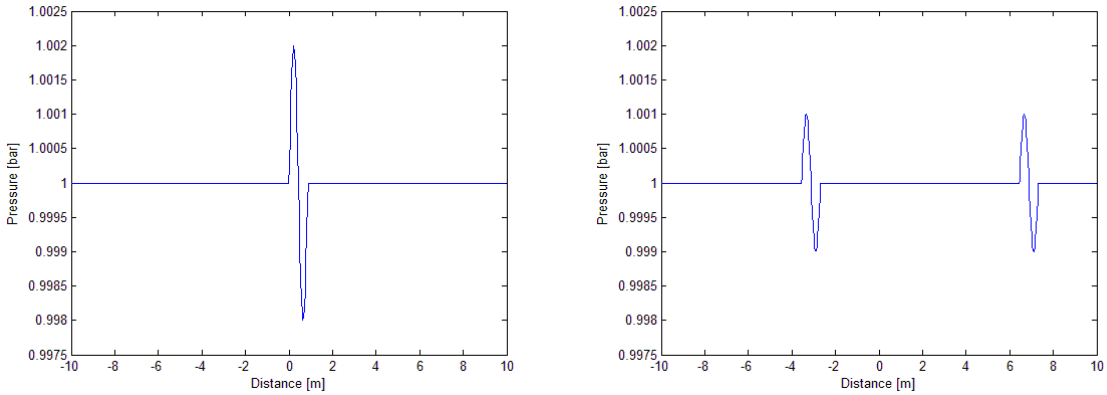

Figure 41: Linear Euler Equations Case Study Analytic Solution; Left: Initial Time; Right: Final Time

Again, results are presented first for the numerical methods of the first order upwind method and the Lax-Wendroff method. These results are presented in Figure 42 and Figure 43 where the methods' respective intended time stepping algorithms are used.

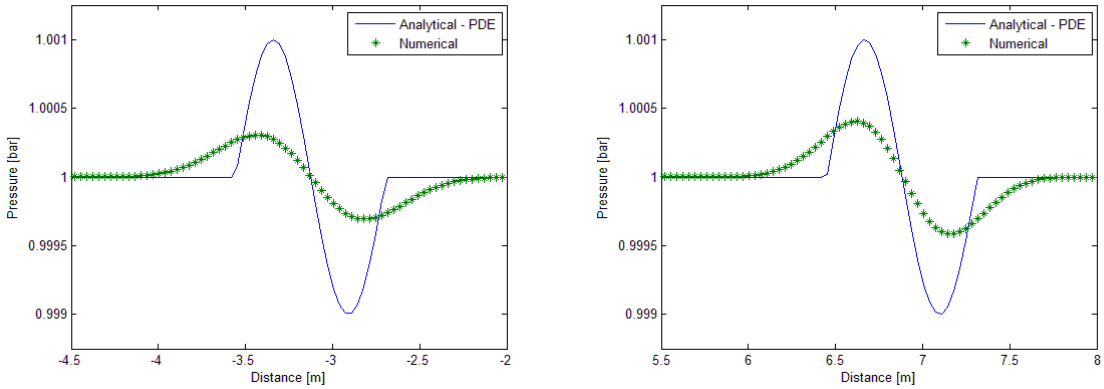

Figure 42: Linear Euler Equations Numeric Solution with First Order Upwind with Flux Vector Splitting; Left: Leftward Travelling Wave; Right: Rightward Travelling Wave

As described in Appendix 8.5.2, the first order upwind method for the linear Euler equations requires Flux Vector Splitting to fully distinguish between the leftward and rightward travelling fluxes. Figure 42 shows the results for this method. It can be seen that, like the results for the Linear Convection equation, the first order upwind method results in significant smearing and dissipation.

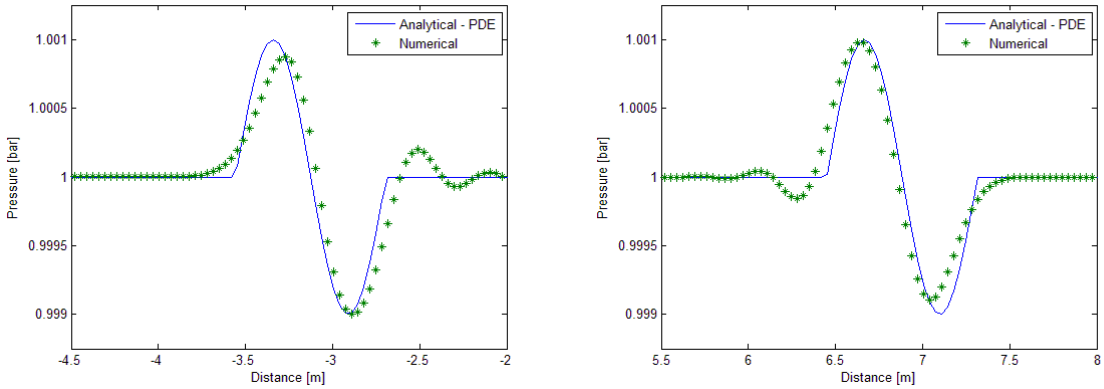

Figure 43: Linear Euler Equations Numeric Solution with Lax-Wendroff Method; Left: Leftward Travelling Wave; Right: Rightward Travelling Wave

The results for the linear Euler equations with the Lax-Wendroff method are shown in Figure 43. Again similar to the Linear Convection equation, these results show the presence of dispersion and spurious oscillations.

If we again replace the time stepping algorithms designed for the first order upwind and Lax-Wendroff methods with that of a 4th Order Runge-Kutta [132], the deficiencies are again magnified. Figure 44 shows that for the first order upwind method, the dissipation and smearing are more significant than in Figure 42. Furthermore, the spurious oscillations are magnified in Figure 45 in comparison to Figure 43.

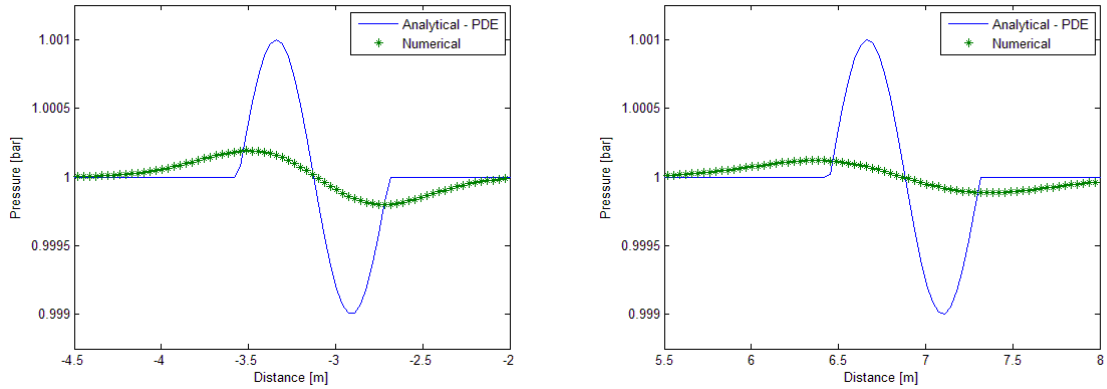

Figure 44: Linear Euler Equations; First Order Upwind, Flux Vector Splitting with 4th Order Runge-Kutta; Left: Leftward Travelling Wave; Right: Rightward Travelling Wave

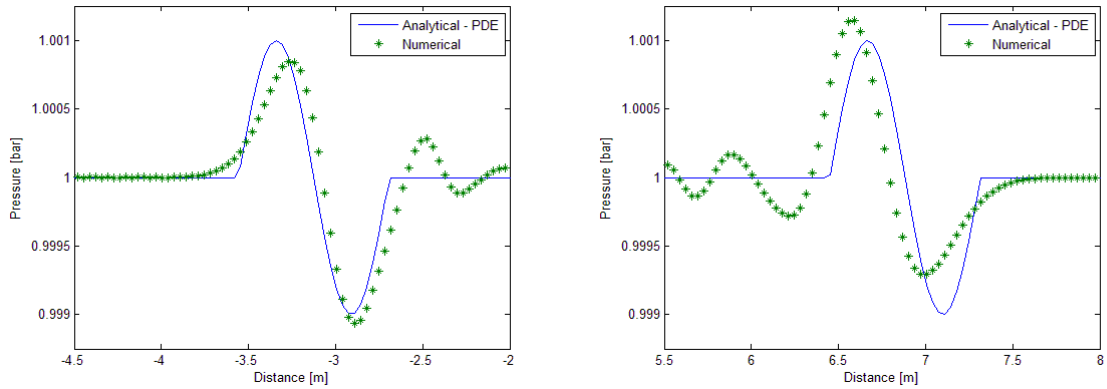

Figure 45: Linear Euler Equations with Lax-Wendroff Method with 4th Order Runge-Kutta; Left: Leftward Travelling Wave; Right: Rightward Travelling Wave

The Courant number study is repeated in Figure 46 and Figure 47 for the linear Euler equations with the two numerical methods. The spatial discretization is fixed, but the

time step is varied to see the effect of varying the Courant number on the accuracy of the numerical simulation. Again we find that for the upwind and Lax-Wendroff methods, as the time step is decreased, the accuracy of the simulation decreases. In the case of the upwind method, Figure 46 shows that the dissipation increases as the time step is decreased. Figure 47 shows that as the time step is decreased, the magnitude of the numerical oscillations increases for the Lax-Wendroff method.

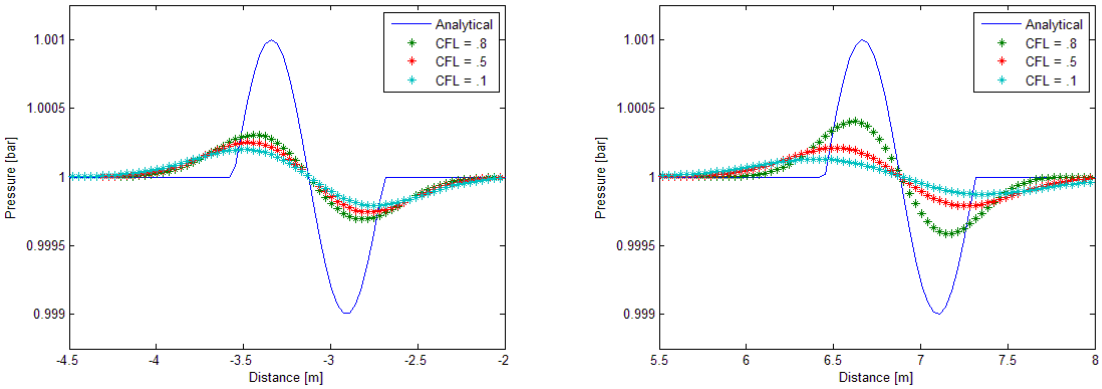

Figure 46: Linear Euler Equations; First Order Upwind, Flux Vector Splitting with Varying CFL; Left: Leftward Travelling Wave; Right: Rightward Travelling Wave

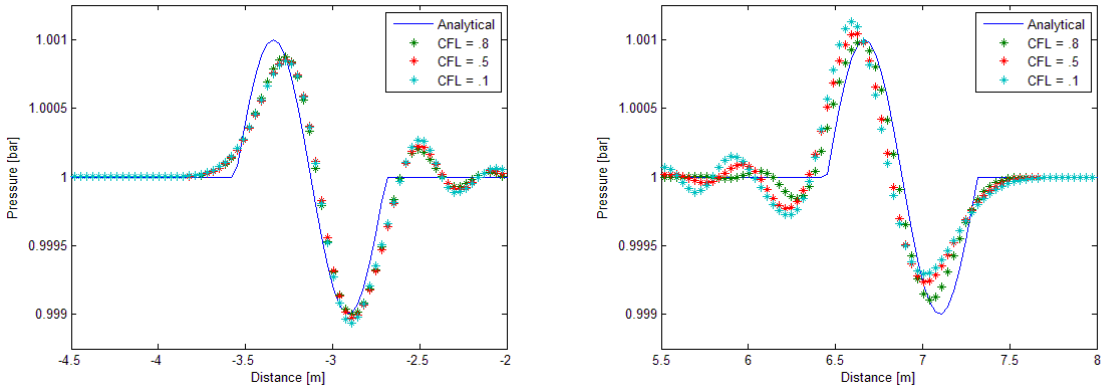

Figure 47: Linear Euler Equations with Lax-Wendroff Method with Varying CFL; Left: Leftward Travelling Wave; Right: Rightward Travelling Wave

Figure 48 - Figure 51 show the results of the proposed model order reduction process as applied to the linear Euler equations. Figure 48 shows the results for the leftward and rightward travelling wave for the constant basis function. As with the Linear Convection equation, the constant basis function contains smearing and dissipation. However, unlike the Linear Convection equation, the constant basis function performs better than the first order upwind method with the higher time stepping algorithm.

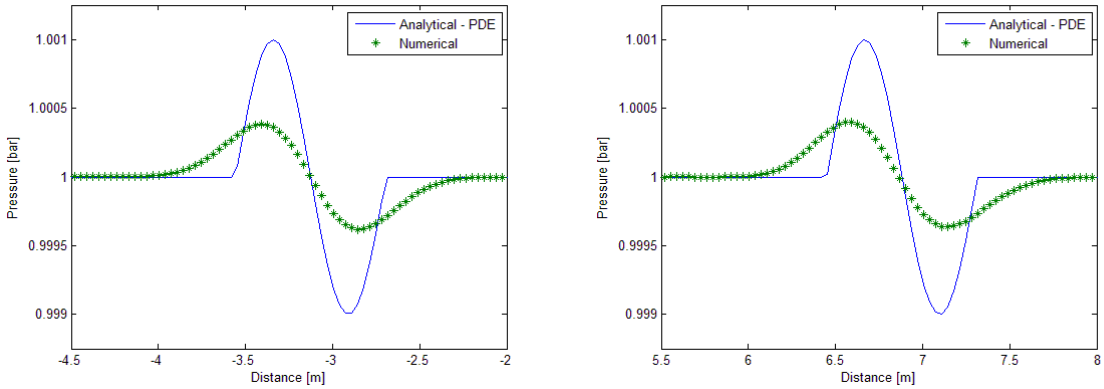

Figure 48: Linear Euler Equations Case Study Numeric Solution with Constant Basis Function; Left: Leftward Travelling Wave; Right: Rightward Travelling Wave

Figure 49 shows the results for the linear basis function. Again we find the presence of some dispersion and spurious oscillations, but these deficiencies are less prevalent then with the Lax-Wendroff method with the higher order time stepping algorithm.

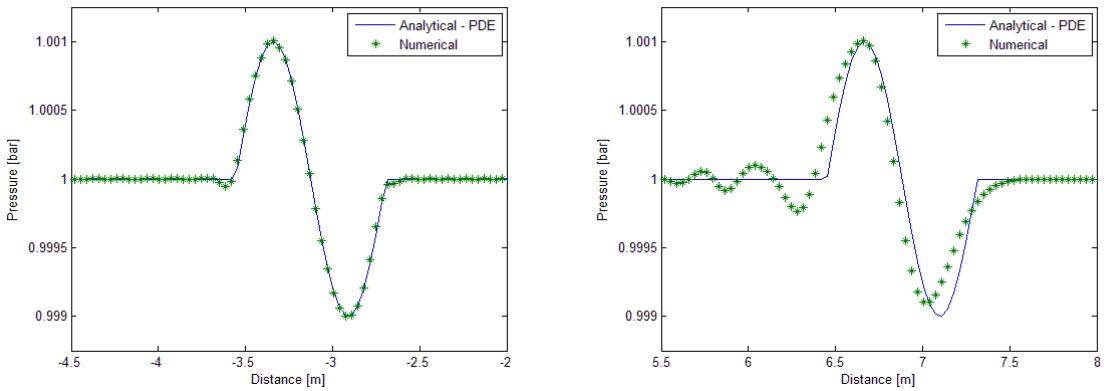

Figure 49: Linear Euler Equations Case Study Numeric Solution with Linear Basis Function; Left: Leftward Travelling Wave; Right: Rightward Travelling Wave

The results shown in Figure 50 and Figure 51 with the quadratic and cubic basis functions again show the benefits of the model order reduction process and the importance of selecting a proper basis function. The results show a significant improvement over the constant and linear methods, as well as over the first order upwind and second order Lax-Wendroff methods. The numerical solution in these figures tracks the analytic solution with only a hint of dissipation and dispersion.

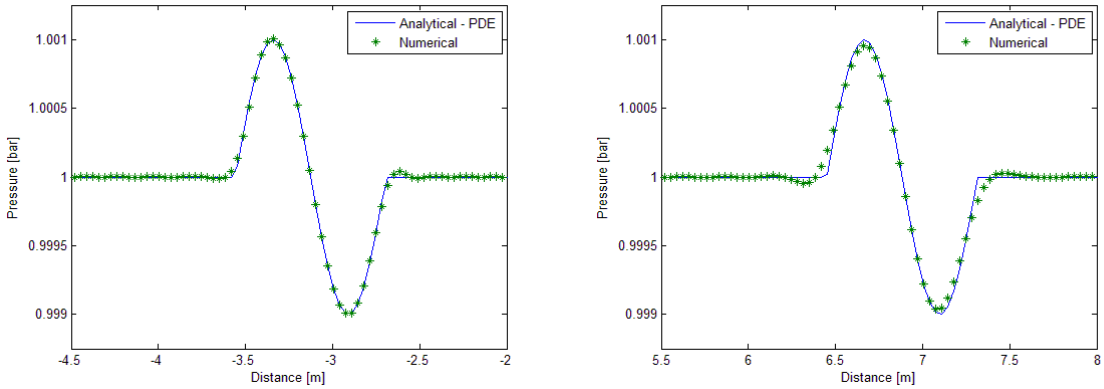

Figure 50: Linear Euler Equations Case Study Numeric Solution with Quadratic Basis Function; Left: Leftward Travelling Wave; Right: Rightward Travelling Wave

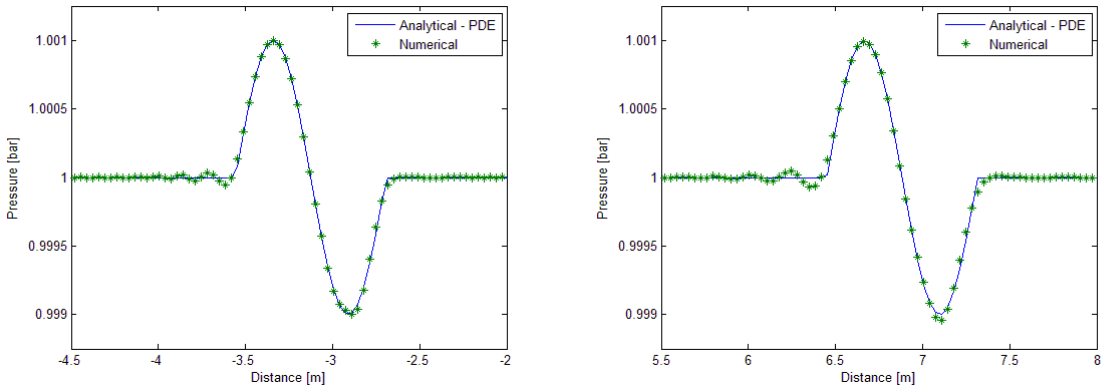

Figure 51: Linear Euler Equations Case Study Numeric Solution with Cubic Basis Function; Left: Leftward Travelling Wave; Right: Rightward Travelling Wave

Figure 52 again shows that the model order reduction process is insensitive to the time step, and thus the Courant number for a fixed spatial discretization.

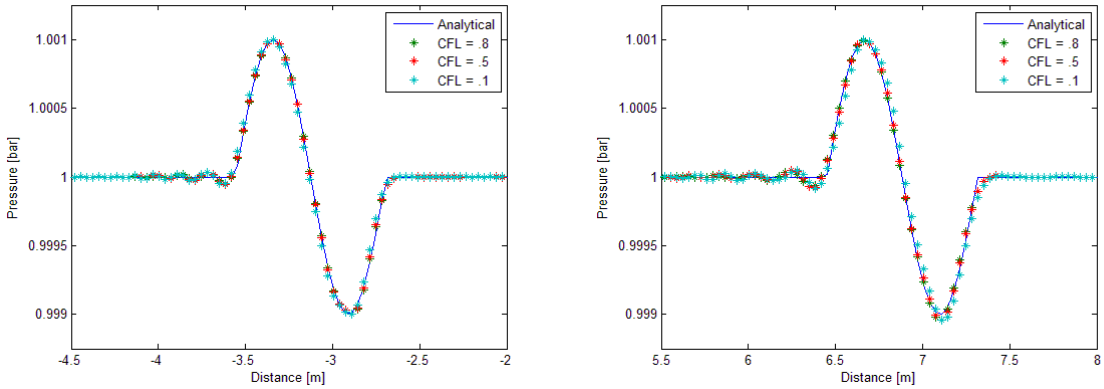

Figure 52: Linear Euler Equations Numeric Solution with Cubic Basis Function with Varying CFL; Left: Leftward Travelling Wave; Right: Rightward Travelling Wave

The second case study detailing the effect of distance travelled by the wave and the spatial discretization is repeated here for the linear Euler equations. The details of the case study are shown in Table 17.

Parameter	Value
Speed of Sound	346 m/s
Mean Pressure	1 bar
Mean Density	1.1692 kg/m^3
Mean Velocity	100 m/s
Amplitude	200 Pa
Frequency	400 Hz
Wave length	.865 m
Distance travelled	65 m, -36 m
Courant (CFL) number	.8
Spatial discretization	[.0346, .0432 .0721 .0692] m
Volumes per Wavelength	[25, 20, 15, 12.5]

Table 17: Linear Euler Equations Case Study II Parameters

The results of the study are shown in the following figures, where again the Root Mean Square of the percent error, as defined in (6.4), is plotted as a function of the distance travelled by the wave and the spatial discretization.

Figure 53 shows the results with the first order upwind and the Lax-Wendroff methods. The results are similar to those seen in the Linear Convection equation, where the Lax-Wendroff method out-performs the first order upwind method.

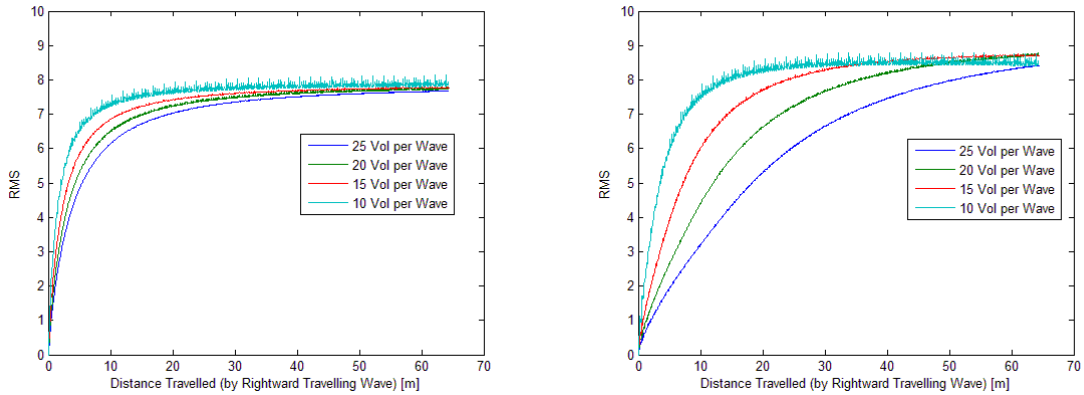

Figure 53: Linear Euler Equations Case Study II: RMS Percent Error vs. Distance Travelled; Left: First Order Upwind Method; Right: Lax-Wendroff Method

Figure 54 and Figure 55 show the results for with the four basis functions. Again, we see that the constant and linear basis function methods perform similar to that of the first order upwind and Lax-Wendroff methods. The quadratic and cubic methods, however, show a much slower accumulation in error as the wave travels, particularly for the smaller spatial discretizations.

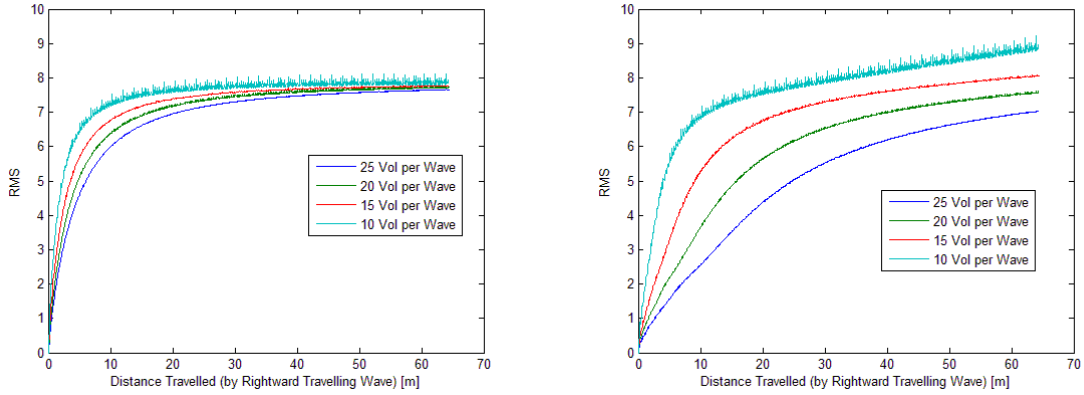

Figure 54: Linear Euler Equations Case Study II: RMS Percent Error vs. Distance Travelled; Left: Constant Basis Function; Right: Linear Basis Function

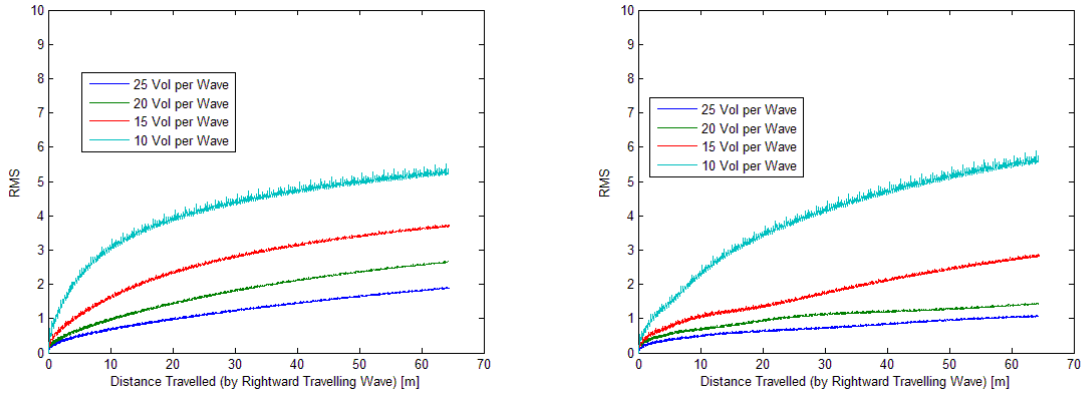

Figure 55: Linear Euler Equations Case Study II: RMS Percent Error vs. Distance Travelled; Left: Quadratic Basis Function; Right: Cubic Basis Function

6.2.3 Euler Equations

As a final validation of the model order reduction technique, the full set of Euler equations are evaluated on a simplified engine platform. A schematic of the engine is portrayed in Figure 56, where it can be seen that the engine's intake and exhaust system's geometry have been simplified to a straight pipe of constant area. The valves have been modeled in a similar fashion as described in Chapter 4, albeit with fixed cam timing.

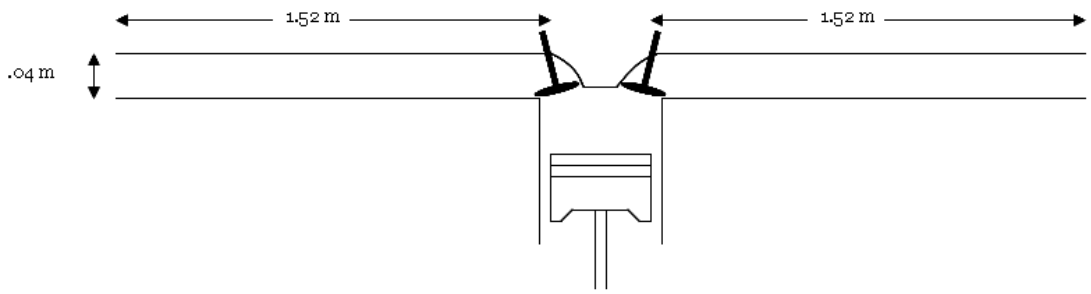

Figure 56: Single Cylinder Engine Schematic

The engine's geometrical parameters are outlined in Table 18, where it can be seen that the intake and exhaust systems have been modeled identically. Furthermore, for simplicity and ease of validation, the only losses modeled in the system are those associated with flow losses through the intake and exhaust valves. The intake and exhaust pipes, as well as the cylinder, have been assumed to be frictionless and adiabatic. Being that the focus of the case study is on the gas dynamics, fuel, and thus the combustion process, has been neglected.

Parameter	Value
Intake, exhaust pipe length	1.52 m
Intake, exhaust pipe diameter	.04 m
Cylinder bore	.088 m
Cylinder stroke	.098 m

Table 18: Single Cylinder Engine Model Parameters

Even with the broad assumptions and approximations described above, the single cylinder engine model comprises a complex physical system. The gas exchange process between the ambient environment, intake, cylinder and exhaust systems in reality is a three-dimensional phenomenon. However, due to the simplified geometry, an assumption of one-dimensional flow in the intake and exhaust systems is reasonable, with some sacrifices in accuracy at the pipe boundaries. It is reasonable, then for the intake and exhaust systems to be modeled through the one-dimensional Euler equations described in Section 2.2.2. As discussed previously, this set of equations is nonlinear and thus for the present case study does not have known analytical solution. The model order reduction technique can then only be evaluated against a high fidelity numerical solution.

The commercial software GT Power [32] has been selected as a means of evaluating the model order reduction technique. A representation of the engine described above as developed in GT Power is shown in Figure 57. The engine's intake and exhaust system have been discretized into a user-defined number of pipe volumes, while the valves and cylinder are modeled through standard GT Power components [32].

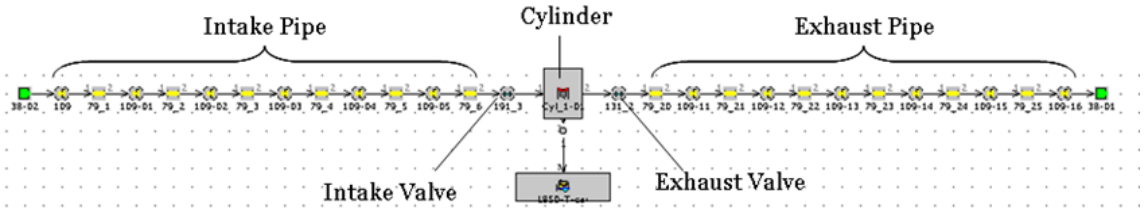

Figure 57: GT Power Representation of Single Cylinder Engine

In order to establish a high fidelity numerical benchmark, the GT Power model's intake and exhaust systems have been discretized into 80 pipe volumes, respectively. The model is then simulated over an engine speed sweep covering the range of 1000 – 6000 RPM in increments of 250 RPM. As discussed in Chapter 4, a pertinent metric for the gas exchange process of an internal combustion engine is the engine's volumetric efficiency (VE). This parameter has been selected for evaluation of the model order reduction technique, with the benchmark results shown in Figure 58.

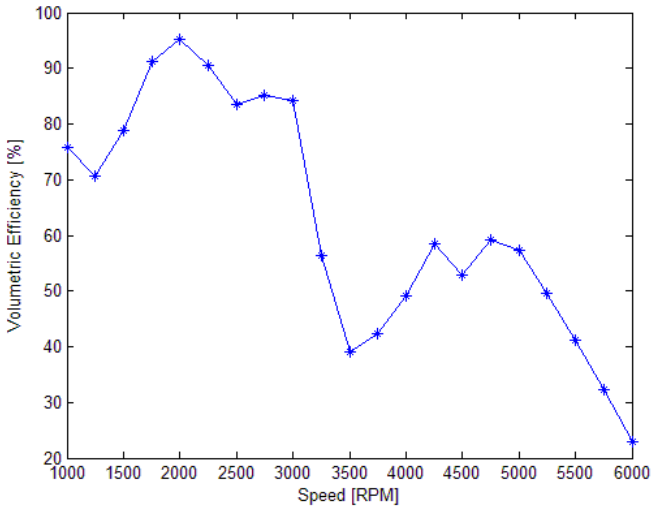

Figure 58: Volumetric Efficiency vs. Engine Speed: GT Power Simulation with 80 Volumes

As discussed previously, a pertinent objective of this case study is the ability to describe the engine's gas exchange process through a low order set of ordinary differential equations. The order of the system is directly proportional to the number of pipe volumes comprised in the intake and exhaust systems. As a means of comparison, a traditional zero-dimensional, crank angle resolved representation of the single cylinder engine (following the description in Section 4.2.1) was simulated over the speed sweep, with the results presented in Figure 59. The results are compared to the benchmark GT Power simulation with 80 volumes, where the error in volumetric efficiency is defined in (6.6).

$$Error_{VE} = VE_{simulation} - VE_{GTPower,80Volumes} \tag{6.6}$$

The poor accuracy in volumetric efficiency prediction exemplifies the zero-dimensional representation's inability to model the gas dynamic effects.

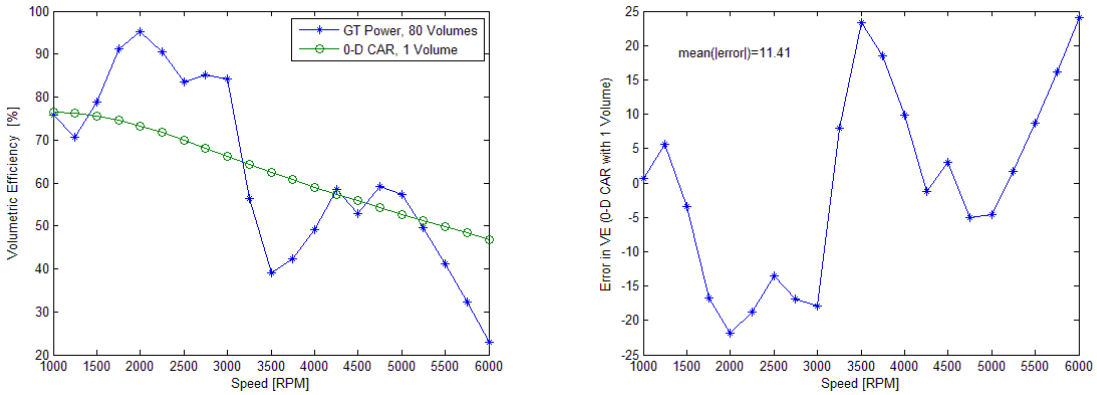

Figure 59: Zero-Dimensional Crank Angle Resolved with One Volume; Left: Volumetric Efficiency vs. Engine Speed; Right: Error in Volumetric Efficiency

With these results in mind, a case study of six volumes (per intake and exhaust system) has been selected to evaluate the model order reduction technique's ability to model the underlying physics through a low order set of ordinary differential equations. For comparison purposes, the GT Power model was modified to include six pipe volumes per the intake and exhaust system, with the results shown in Figure 60. These results represent conventional numerical methods' ability to model the gas exchange portion of an internal combustion engine with a low number of volumes. It can be seen that a conventional numerical method with six volumes captures the general trend of the volumetric efficiency, with accuracy decreasing for higher engine speeds.

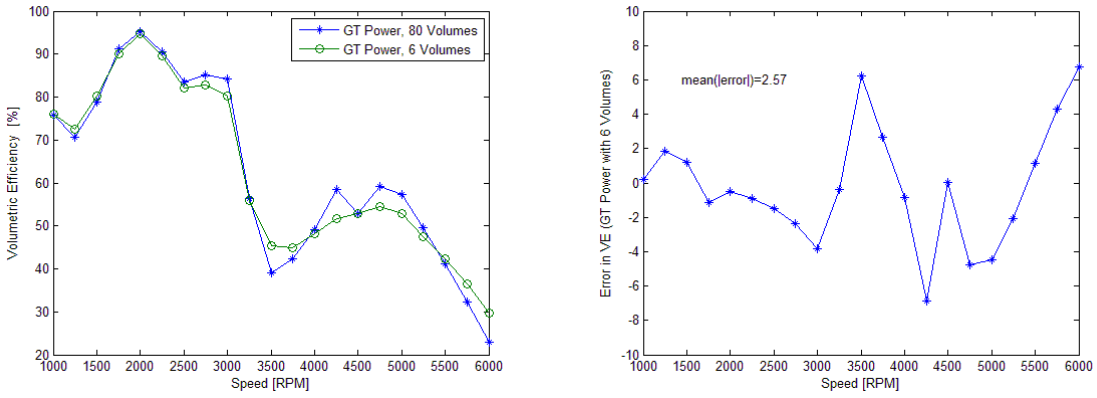

Figure 60: GT Power Simulation with Six Volumes; Left: Volumetric Efficiency vs. Engine Speed; Right: Error in Volumetric Efficiency

The same set of simulations is repeated for the model order reduction technique with the constant basis function with six volumes. The results are compared to the GT Power simulations with 6 and 80 volumes in Figure 61. The results indicate that the model order reduction technique with a constant basis function and six volumes achieves accuracy comparable to that of the computational fluid dynamics model with six volumes. In comparison to the GT Power simulation with 80 volumes, it can be seen that the low order method is capable of describing the gas exchange process well at low engine speeds, but as engine speed is increased some errors are introduced in the prediction of volumetric efficiency.

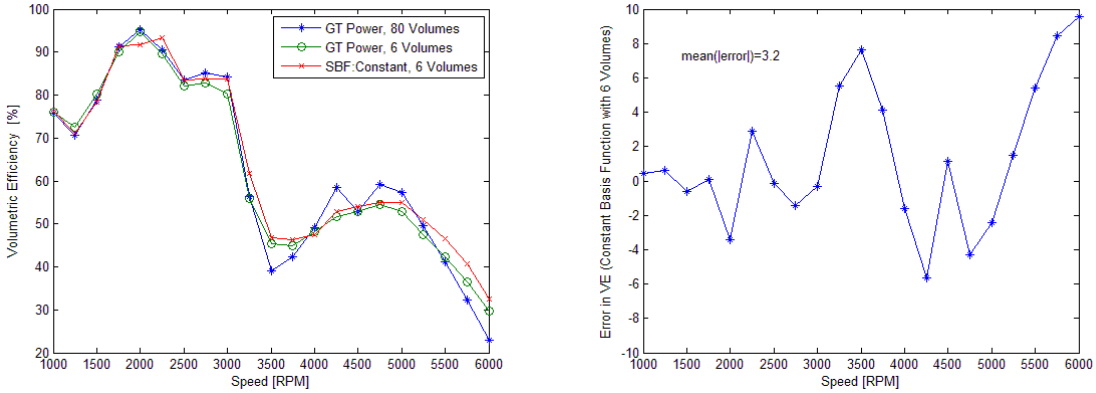

Figure 61: Constant Basis Function Simulation with Six Volumes; Left: Volumetric Efficiency vs. Engine Speed; Right: Error in Volumetric Efficiency

The crank angle domain plots shown in Figure 62 - Figure 65 exemplify how well the constant basis function method matches the results of the GT Power simulation with six volumes. Figure 62 and Figure 63 show the intake and exhaust port pressures and valve flows at 1000 RPM. It can be seen that the model order reduction technique with a constant basis function is capable of describing the gas dynamics within an ordinary differential equation structure to a high degree of accuracy with respect to the computational fluid dynamics results. Figure 64 and Figure 65 show that the results also match well at 6000 RPM.

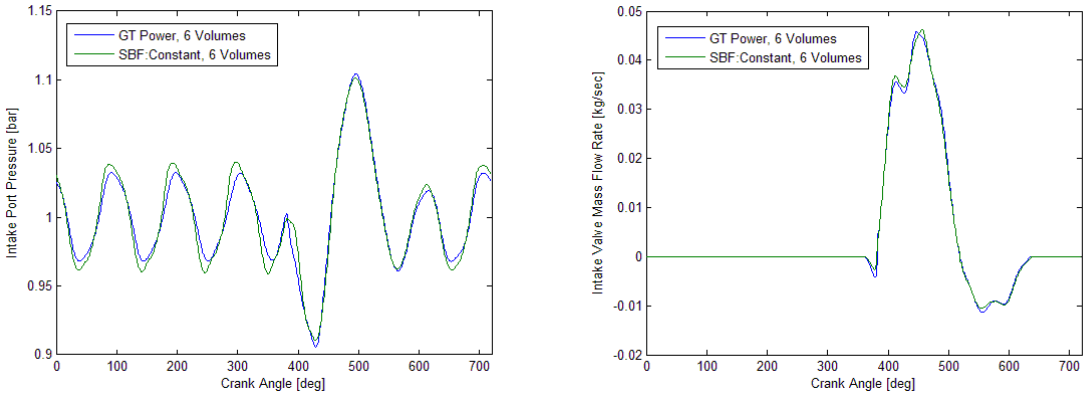

Figure 62: Crank Angle Domain Simulation Results with Six Volumes at 1000 RPM; Left: Intake Port Pressure; Right: Intake Valve Mass Flow Rate

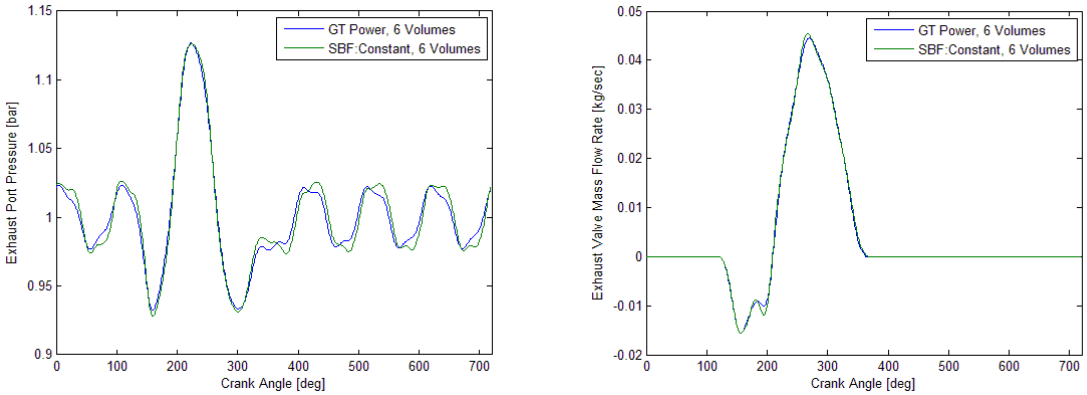

Figure 63: Crank Angle Domain Simulation Results with Six Volumes at 1000 RPM; Left: Exhaust Port Pressure; Right: Exhaust Valve Mass Flow Rate

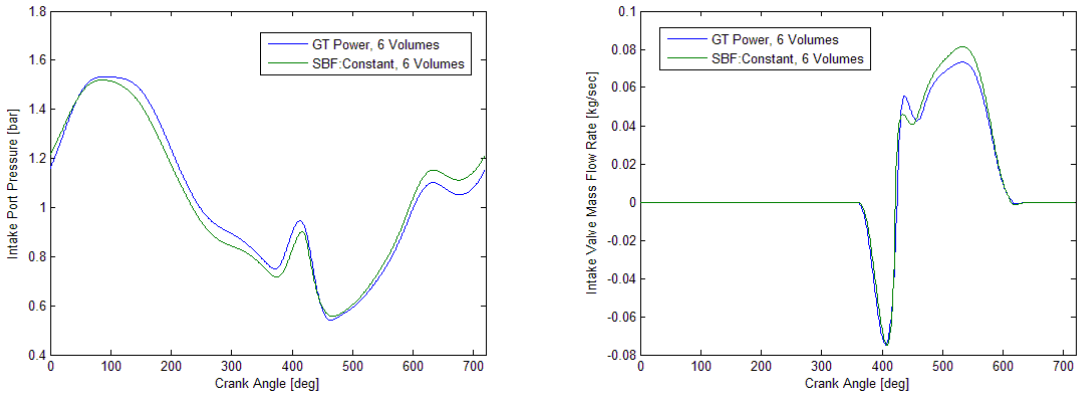

Figure 64: Crank Angle Domain Simulation Results with Six Volumes at 6000 RPM; Left: Intake Port Pressure; Right: Intake Valve Mass Flow Rate

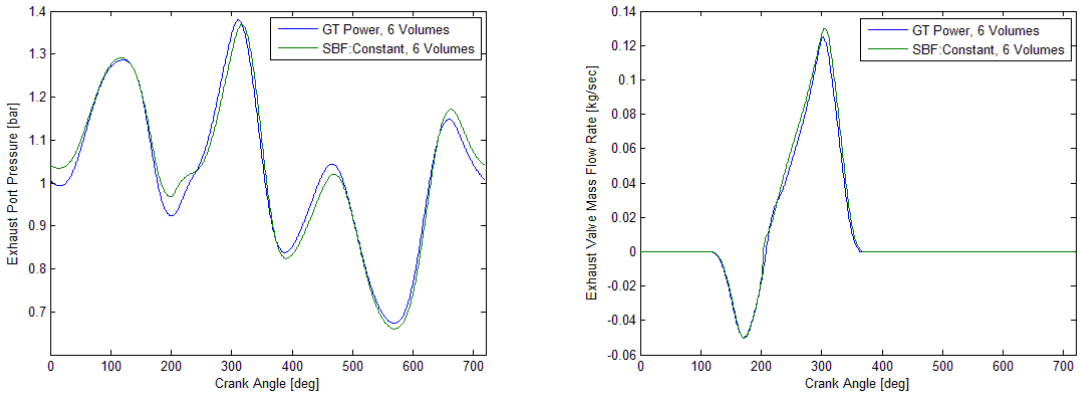

Figure 65: Crank Angle Domain Simulation Results with Six Volumes at 6000 RPM; Left: Exhaust Port Pressure; Right: Exhaust Valve Mass Flow Rate

The results above show that the model order reduction technique with a constant basis function can achieve accuracy comparable to that of a commercial computational fluid dynamics software. Furthermore, the model order reduction technique is capable of

achieving such accuracy through an ordinary differential equation structure and within a standard dynamic systems simulation package.

The effect of employing a more sophisticated basis function is explored in Figure 66. These simulation results again utilize six volumes for the intake and exhaust systems, but the constant basis function has been replaced by the quadratic basis function. The results show that quadratic basis function is capable of describing the volumetric efficiency accurately across the speed range. In particular, it can be seen that the quadratic basis function achieves a higher degree of accuracy at high engine speeds than the computational fluid dynamics algorithm with the same number of volumes.

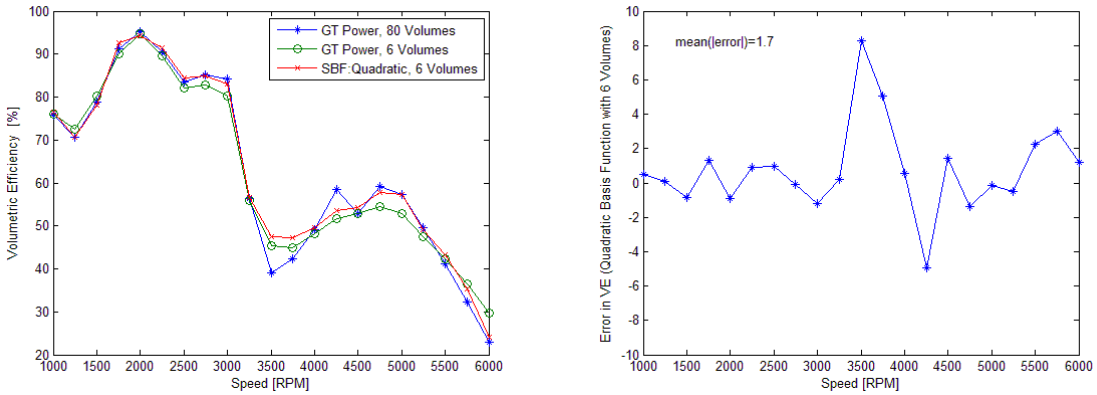

Figure 66: Quadratic Basis Function Simulation with Six Volumes; Left: Volumetric Efficiency vs. Engine Speed; Right: Error in Volumetric Efficiency

The results of the single cylinder engine case study are summarized in Table 19 employing the metric of the mean absolute error in volumetric efficiency as defined in (6.7).

$$MeanAbsoluteError_{VE} = mean\left(\left|VE_x - VE_{GTPower,80Volumes}\right|\right) \tag{6.7}$$

The results show that with respect to the 80 volume GT Power simulation results, the model order reduction technique with a constant basis function and six volumes achieves a mean absolute error in volumetric efficiency on the order of 3 percent (a value slightly larger than that achieved by the computational fluid dynamics simulation with the same number of volumes). The model order reduction technique with the quadratic basis function, on the other hand, achieves a mean absolute error in volumetric efficiency on the order of 1.7 %. The commercial computational fluid dynamics software would require nine volumes to achieve this level of accuracy.

Simulation	Number of Volumes	Mean Absolute Error in VE
GT Power	9	1.68
SBF: Quadratic	6	1.70
GT Power	6	2.57
SBF: Constant	6	3.20
0-D CAR	1	11.41

Table 19: Mean Absolute Error in Volumetric Efficiency Prediction with Respect to 80 Volume GT Power Simulation

Table 20 displays a comparison of the number of states and the corresponding simulation time for the model order reduction technique. The results are compared against the 0-D CAR results, since these models have been coded in the same software package. The results indicate that the significant increase in accuracy and fidelity associated with the model order reduction technique is offset by only a small increase in computation time.

Simulation	Number of Volumes per intake \ exhaust system	Number of States	Computation Time (normalized to 0-D CAR)
0-D CAR	1	13	1
SBF: Constant	6	43	1.6
SBF: Quadratic	6	43	1.6

Table 20: Simulation Time Comparison

6.3 Conclusions

The model order reduction procedure has been evaluated with respect to its ability to employ a low order, ordinary differential equation structure to model distributed parameter systems. The evaluation has been performed through case studies carefully selected to mimic engine intake and exhaust systems. The Linear Convection and linear Euler equations have been evaluated on traveling wave scenarios where the wave speeds and amplitudes have been chosen to resemble engine intake and exhaust conditions. The four basis functions were evaluated within the model order reduction technique against these two sets of equations by comparing the results against analytic and standard numerical methods solutions. The results show that the piecewise constant and linear methods achieve results comparable to the standard numerical methods. The piecewise

quadratic and cubic basis functions, however, match the analytic simulation results to high degree of accuracy and outperform the standard numerical methods. Furthermore, it has been shown that model order reduction technique (unlike the numerical methods) is insensitive to changes in time step, assuming that the Courant condition is satisfied. This quality is advantageous for engine simulations were engine speed varies over a wide range.

As a final evaluation, the piecewise constant and piecewise quadratic basis functions were chosen for evaluation against the full set of Euler equations. A case study of a single cylinder engine model was developed, where the results are compared against a high fidelity commercial computational fluid dynamics software package. The results indicate that the piecewise constant basis function achieves accuracy comparable to the computational fluid dynamics software, with respect to its ability to model crank angle resolved pressures and mass flow rates, as well as the cycle average quantity of volumetric efficiency. Furthermore, the piecewise quadratic method has been shown to yield an improvement over computational fluid dynamics software in that a fewer number of volumes is required to achieve a defined level of accuracy in volumetric efficiency prediction.

CHAPTER 7

CONCLUSIONS AND RECOMMENDATIONS

7.1 Conclusions

Methodologies for the development of computationally efficient, crank angle resolved system dynamics models of internal combustion engine systems have been evaluated. Specifically, focusing on the engine intake and exhaust gas exchange process, two novel parallel paths to achieve similar ends have been developed.

The first path improves upon the traditional zero-dimensional filling and emptying model to incorporate the inherently distributed phenomena of wave dynamic and charge heating effects within a 0-D context. The method involves the identification and calibration of a set of empirical parameters and has been shown to be applicable across the entire engine operating map. Simulation and experimental results validate that the improved 0-D CAR model with Wave Dynamic Compensation is capable of predicting both cycle-resolved and crank angle resolved states to a high degree of accuracy, while maintaining a computationally efficient architecture.

A second path has been devised to achieve similar ends without the heavy reliance upon empirical parameters. This approach has been developed beginning from the fundamental equations governing compressible fluid systems and applies an innovative model order reduction method to project the governing partial differential equations onto ordinary differential equations. The approach has been evaluated on linear equations approximating the underlying physics and, with the proper choice in basis function, has been shown to yield results better than some computational fluid dynamics algorithms. The methodology has been validated through a case study of a single cylinder engine model, where the results have been shown to be an improvement over the industry standard commercial one-dimensional simulation package.

7.2 Recommendations and Future Work

The two paths for system dynamic modeling of crank angle resolved engine models have great potential for aiding controls and performance engineers in developing, optimizing and evaluating control systems.

The first path, based upon an empirical approach, has great potential for high fidelity transient simulation applications. The simple, compact architecture can provide extremely efficient simulations with crank angle resolved accuracy. This architecture can permit the inclusion of a high fidelity engine model within a full vehicle model to analyze engine-drivetrain-vehicle interactions and can help evaluate the “drivability” aspect of the control system. Furthermore, as computer processor and hardware

technology continues to improve, this level of model may serve in Software in the Loop (SIL) and Hardware in the Loop (HIL) applications to debug and properly evaluate control algorithms.

Applications for the second path overlap with the first, with the addition of a number of analytical benefits. The model order reduction path provides a complete model of the engine's distributed intake and exhaust systems as a set of ordinary differential equations. Such an equation set can be used to help identify the sensitivity of geometrical parameters, as well as for developing lower fidelity, input-output relationships. Additionally, the ODE structure can be employed for the creation of estimators in place of physical sensors. Furthermore, future developments in this methodology will most certainly be obtained through the evaluation of different classes of basis functions.

APPENDIX: MATHEMATICAL DERIVATIONS

8.1 Derivation of Approximations to 1-D Equations

8.1.1 Linear Euler Equations

In the following sections, the one-dimensional Euler equations are reduced to a linear form under an assumption of small perturbations. A distinction is presented between the linear Euler equations with and without bulk flow. The first section derives the equations under the assumption that the gas has a mean flow of velocity, while the second section assumes that the bulk gas velocity is zero, leading to the well known Acoustic Equations.

8.1.1.1 With Bulk Flow

We begin with the constant-area, one-dimensional, differential form of the conservations of mass and momentum and assume an isentropic process in liu of the energy equation:

$$\frac{\partial \rho}{\partial t} + \frac{\partial (\rho u)}{\partial x} = 0 \tag{8.1}$$

$$\frac{\partial (\rho u)}{\partial t} + \frac{\partial (\rho u^2)}{\partial x} + \frac{\partial P}{\partial x} = 0 \tag{8.2}$$

$$P = \rho c^2 \tag{8.3}$$

The first and second derivatives within the momentum equation can be expanded as follows:

$$\rho\frac{\partial u}{\partial t}+u\frac{\partial \rho}{\partial t}+u\frac{\partial(\rho u)}{\partial x}+\rho u\frac{\partial u}{\partial x}+\frac{\partial P}{\partial x}=0 \tag{8.4}$$

The terms in (8.4) can be collected as follows:

$$\rho\left\{\frac{\partial u}{\partial t}+u\frac{\partial u}{\partial x}\right\}+u\left\{\frac{\partial \rho}{\partial t}+\frac{\partial(\rho u)}{\partial x}\right\}+\frac{\partial P}{\partial x}=0 \tag{8.5}$$

The conservation of mass can be applied to (8.5) to yield the reduced form:

$$\rho\left\{\frac{\partial u}{\partial t}+u\frac{\partial u}{\partial x}\right\}+\frac{\partial P}{\partial x}=0 \tag{8.6}$$

The conservation equations shown in (8.7) and (8.8) are ready for the linearization process.

$$\frac{\partial \rho}{\partial t}+\frac{\partial(\rho u)}{\partial x}=0 \tag{8.7}$$

$$\frac{\partial u}{\partial t}+u\frac{\partial u}{\partial x}+\frac{1}{\rho}\frac{\partial P}{\partial x}=0 \tag{8.8}$$

We now begin the linearization process by defining that the states are comprised of a summation of a mean component (denoted with the subscript 0) and a fluctuating component. The mean component is assumed to be independent of time and space.

$$P(x,t) = P_0 + \hat{P}(x,t) \tag{8.9}$$

$$\rho(x,t) = \rho_0 + \hat{\rho}(x,t) \tag{8.10}$$

$$u(x,t) = u_0 + \hat{u}(x,t) \tag{8.11}$$

We assume that the fluctuating components are much less than their mean value:

$$\frac{\hat{\rho}}{\rho_0} << 1, \frac{\hat{P}}{\hat{P}_0} << 1, \frac{u}{u_0} << 1 \tag{8.12}$$

Applying equations (8.9) - (8.11) to the conservation of mass in (8.7) yields:

$$\frac{\partial(\rho_0 + \hat{\rho})}{\partial t} + \frac{\partial\left((\rho_0 + \hat{\rho})(u_0 + \hat{u})\right)}{\partial x} = \frac{\partial(\rho_0 + \hat{\rho})}{\partial t} + \frac{\partial(\rho_0 u_0 + \hat{\rho}u_0 + \rho_0\hat{u} + \hat{\rho}\hat{u})}{\partial x} = 0 \tag{8.13}$$

This equation can be reduced through the assumption that the mean values are independent of space and time and by assuming the product of two small quantities is negligible:

$$\frac{\partial\hat{\rho}}{\partial t} + u_0\frac{\partial\hat{\rho}}{\partial x} + \rho_0\frac{\partial\hat{u}}{\partial x} = 0 \tag{8.14}$$

Applying equations (8.9) - (8.11) to the conservation of momentum in (8.8) yields:

$$\frac{\partial(u_0 + \hat{u})}{\partial t} + (u_0 + \hat{u})\frac{\partial(u_0 + \hat{u})}{\partial x} + \frac{1}{\rho_0 + \hat{\rho}}\frac{\partial(P_0 + \hat{P})}{\partial x} = 0 \tag{8.15}$$

Again, this can be reduced through the assumptions defined above:

$$\frac{\partial \hat{u}}{\partial t} + u_0 \frac{\partial \hat{u}}{\partial x} + \frac{1}{\rho_0 + \hat{\rho}} \frac{\partial \hat{P}}{\partial x} = 0 \tag{8.16}$$

Multiplying through by the denominator and applying the same logic as above yields:

$$\rho_0 \frac{\partial \hat{u}}{\partial t} + \rho_0 u_0 \frac{\partial \hat{u}}{\partial x} + \frac{\partial \hat{P}}{\partial x} = 0 \tag{8.17}$$

Equation (8.3) can be applied to (8.17); the resulting linear Euler equations (with bulk flow) are shown below. [Note: the notation for the fluctuating component has been dropped].

$$\frac{\partial \rho}{\partial t} + u_0 \frac{\partial \rho}{\partial x} + \rho_0 \frac{\partial u}{\partial x} = 0 \tag{8.18}$$

$$\frac{\partial u}{\partial t} + u_0 \frac{\partial u}{\partial x} + \frac{c^2}{\rho_0} \frac{\partial \rho}{\partial x} = 0 \tag{8.19}$$

8.1.1.2 Without Bulk Flow (Acoustic Equations)

The linear Euler equations can be further simplified under the assumption that there is no bulk fluid velocity $\left(u_0 = 0\right)$. Applying this assumption to (8.18) and (8.19) yields the equation set shown below:

$$\frac{\partial \rho}{\partial t} + \rho_0 \frac{\partial u}{\partial x} = 0 \tag{8.20}$$

$$\frac{\partial u}{\partial t} + \frac{1}{\rho_0} \frac{\partial P}{\partial x} = 0 \tag{8.21}$$

These equations can be combined for an alternative presentation as follows:

First, differentiate the conservation of mass with respect to time:

$$\frac{\partial^2 \rho}{\partial t^2} + \rho_0 \frac{\partial^2 u}{\partial x \partial t} = 0 \tag{8.22}$$

Next, differentiate the conservation of momentum with respect to distance:

$$\rho_0 \frac{\partial^2 u}{\partial t \partial x} + \frac{\partial^2 p}{\partial x^2} = 0 \tag{8.23}$$

Now combine these two equations:

$$\frac{\partial^2 \rho}{\partial t^2} = \frac{\partial^2 p}{\partial x^2} \tag{8.24}$$

Finally, applying the relation from (8.3) to (8.24) yields the well known wave equation:

$$\frac{\partial^2 P}{\partial x^2} = \frac{1}{c^2} \frac{\partial^2 P}{\partial t^2} \tag{8.25}$$

8.1.2 Linear Convection Equation

The derivation of the Linear Convection Equation is presented below, beginning from the Euler equations. Along the way, the Nonlinear Burger's Equation is derived as an intermediate step.

We begin with the constant-area, one-dimensional, differential form of the conservations of mass and momentum and assume an isentropic process in liu of the energy equation:

$$\frac{\partial \rho}{\partial t} + \frac{\partial (\rho u)}{\partial x} = 0 \tag{8.26}$$

$$\frac{\partial (\rho u)}{\partial t} + \frac{\partial (\rho u^2)}{\partial x} + \frac{\partial P}{\partial x} = 0 \tag{8.27}$$

$$P = \rho c^2 \tag{8.28}$$

Applying equation (8.28) to (8.27) yields:

$$\frac{\partial (\rho u)}{\partial t} + \frac{\partial (\rho u^2)}{\partial x} + c^2 \frac{\partial \rho}{\partial x} = 0 \tag{8.29}$$

The first and second derivatives within this equation can be expanded as follows:

$$\rho \frac{\partial u}{\partial t} + u \frac{\partial \rho}{\partial t} + u \frac{\partial (\rho u)}{\partial x} + \rho u \frac{\partial u}{\partial x} + c^2 \frac{\partial \rho}{\partial x} = 0 \tag{8.30}$$

The terms in (8.30) can be collected as follows:

$$\rho\left\{\frac{\partial u}{\partial t}+u\frac{\partial u}{\partial x}\right\}+u\left\{\frac{\partial \rho}{\partial t}+\frac{\partial\left(\rho u\right)}{\partial x}\right\}+c^2\frac{\partial \rho}{\partial x}=0 \tag{8.31}$$

The conservation of mass can be applied to (8.31) to yield the reduced form:

$$\rho\left\{\frac{\partial u}{\partial t}+u\frac{\partial u}{\partial x}\right\}+c^2\frac{\partial \rho}{\partial x}=0 \tag{8.32}$$

Under the assumption of constant density, (8.32) can be reduced to:

$$\frac{\partial u}{\partial t}+u\frac{\partial u}{\partial x}=0 \tag{8.33}$$

The second term in (8.33) can be re-written as:

$$u\frac{\partial u}{\partial x}=\frac{u}{2}\frac{\partial u}{\partial x}+\frac{u}{2}\frac{\partial u}{\partial x}=\frac{1}{2}\frac{\partial u^2}{\partial x} \tag{8.34}$$

Substituting (8.34) into (8.33) yields the *Nonlinear Inviscid Burger's Equation*:

$$\frac{\partial u}{\partial t}+\frac{1}{2}\frac{\partial u^2}{\partial x}=0 \tag{8.35}$$

We now begin the linearization process by defining that the state is comprised of a summation of a mean component (denoted with the subscript 0) and a fluctuating component. The mean component is assumed to be independent of time and space.

$$u\left(x,t\right)=u_0+\hat{u}\left(x,t\right) \tag{8.36}$$

We assume that the fluctuating component is much less than the mean value:

$$\frac{u}{u_0} << 1 \tag{8.37}$$

Applying (8.36) to (8.35) yields:

$$\frac{\partial\left(u_0+\hat{u}\right)}{\partial t}+\frac{1}{2}\frac{\partial\left(u_0+\hat{u}\right)^2}{\partial x}=\frac{\partial\left(u_0+\hat{u}\right)}{\partial t}+\frac{1}{2}\frac{\partial\left(u_0u_0+2u_0\hat{u}+\hat{u}\hat{u}\right)}{\partial x}=0 \tag{8.38}$$

This equation can be reduced through the assumption that the mean values are independent of space and time and by assuming the product of two small quantities is negligible:

$$\frac{\partial\hat{u}}{\partial t}+u_0\frac{\partial\hat{u}}{\partial x}=0 \tag{8.39}$$

This equation can be generalized to the *Linear Convection Equation* through setting the mean component equal to an arbitrary constant $\left(u_0=c\right)$. [Note: the notation for the fluctuating component has been dropped].

$$\frac{\partial u}{\partial t}+c\frac{\partial u}{\partial x}=0 \tag{8.40}$$

8.2 Zero-Dimensional Crank Angle Resolved Model Derivations

8.2.1 Temperature Dynamics

The zero-dimensional conservation of energy can be applied to a generic control volume to yield:

$$\frac{d\left(m \cdot e\right)}{dt} = \dot{Q} - \dot{W} + \dot{m}_{in} h_{in} - \dot{m}_{out} h_{out} \tag{8.41}$$

Expanding the left hand side of the equation via the chain rule and knowing that the heat energy entering the control volume is the difference between the energy from combustion and the energy lost due to heat transfer, as well as knowing that the work done by the change in volume is equal to the integral of the pressure times the change in volume yields:

$$e\frac{dm}{dt} + m\frac{du}{dt} = \dot{Q}_{com} - \dot{Q}_{ht} - P\frac{dV}{dt} + \dot{m}_{in} h_{in} - \dot{m}_{out} h_{out} \tag{8.42}$$

The gas can be assumed to be composed of three species: air, fuel and exhaust. Based upon this assumption, the internal energy of the gas can be defined as:

$$e = e_{air} X_{air} + e_{ex} X_{ex} + e_{fuel} X_{fuel} \tag{8.43}$$

Differentiating equation (8.43) with respect to time yields:

$$\frac{de}{dt} = X_{air}\frac{de_{air}}{dt} + e_{air}\frac{dX_{air}}{dt} + X_{ex}\frac{de_{ex}}{dt} + e_{ex}\frac{dX_{ex}}{dt} + X_{fuel}\frac{de_{fuel}}{dt} + e_{fuel}\frac{dX_{fuel}}{dt} \quad (8.44)$$

The internal energy of the respective three mixtures can be defined as:

$$\frac{de_{air}}{dt} = c_{v,air}\frac{dT}{dt} \quad (8.45)$$

$$\frac{de_{ex,cyl}}{dt} = c_{v,ex}\frac{dT}{dt} \quad (8.46)$$

$$\frac{de_{fuel,cyl}}{dt} = c_{v,fuel}\frac{dT}{dt} \quad (8.47)$$

Applying equations (8.45)-(8.47) to (8.44) yields:

$$\frac{de}{dt} = \frac{dT}{dt}\left\{X_{air}c_{v,air} + X_{ex}c_{v,ex} + X_{fuel}c_{v,fuel}\right\} + e_{air}\frac{dX_{air}}{dt} + e_{ex}\frac{dX_{ex}}{dt} + e_{fuel}\frac{dX_{fuel}}{dt} \quad (8.48)$$

The definition of the specific heat at constant volume within the cylinder is known to be:

$$c_v = \left\{X_{air}c_{v,air} + X_{ex}c_{v,ex} + X_{fuel}c_{v,fuel}\right\} \quad (8.49)$$

Equations (8.48) and (8.49) can be applied to equation (8.42) to yield:

$$mc_v\frac{dT}{dt} + e\frac{dm}{dt} = \dot{Q}_{com} - \dot{Q}_{ht} - P\frac{dV}{dt} + \dot{m}_{in}h_{in} - \dot{m}_{out}h_{out} - me_{air}\frac{dX_{air}}{dt} - me_{ex}\frac{dX_{ex}}{dt} - me_{fuel}\frac{dX_{fuel}}{dt} \quad (8.50)$$

The conservation of mass about control volume can be seen to be:

$$\frac{dm}{dt} = \dot{m}_{in} h_{in} - \dot{m}_{out} h_{out} \tag{8.51}$$

Applying equation (8.51) to (8.50) yields:

$$\frac{dT}{dt} = \frac{1}{mc_v}\left\{\dot{Q}_{com} - \dot{Q}_{ht} - P\frac{dV}{dt} + \dot{m}_{in}\left(h_{in} - e\right) - \dot{m}_{out}\left(h_{out} - e\right) - me_{air}\frac{dX_{air}}{dt} - me_{ex}\frac{dX_{ex}}{dt} - me_{fuel}\frac{dX_{fuel}}{dt}\right\} \tag{8.52}$$

The following relationship is known for the mass fractions:

$$X_{ex} + X_{fuel} + X_{air} = 1 \tag{8.53}$$

Differentiating equation (8.53) with respect to time yields:

$$\frac{dX_{air}}{dt} + \frac{dX_{ex}}{dt} + \frac{dX_{fuel}}{dt} = 0 \tag{8.54}$$

Equation (8.54) can be applied to equation (8.52) to eliminate the $\frac{dX_{air}}{dt}$ term:

$$\frac{dT}{dt} = \frac{1}{mc_v}\left\{\dot{Q}_{com} - \dot{Q}_{ht} - P\frac{dV}{dt} + \dot{m}_{in}\left(h_{in} - e\right) - \dot{m}_{out}\left(h_{out} - e\right) + \left(e_{air} - e_{ex}\right)m\frac{dX_{ex}}{dt} + \left(e_{air} - e_{fuel}\right)m\frac{dX_{fuel}}{dt}\right\} \tag{8.55}$$

8.2.1.1 Intake and Exhaust Manifolds

As a representative derivation for the engine manifolds, (8.55) can be applied to the intake manifold to yield (8.56). Note that the assumption of constant volume and absence of combustion eliminates terms.

$$\frac{dT_{im}}{dt} = \frac{1}{m_{im} c_{v,im}} \left\{ \begin{array}{l} \dot{m}_{th} \left(K_{th,im} - e_{im} \right) - \sum_{1}^{num_{cyl}} \left\{ \dot{m}_{iv} \left(i \right) \cdot \left(K_{iv,im} \left(i \right) - e_{im} \right) \right\} - \dot{Q}_{ht,im} + \ldots \\ \left(e_{air,im} - e_{ex,im} \right) m_{im} \frac{dX_{ex,im}}{dt} + \left(e_{air,im} - e_{fuel,im} \right) m_{im} \frac{dX_{fuel,im}}{dt} \end{array} \right\} \quad (8.56)$$

Where:

For $\dot{m}_{th} > 0$	*For* $\dot{m}_{th} < 0$	*For* $\dot{m}_{iv} > 0$	*For* $\dot{m}_{iv} < 0$
$K_{th,im} = h_0$	$K_{th,im} = h_{im}$	$K_{iv,im} = h_{im}$	$K_{iv,im} = h_{cyl}$

8.2.1.2 Cylinders

Equation (8.55) can be applied to the cylinder volumes to yield:

$$\frac{dT_{cyl}}{dt} = \frac{1}{m_{cyl} c_{v,cyl}} \left\{ \begin{array}{l} \frac{dQ_{com}}{dt} - \dot{Q}_{ht,cyl} - P_{cyl} \frac{dV_{cyl}}{dt} + \sum_{1}^{num_{cyl}} \left\{ \dot{m}_{iv} \left(i \right) \left(K_{iv,cyl} \left(i \right) - e_{cyl} \right) \right\} - \ldots \\ \sum_{1}^{num_{cyl}} \left\{ \dot{m}_{ev} \left(i \right) \left(K_{ev,cyl} \left(i \right) - e_{cyl} \right) \right\} + \left(e_{air,cyl} - e_{ex,cyl} \right) m_{cyl} \frac{dX_{ex,cyl}}{dt} + \ldots \\ \left(e_{air,cyl} - e_{fuel,cyl} \right) m_{cyl} \frac{dX_{fuel,cyl}}{dt} \end{array} \right\} \quad (8.57)$$

Where:

For $\dot{m}_{iv} > 0$	*For* $\dot{m}_{iv} < 0$	*For* $\dot{m}_{ev} > 0$	*For* $\dot{m}_{ev} < 0$
$K_{iv,cyl} = h_{im}$	$K_{iv} = h_{cyl}$	$K_{ev} = h_{cyl}$	$K_{ev} = h_{em}$

8.2.2 Species Concentration

Within the zero-dimensional, crank angle resolved model structure, three species concentrations are tracked: air, fuel and residual exhaust gases. These concentrations are tracked through differential equations governing their respective mass fractions. A generic derivation of the fictitious concentration Z presented below, followed by an application of the derivation to the three concentrations in the engine manifolds and cylinders.

Considering a generic zero-dimensional control volume (be it a manifold or a cylinder) the mass fraction of a species Z in the volume can be defined as:

$$X_Z = \frac{m_Z}{m} \tag{8.58}$$

Rearranging equation (8.58) and differentiating with respect to time yields:

$$\frac{dm_Z}{dt} = m\frac{dX_Z}{dt} + X_Z\frac{dm}{dt} \tag{8.59}$$

Additionally, a conservation of the quantity of Z in the volume can be defined in (8.60) as a function of the flux of Z entering and leaving the control volume.

$$\frac{dm_Z}{dt} = X_{Z,in}\dot{m}_{in} - X_{Z,out}\dot{m}_{out} \tag{8.60}$$

Equations (8.60) and (8.59) can be combined to yield:

$$\frac{dX_Z}{dt} = \frac{1}{m}\left\{ X_{Z,in}\dot{m}_{in} - X_Z\dot{m}_{out} - X_Z\frac{dm}{dt} \right\} \tag{8.61}$$

8.2.2.1 Intake and Exhaust Manifolds

As a representative derivation of the engine manifolds, (8.61) can be applied to the species of exhaust and fuel within the intake manifold to yield:

$$\frac{dX_{ex,im}}{dt} = \frac{1}{m_{im}}\left\{ \dot{m}_{th}K_{th,im,ex} - \sum_{1}^{num_{cyl}} \left\{ \dot{m}_{iv}(i)\cdot K_{iv,im,ex}(i) \right\} - X_{ex,im}\frac{dm_{im}}{dt} \right\} \tag{8.62}$$

$$\frac{dX_{fuel,im}}{dt} = \frac{1}{m_{im}}\left\{ \dot{m}_{th}K_{th,im,fuel} + \dot{m}_{fi} - \sum_{1}^{num_{cyl}} \left\{ \dot{m}_{iv}(i)\cdot K_{iv,im,fuel}(i) \right\} - X_{fuel,im}\frac{dm_{im}}{dt} \right\} \tag{8.63}$$

Where the 'K' parameters shown in equations (4.5) and (4.6) allow for flow reversal conditions, and are defined as:

For $\dot{m}_{th} > 0$	*For* $\dot{m}_{th} < 0$	*For* $\dot{m}_{iv} > 0$	*For* $\dot{m}_{iv} < 0$
$K_{th,im,ex} = 0$	$K_{th,im,ex} = X_{ex,im}$	$K_{iv,im,ex} = X_{ex,im}$	$K_{iv,im,ex} = X_{ex,cyl}$
$K_{th,im,fuel} = 0$	$K_{th,im,fuel} = X_{fuel,im}$	$K_{iv,im,fuel} = X_{fuel,im}$	$K_{iv,im,fuel} = X_{fuel,cyl}$

A differential equation is not required for the composition of air, since the three mass fractions must sum to one. Thus the mass fraction of air can be described through the algebraic relation shown in (8.64).

$$X_{air,im} = 1 - X_{ex,im} - X_{fuel,im} \tag{8.64}$$

8.2.2.2 Cylinders

The relations shown in (8.62) - (8.63) can be applied directly to the cylinder volume to yield:

$$\frac{dX_{ex,cyl}}{dt} = \frac{1}{m_{cyl}}\left\{\sum_{1}^{num_{cyl}}\left\{\dot{m}_{iv}(i)\cdot K_{iv,cyl}(i)\right\} - \sum_{1}^{num_{cyl}}\left\{\dot{m}_{ev}(i)\cdot K_{ev,cyl}(i)\right\} - X_{ex,cyl}\frac{dm_{cyl}}{dt}\right\} \quad (8.65)$$

$$\frac{dX_{fuel,cyl}}{dt} = \frac{1}{m_{cyl}}\left\{\sum_{1}^{num_{cyl}}\left\{\dot{m}_{iv}(i)\cdot K_{ivf,cyl}(i)\right\} - \sum_{1}^{num_{cyl}}\left\{\dot{m}_{ev}(i)\cdot K_{evf,cyl}(i)\right\} - X_{fuel,cyl}\frac{dm_{cyl}}{dt}\right\} \quad (8.66)$$

However, the conversion of fuel and air to exhaust products must be taken into account, through knowing that the conversion process follows the burn rate correlation to yield:

$$\frac{dX_{ex,cyl}}{dt} = \frac{1}{m_{cyl}}\left\{\sum_{1}^{num_{cyl}}\left\{\dot{m}_{iv}(i)\cdot K_{iv,cyl}(i)\right\} - \sum_{1}^{num_{cyl}}\left\{\dot{m}_{ev}(i)\cdot K_{ev,cyl}(i)\right\} + m_{charge,IVC}\frac{dX_b}{dt} - X_{ex,cyl}\frac{dm_{cyl}}{dt}\right\} \quad (8.67)$$

$$\frac{dX_{fuel,cyl}}{dt} = \frac{1}{m_{cyl}}\left\{\sum_{1}^{num_{cyl}}\left\{\dot{m}_{iv}(i)\cdot K_{ivf,cyl}(i)\right\} - \sum_{1}^{num_{cyl}}\left\{\dot{m}_{ev}(i)\cdot K_{evf,cyl}(i)\right\} + m_{fuel,IVC}\frac{dX_b}{dt} - X_{fuel,cyl}\frac{dm_{cyl}}{dt}\right\} \quad (8.68)$$

Where:

$For\ \dot{m}_{iv} > 0$	$For\ \dot{m}_{iv} < 0$	$For\ \dot{m}_{ev} > 0$	$For\ \dot{m}_{ev} < 0$
$K_{iv,cyl} = X_{ex,im}$	$K_{iv,cyl} = X_{ex,cyl}$	$K_{ev,cyl} = X_{ex,cyl}$	$K_{ev,cyl} = X_{ex,em}$
$K_{ivf,cyl} = X_{fuel,im}$	$K_{ivf,cyl} = X_{fuel,cyl}$	$K_{evf,cyl} = X_{fuel,cyl}$	$K_{evf,cyl} = X_{fuel,em}$

Again, the mass fraction of air can be found from the algebraic relation in (8.69):

$$X_{air,cyl} = 1 - X_{ex,cyl} - X_{fuel,cyl} \tag{8.69}$$

8.3 Buckeye Suite of Engineering Simulation Solutions

A collection of tools, interfaces and models have developed for the calibration, simulation and evaluation of different levels of engine models. These tools and models comprise an automated, standardized model development architecture complete with Graphical User Interfaces (GUIs). The software package has been designed to be universal and adaptable to different engine platforms and configurations with the intent of rapid, semi-automated model development to aid in control systems design applications.

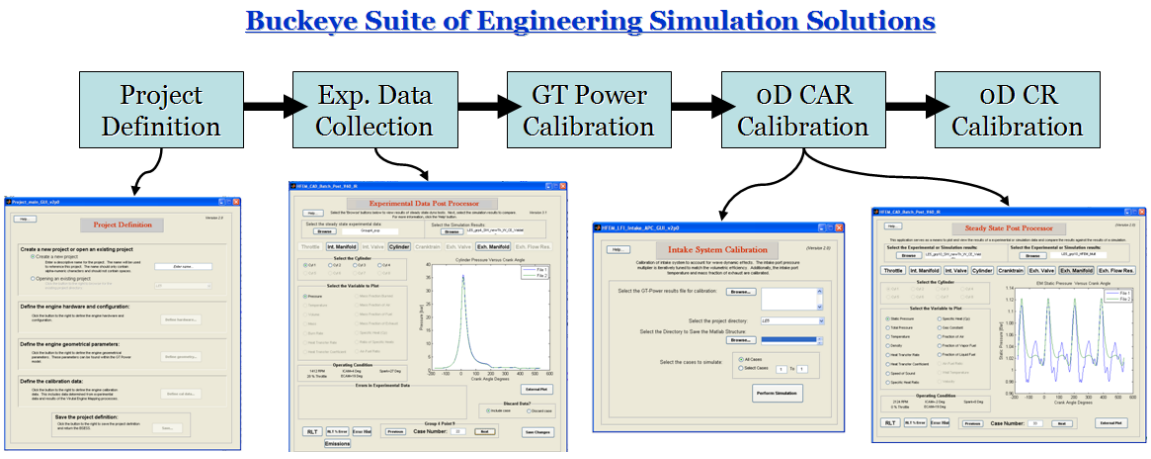

Figure 67: Buckeye Suite of Engineering Simulation Solutions

8.4 Model Order Reduction Derivations

8.4.1 Linear Convection Equation

The Linear Convection Equation, is shown in differential form in equation (8.70) below.

$$\frac{\partial u(x,t)}{\partial t} + c \cdot \frac{\partial u(x,t)}{\partial x} = 0 \tag{8.70}$$

Applying the model order reduction process from Section 5.2, we perform a spatial integration about (8.70) within a generic control volume:

$$\int_0^L \frac{\partial u(x,t)}{\partial t} \cdot dx + \int_0^L c \cdot \frac{\partial u(x,t)}{\partial x} \cdot dx = 0 \tag{8.71}$$

Equation (8.71) simplifies to:

$$\int_0^L \frac{\partial u(x,t)}{\partial t} \cdot dx = c\left(u(t, x=0) - u(t, x=L)\right) \tag{8.72}$$

Next, the spatial average value of u within control volume i can be defined as:

$$u_i^*(t) = \frac{1}{L}\int_0^L u(x,t) \cdot dx \tag{8.73}$$

Thus:

$$\frac{du_i^*(t)}{dt} = \frac{1}{L}\int_0^L \frac{\partial u(x,t)}{\partial t}\cdot dx \tag{8.74}$$

Applying (8.74) to (8.72) yields:

$$\frac{du_i^*(t)}{dt} = \frac{c}{L}\left(u(t,x=0) - u(t,x=L)\right) \tag{8.75}$$

The form of (8.75) can be closed through the definition of the spatial basis function, as defined in the following sections for polynomial representations.

8.4.1.1 Piecewise Constant Spatial Basis Function

The piecewise constant basis function is defined within a control volume as:

$$u(x,t)\Big|_0^L = \alpha_1(t) \tag{8.76}$$

Based upon this basis function, the spatial average variable can be defined as:

$$u_i^*(t) = \frac{1}{L}\int_0^L u(x,t)\cdot dx = \frac{1}{L}\int_0^L \alpha_1(t)\cdot dx = \alpha_1(t) \tag{8.77}$$

Thus the basis function can be written as:

$$u(x,t)\Big|_0^L = u_i^*(t) \tag{8.78}$$

The value at the end of volume can be found from the basis function to be:

$$u\left(t, x = L\right) = u_i^*\left(t\right) \tag{8.79}$$

8.4.1.2 Piecewise Linear Spatial Basis Function

The piecewise linear basis function is defined within two adjacent control volumes as:

$$u\left(x,t\right)\Big|_0^{2L} = \alpha_1\left(t\right) + \alpha_2\left(t\right)x \tag{8.80}$$

Based upon this basis function, the spatial average variables for the two adjacent control volumes can be defined as:

$$u_i^*\left(t\right) = \frac{1}{L}\int_0^L u\left(x,t\right)\cdot dx = \frac{1}{L}\int_0^L \alpha_1\left(t\right) + \alpha_2\left(t\right)x\cdot dx = \alpha_1\left(t\right) + \frac{\mathrm{L}}{2}\alpha_2\left(t\right) \tag{8.81}$$

$$u_{i+1}^*\left(t\right) = \frac{1}{L}\int_L^{2L} u\left(x,t\right)\cdot dx = \frac{1}{L}\int_L^{2L} \alpha_1\left(t\right) + \alpha_2\left(t\right)x\cdot dx = \alpha_1\left(t\right) + \frac{3\mathrm{L}}{2}\alpha_2\left(t\right) \tag{8.82}$$

Solving equations (8.81) and (8.82) for the unknown constants:

$$\alpha_1\left(t\right) = \frac{3}{2}u_i^*\left(t\right) - \frac{1}{2}u_{i+1}^*\left(t\right) \tag{8.83}$$

$$\alpha_2\left(t\right) = \frac{u_{i+1}^*\left(t\right) - u_i^*\left(t\right)}{L} \tag{8.84}$$

Substituting the unknown constants into the basis function, yields:

$$u(x,t)\Big|_0^{2L} = \left(\frac{3}{2} - \frac{x}{L}\right) u_i^*(t) + \left(\frac{x}{L} - \frac{1}{2}\right) u_{i+1}^*(t) \tag{8.85}$$

The value at the exit of volume can be found from the basis function to be:

$$u(t, x = L) = \frac{u_i^*(t) + u_{i+1}^*(t)}{2} \tag{8.86}$$

8.4.1.3 Piecewise Quadratic Spatial Basis Function

The piecewise quadratic basis function is defined within three adjacent control volumes as:

$$u(x,t)\Big|_{-L}^{2L} = \alpha_1(t) + \alpha_2(t)\,x + \alpha_3(t)\,x^2 \tag{8.87}$$

Based upon this basis function, the spatial average variables for the three adjacent control volumes can be defined as:

$$u_{i-1}^*(t) = \frac{1}{L}\int_{-L}^{0} \alpha_1(t) + \alpha_2(t)\,x + \alpha_3(t)\,x^2 \cdot dx = \alpha_1(t) - \frac{\mathrm{L}}{2}\alpha_2(t) + \frac{\mathrm{L}^2}{3}\alpha_3(t) \tag{8.88}$$

$$u_i^*(t) = \frac{1}{L}\int_{0}^{L} \alpha_1(t) + \alpha_2(t)\,x + \alpha_3(t)\,x^2 \cdot dx = \alpha_1(t) + \frac{\mathrm{L}}{2}\alpha_2(t) + \frac{\mathrm{L}^2}{3}\alpha_3(t) \tag{8.89}$$

$$u_{i+1}^*(t) = \frac{1}{L}\int_{L}^{2L} \alpha_1(t) + \alpha_2(t)\,x + \alpha_3(t)\,x^2 \cdot dx = \alpha_1(t) + \frac{3\mathrm{L}}{2}\alpha_2(t) + \frac{7\mathrm{L}^2}{3}\alpha_3(t) \tag{8.90}$$

Solving equations (8.88) - (8.90) for the unknown constants:

$$\alpha_1(t) = \frac{1}{3}u_{i-1}^*(t) + \frac{5}{6}u_i^*(t) - \frac{1}{6}u_{i+1}^*(t) \tag{8.91}$$

$$\alpha_2(t) = \frac{-u_{i-1}^*(t) + u_i^*(t)}{L} \tag{8.92}$$

$$\alpha_3(t) = \frac{u_{i-1}^*(t) - 2u_i^*(t) + u_{i+1}^*(t)}{2L^2} \tag{8.93}$$

Substituting the unknown constants into the basis function, yields:

$$u(x,t)\Big|_{-L}^{2L} = \left(\frac{1}{3} - \frac{x}{L} + \frac{x^2}{2L^2}\right)u_{i-1}^*(t) + \left(\frac{5}{6} + \frac{x}{L} - \frac{x^2}{L^2}\right)u_i^*(t) + \left(-\frac{1}{6} + \frac{x^2}{2L^2}\right)u_{i+1}^*(t) \tag{8.94}$$

The value at the exit of volume can be found from the basis function to be:

$$u(t, x = L) = -\frac{1}{6}u_{i-1}^*(t) + \frac{5}{6}u_i^*(t) + \frac{1}{3}u_{i+1}^*(t) \tag{8.95}$$

8.4.1.4 Piecewise Cubic Spatial Basis Function

The piecewise cubic basis function is defined within four adjacent control volumes as:

$$u(x,t)\Big|_{-L}^{3L} = \alpha_1(t) + \alpha_2(t)x + \alpha_3(t)x^2 + \alpha_4(t)x^3 \tag{8.96}$$

Based upon this basis function, the spatial average variables for the four adjacent control volumes can be defined as:

$$u_{i-1}^{*}(t)=\frac{1}{L}\int_{-L}^{0}\alpha_1(t)+\alpha_2(t)x+\alpha_3(t)x^2+\alpha_4(t)x^3\cdot dx=\alpha_1(t)-\frac{\mathrm{L}}{2}\alpha_2(t)+\frac{\mathrm{L}^2}{3}\alpha_3(t)-\frac{\mathrm{L}^3}{4}\alpha_4(t) \quad (8.97)$$

$$u_{i}^{*}(t)=\frac{1}{L}\int_{0}^{L}\alpha_1(t)+\alpha_2(t)x+\alpha_3(t)x^2+\alpha_4(t)x^3\cdot dx=\alpha_1(t)+\frac{\mathrm{L}}{2}\alpha_2(t)+\frac{\mathrm{L}^2}{3}\alpha_3(t)+\frac{\mathrm{L}^3}{4}\alpha_4(t) \quad (8.98)$$

$$u_{i+1}^{*}(t)=\frac{1}{L}\int_{L}^{2L}\alpha_1(t)+\alpha_2(t)x+\alpha_3(t)x^2+\alpha_4(t)x^3\cdot dx=\alpha_1(t)+\frac{3\mathrm{L}}{2}\alpha_2(t)+\frac{7\mathrm{L}^2}{3}\alpha_3(t)+\frac{15\mathrm{L}^3}{4}\alpha_4(t) \quad (8.99)$$

$$u_{i+2}^{*}(t)=\frac{1}{L}\int_{2L}^{3L}\alpha_1(t)+\alpha_2(t)x+\alpha_3(t)x^2+\alpha_4(t)x^3\cdot dx=\alpha_1(t)+\frac{5\mathrm{L}}{2}\alpha_2(t)+\frac{19\mathrm{L}^2}{3}\alpha_3(t)+\frac{65\mathrm{L}^3}{4}\alpha_4(t) \quad (8.100)$$

Solving equations (8.97) - (8.100) for the unknown constants:

$$\alpha_1(t)=\frac{1}{4}u_{i-1}^{*}(t)+\frac{13}{12}u_{i}^{*}(t)-\frac{5}{12}u_{i+1}^{*}(t)+\frac{1}{12}u_{i+2}^{*}(t) \quad (8.101)$$

$$\alpha_2(t)=\frac{-11u_{i-1}^{*}(t)+9u_{i}^{*}(t)+3u_{i+1}^{*}(t)-u_{i+2}^{*}(t)}{12L} \quad (8.102)$$

$$\alpha_3(t)=\frac{3u_{i-1}^{*}(t)-7u_{i}^{*}(t)+5u_{i+1}^{*}(t)-u_{i+2}^{*}(t)}{4L^2} \quad (8.103)$$

$$\alpha_4(t)=\frac{-u_{i-1}^{*}(t)+3u_{i}^{*}(t)-3u_{i+1}^{*}(t)+u_{i+2}^{*}(t)}{6L^3} \quad (8.104)$$

Substituting the unknown constants into the basis function, yields:

$$u(x,t)\Big|_{-L}^{3L}=\left(\frac{1}{4}-\frac{11x}{12L}+\frac{3x^2}{4L^2}-\frac{x^3}{6L^3}\right)u_{i-1}^{*}(t)+\left(\frac{13}{12}+\frac{3x}{4L}-\frac{7x^2}{4L^2}+\frac{x^3}{2L^3}\right)u_{i}^{*}(t)+\left(-\frac{5}{12}+\frac{x}{4L}+\frac{5x^2}{4L^2}-\frac{x^3}{2L^3}\right)u_{i+1}^{*}(t)+\left(\frac{1}{12}-\frac{x}{12L}-\frac{x^2}{4L^2}+\frac{x^3}{6L^3}\right)u_{i+2}^{*}(t) \quad (8.105)$$

The value at the exit of volume can be found from the basis function to be:

$$u\left(t, x=L\right)=-\frac{1}{12}u_{i-1}^{*}\left(t\right)+\frac{7}{12}u_{i}^{*}\left(t\right)+\frac{7}{12}u_{i+1}^{*}\left(t\right)-\frac{1}{12}u_{i+2}^{*}\left(t\right) \tag{8.106}$$

8.4.2 Linear Euler Equations

The linear Euler Equations, are shown in differential form in equations (8.107) and (8.108) below.

$$\frac{\partial\rho\left(x,t\right)}{\partial t}+u_0\frac{\partial\rho\left(x,t\right)}{\partial x}+\rho_0\frac{\partial u\left(x,t\right)}{\partial x}=0 \tag{8.107}$$

$$\frac{\partial u\left(x,t\right)}{\partial t}+u_0\frac{\partial u\left(x,t\right)}{\partial x}+\frac{c^2}{\rho_0}\frac{\partial\rho\left(x,t\right)}{\partial x}=0 \tag{8.108}$$

Beginning with the continuity equation, applying the model order reduction process from Section 5.2, we perform a spatial integration within the generic control volume:

$$\int_0^L\frac{\partial\rho\left(x,t\right)}{\partial t}\cdot dx+\int_0^L u_0\frac{\partial\rho\left(x,t\right)}{\partial x}\cdot dx+\int_0^L\rho_0\frac{\partial u\left(x,t\right)}{\partial x}\cdot dx=0 \tag{8.109}$$

Equation (8.109) simplifies to:

$$\int_0^L\frac{\partial\rho\left(x,t\right)}{\partial t}\cdot dx=u_0\left(\rho\left(t,x=0\right)-\rho\left(t,x=L\right)\right)+\rho_0\left(u\left(t,x=0\right)-u\left(t,x=L\right)\right) \tag{8.110}$$

Next, integrating the momentum equation about a control volume that is staggered with respect to the continuity volume yields:

$$\int_{.5L}^{1.5L} \frac{\partial u(x,t)}{\partial t} \cdot dx + \int_{.5L}^{1.5L} u_0 \frac{\partial u(x,t)}{\partial x} \cdot dx + \int_{.5L}^{1.5L} \frac{c^2}{\rho_0} \frac{\partial \rho(x,t)}{\partial x} \cdot dx = 0 \tag{8.111}$$

Equation (8.111) simplifies to:

$$\int_{.5L}^{1.5L} \frac{\partial u(x,t)}{\partial t} \cdot dx = u_0 \left(u\left(t, x = \frac{L}{2}\right) - u\left(t, x = \frac{3L}{2}\right)\right) + \frac{c^2}{\rho_0}\left(\rho\left(t, x = \frac{L}{2}\right) - \rho\left(t, x = \frac{3L}{2}\right)\right) \tag{8.112}$$

The spatial average values of ρ and u within volumes i and j can be defined as:

$$\rho_i^*(t) = \frac{1}{L}\int_0^L \rho(x,t) \cdot dx \tag{8.113}$$

$$u_j^*(t) = \frac{1}{L}\int_{.5L}^{1.5L} u(x,t) \cdot dx \tag{8.114}$$

Thus:

$$\frac{d\rho_i^*(t)}{dt} = \frac{1}{L}\int_0^L \frac{\partial \rho(x,t)}{\partial t} \cdot dx \tag{8.115}$$

$$\frac{du_j^*(t)}{dt} = \frac{1}{L}\int_{.5}^{1.5L} \frac{\partial u(x,t)}{\partial t} \cdot dx \tag{8.116}$$

Applying (8.115) and (8.116) to (8.110) and (8.112) yields:

$$\frac{d\rho_i^*(t)}{dt} = \frac{u_0}{L}\left(\rho(t, x=0) - \rho(t, x=L)\right) + \frac{\rho_0}{L}\left(u(t, x=0) - u(t, x=L)\right) \quad (8.117)$$

$$\frac{du_j^*(t)}{dt} = u_0\left(u\left(t, x=\frac{L}{2}\right) - u\left(t, x=\frac{3L}{2}\right)\right) + \frac{c^2}{\rho_0}\left(\rho\left(t, x=\frac{L}{2}\right) - \rho\left(t, x=\frac{3L}{2}\right)\right) \quad (8.118)$$

The form of (8.117) and (8.118) can be closed through the definition of the spatial basis function, as defined in the following sections for polynomial representations.

8.4.2.1 Piecewise Constant Spatial Basis Function

The piecewise constant basis functions are defined within two separate sets of control volumes: the first contains a single control volume where a basis function is defined for the density; the second, staggered from the first, contains a single control volume for the velocity basis function:

$$\rho(x,t)\Big|_0^L = \alpha_1(t) \quad (8.119)$$

$$u(x,t)\Big|_{.5L}^{1.5L} = \beta_1(t) \quad (8.120)$$

Based upon these basis functions, the spatial average variables can be defined as:

$$\rho_i^*(t) = \frac{1}{L}\int_0^L \alpha_1(t)\cdot dx = \alpha_1(t) \quad (8.121)$$

$$u_j^*(t) = \frac{1}{L}\int_{.5L}^{1.5L} \beta_1(t)\cdot dx = \beta_1(t) \tag{8.122}$$

Thus the basis functions can be written as:

$$\rho(x,t)\Big|_0^L = \rho_i^*(t) \tag{8.123}$$

$$u(x,t)\Big|_{.5L}^{1.5L} = u_j^*(t) \tag{8.124}$$

The fluxes leaving control volumes i and j can now be found:

$$u(t, x = L) = u_j^*(t) \tag{8.125}$$

$$u\left(t, x = \frac{3L}{2}\right) = u_j^*(t) \tag{8.126}$$

$$\rho(t, x = L) = \rho_i^*(t) \tag{8.127}$$

$$\rho\left(t, x = \frac{3L}{2}\right) = \rho_{i+1}^*(t) \tag{8.128}$$

8.4.2.2 Piecewise Linear Spatial Basis Function

The piecewise linear basis functions are defined within two separate sets of control volumes: the first contains two adjacent control volumes where a basis function is

defined for the density; the second, staggered from the first, contains two adjacent control volumes for the velocity basis function:

$$\rho(x,t)\Big|_0^{2L} = \alpha_1(t) + \alpha_2(t)\,x \tag{8.129}$$

$$u(x,t)\Big|_{.5L}^{2.5L} = \beta_1(t) + \beta_2(t)\,x \tag{8.130}$$

Based upon these basis functions, the spatial average variables can be defined as:

$$\rho_i^*(t) = \frac{1}{L}\int_0^L \alpha_1(t) + \alpha_2(t)\,x \cdot dx = \alpha_1(t) + \frac{L}{2}\alpha_2(t) \tag{8.131}$$

$$\rho_{i+1}^*(t) = \frac{1}{L}\int_L^{2L} \alpha_1(t) + \alpha_2(t)\,x \cdot dx = \alpha_1(t) + \frac{3L}{2}\alpha_2(t) \tag{8.132}$$

$$u_j^*(t) = \frac{1}{L}\int_{.5L}^{1.5L} \beta_1(t) + \beta_2(t)\,x \cdot dx = \beta_1(t) + L\beta_2(t) \tag{8.133}$$

$$u_{j+1}^*(t) = \frac{1}{L}\int_{1.5L}^{2.5L} \beta_1(t) + \beta_2(t)\,x \cdot dx = \beta_1(t) + 2L\beta_2(t) \tag{8.134}$$

Equations (8.131) - (8.134) can be solved for the unknown variables:

$$\alpha_1(t) = \frac{3}{2}\rho_i^*(t) - \frac{1}{2}\rho_{i+1}^*(t) \tag{8.135}$$

$$\alpha_2(t) = \frac{-\rho_i^*(t) + \rho_{i+1}^*(t)}{L} \tag{8.136}$$

$$\beta_1(t) = 2u_j^*(t) - u_{j+1}^*(t) \tag{8.137}$$

$$\beta_2(t) = \frac{-u_j^*(t) + u_{j+1}^*(t)}{L} \tag{8.138}$$

Substituting the unknown parameters into the basis functions yields:

$$\rho(x,t)\Big|_0^{2L} = \left(\frac{3}{2} - \frac{x}{L}\right)\rho_i^*(t) + \left(-\frac{1}{2} + \frac{x}{L}\right)\rho_{i+1}^*(t) \tag{8.139}$$

$$u(x,t)\Big|_{.5L}^{2.5L} = \left(2 - \frac{x}{L}\right)u_j^*(t) + \left(-1 + \frac{x}{L}\right)u_{j+1}^*(t) \tag{8.140}$$

The fluxes leaving control volumes i and j can now be found:

$$\rho(t, x = L) = \frac{\rho_i^*(t) + \rho_{i+1}^*(t)}{2} \tag{8.141}$$

$$\rho\left(t, x = \frac{3L}{2}\right) = \rho_{i+1}^*(t) \tag{8.142}$$

$$u(t, x = L) = u_j^*(t) \tag{8.143}$$

$$u\left(t, x = \frac{3L}{2}\right) = \frac{u_j^*(t) + u_{j+1}^*(t)}{2} \tag{8.144}$$

8.4.2.3 Piecewise Quadratic Spatial Basis Function

The piecewise quadratic basis functions are defined within two separate sets of control volumes: the first contains three adjacent control volumes where a basis function is defined for the density; the second, staggered from the first, contains three adjacent control volumes for the velocity basis function:

$$\rho(x,t)\Big|_{-L}^{2L} = \alpha_1(t) + \alpha_2(t)x + \alpha_3(t)x^2 \tag{8.145}$$

$$u(x,t)\Big|_{-.5L}^{2.5L} = \beta_1(t) + \beta_2(t)x + \beta_3(t)x^2 \tag{8.146}$$

Based upon these basis functions, the spatial average variables can be defined as:

$$\rho_{i-1}^*(t) = \frac{1}{L}\int_{-L}^{0} \alpha_1(t) + \alpha_2(t)x + \alpha_3(t)x^2 \cdot dx = \alpha_1(t) - \frac{L}{2}\alpha_2(t) + \frac{L^2}{3}\alpha_3(t) \tag{8.147}$$

$$\rho_i^*(t) = \frac{1}{L}\int_{0}^{L} \alpha_1(t) + \alpha_2(t)x + \alpha_3(t)x^2 \cdot dx = \alpha_1(t) + \frac{L}{2}\alpha_2(t) + \frac{L^2}{3}\alpha_3(t) \tag{8.148}$$

$$\rho_{i+1}^*(t) = \frac{1}{L}\int_{L}^{2L} \alpha_1(t) + \alpha_2(t)x + \alpha_3(t)x^2 \cdot dx = \alpha_1(t) + \frac{3L}{2}\alpha_2(t) + \frac{7L^2}{2}\alpha_3(t) \tag{8.149}$$

$$u_{j-1}^*(t) = \frac{1}{L}\int_{-.5L}^{.5L} \beta_1(t) + \beta_2(t)x + \beta_3(t)x^2 \cdot dx = \beta_1(t) + \frac{L^2}{12}\beta_3(t) \tag{8.150}$$

$$u_j^*(t) = \frac{1}{L}\int_{.5L}^{1.5L} \beta_1(t) + \beta_2(t)x + \beta_3(t)x^2 \cdot dx = \beta_1(t) + L\beta_2(t) + \frac{13L^2}{12}\beta_3(t) \tag{8.151}$$

$$u_{j+1}^{*}(t)=\frac{1}{L}\int_{1.5L}^{2.5L}\beta_1(t)+\beta_2(t)x+\beta_3(t)x^2\cdot dx=\beta_1(t)+2L\beta_2(t)+\frac{49L^2}{12}\beta_3(t) \quad (8.152)$$

Equations (8.147) - (8.152) can be solved for the unknown variables:

$$\alpha_1(t)=\frac{1}{3}\rho_{i-1}^{*}(t)+\frac{5}{6}\rho_i^{*}(t)-\frac{1}{6}\rho_{i+1}^{*}(t) \quad (8.153)$$

$$\alpha_2(t)=\frac{-\rho_{i-1}^{*}(t)+\rho_i^{*}(t)}{L} \quad (8.154)$$

$$\alpha_3(t)=\frac{\rho_{i-1}^{*}(t)-2\rho_i^{*}(t)+\rho_{i+1}^{*}(t)}{2L^2} \quad (8.155)$$

$$\beta_1(t)=\frac{23}{24}u_{j-1}^{*}(t)+\frac{2}{24}u_j^{*}(t)-\frac{1}{24}u_{j+1}^{*}(t) \quad (8.156)$$

$$\beta_2(t)=\frac{-3u_{j-1}^{*}(t)+4u_j^{*}(t)-u_{j+1}^{*}(t)}{2L} \quad (8.157)$$

$$\beta_3(t)=\frac{u_{j-1}^{*}(t)-2u_j^{*}(t)+u_{j+1}^{*}(t)}{2L^2} \quad (8.158)$$

Substituting the unknown parameters into the basis functions yields:

$$\rho(x,t)\Big|_{-L}^{2L}=\left(\frac{1}{3}-\frac{x}{L}+\frac{x^2}{2L^2}\right)\rho_{i-1}^{*}(t)+\left(\frac{5}{6}+\frac{x}{L}-\frac{x^2}{L^2}\right)\rho_i^{*}(t)+\left(-\frac{1}{6}+\frac{x^2}{2L^2}\right)\rho_{i+1}^{*}(t) \quad (8.159)$$

$$u(x,t)\Big|_{-.5L}^{2.5L}=\left(\frac{23}{24}-\frac{3x}{2L}+\frac{x^2}{2L^2}\right)u_{j-1}^{*}(t)+\left(\frac{1}{12}+\frac{2x}{L}-\frac{x^2}{L^2}\right)u_j^{*}(t)+\left(-\frac{1}{24}-\frac{x}{2L}+\frac{x^2}{2L^2}\right)u_{j+1}^{*}(t) \quad (8.160)$$

The fluxes leaving control volumes i and j can now be found:

$$\rho\left(t, x = L\right) = -\frac{1}{6}\rho_{i-1}^{*}\left(t\right) + \frac{5}{6}\rho_{i}^{*}\left(t\right) + \frac{1}{3}\rho_{i+1}^{*}\left(t\right) \tag{8.161}$$

$$\rho\left(t, x = \frac{3L}{2}\right) = -\frac{1}{24}\rho_{i-1}^{*}\left(t\right) + \frac{1}{12}\rho_{i}^{*}\left(t\right) + \frac{23}{24}\rho_{i+1}^{*}\left(t\right) \tag{8.162}$$

$$u\left(t, x = L\right) = -\frac{1}{24}u_{j-1}^{*}\left(t\right) + \frac{13}{12}u_{j}^{*}\left(t\right) - \frac{1}{24}u_{j+1}^{*}\left(t\right) \tag{8.163}$$

$$u\left(t, x = \frac{3L}{2}\right) = -\frac{1}{6}u_{j-1}^{*}\left(t\right) + \frac{5}{6}u_{j}^{*}\left(t\right) + \frac{1}{3}u_{j+1}^{*}\left(t\right) \tag{8.164}$$

8.4.2.4 Piecewise Cubic Spatial Basis Function

The piecewise cubic basis functions are defined within two separate sets of control volumes: the first contains four adjacent control volumes where a basis function is defined for the density; the second, staggered from the first, contains four adjacent control volumes for the velocity basis function:

$$\rho\left(x,t\right)\Big|_{-L}^{3L} = \alpha_1\left(t\right) + \alpha_2\left(t\right)x + \alpha_3\left(t\right)x^2 + \alpha_4\left(t\right)x^3 \tag{8.165}$$

$$u\left(x,t\right)\Big|_{-.5L}^{3.5L} = \beta_1\left(t\right) + \beta_2\left(t\right)x + \beta_3\left(t\right)x^2 + \beta_4\left(t\right)x^3 \tag{8.166}$$

Based upon these basis functions, the spatial average variables can be defined as:

$$\rho_{i-1}^{*}(t)=\frac{1}{L}\int_{-L}^{0}\alpha_1(t)+\alpha_2(t)x+\alpha_3(t)x^2+\alpha_4(t)x^3\cdot dx=\alpha_1(t)-\frac{L}{2}\alpha_2(t)+\frac{L^2}{3}\alpha_3(t)-\frac{L^3}{4}\alpha_4(t) \quad (8.167)$$

$$\rho_{i}^{*}(t)=\frac{1}{L}\int_{0}^{L}\alpha_1(t)+\alpha_2(t)x+\alpha_3(t)x^2+\alpha_4(t)x^3\cdot dx=\alpha_1(t)+\frac{L}{2}\alpha_2+\frac{L^2}{3}\alpha_3(t)+\frac{L^3}{4}\alpha_4(t) \quad (8.168)$$

$$\rho_{i+1}^{*}(t)=\frac{1}{L}\int_{L}^{2L}\alpha_1(t)+\alpha_2(t)x+\alpha_3(t)x^2+\alpha_4(t)x^3\cdot dx=\alpha_1(t)+\frac{3L}{2}\alpha_2(t)+\frac{7L^2}{3}\alpha_3(t)+\frac{15L^3}{4}\alpha_4(t) \quad (8.169)$$

$$\rho_{i+2}^{*}(t)=\frac{1}{L}\int_{2L}^{3L}\alpha_1(t)+\alpha_2(t)x+\alpha_3(t)x^2+\alpha_4(t)x^3\cdot dx=\alpha_1(t)+\frac{5L}{2}\alpha_2(t)+\frac{19L^2}{3}\alpha_3(t)+\frac{64L^3}{4}\alpha_4(t) \quad (8.170)$$

$$u_{j-1}^{*}(t)=\frac{1}{L}\int_{-.5L}^{.5L}\beta_1(t)+\beta_2(t)x+\beta_3(t)x^2+\beta_4(t)x^3\cdot dx=\beta_1(t)+\frac{L^2}{12}\beta_3(t) \quad (8.171)$$

$$u_{j}^{*}(t)=\frac{1}{L}\int_{.5L}^{1.5L}\beta_1(t)+\beta_2(t)x+\beta_3(t)x^2+\beta_4(t)x^3\cdot dx=\beta_1(t)+L\beta_2(t)+\frac{13L^2}{12}\beta_3(t)+\frac{5L^3}{4}\beta_4(t) \quad (8.172)$$

$$u_{j+1}^{*}(t)=\frac{1}{L}\int_{1.5L}^{2.5L}\beta_1(t)+\beta_2(t)x+\beta_3(t)x^2+\beta_4(t)x^3\cdot dx=\beta_1(t)+2L\beta_2(t)+\frac{49L^2}{12}\beta_3(t)+\frac{17L^3}{2}\beta_4(t) \quad (8.173)$$

$$u_{j+2}^{*}(t)=\frac{1}{L}\int_{2.5L}^{3.5L}\beta_1(t)+\beta_2(t)x+\beta_3(t)x^2+\beta_4(t)x^3\cdot dx=\beta_1(t)+3L\beta_2(t)+\frac{109L^2}{12}\beta_3(t)+\frac{111L^3}{4}\beta_4(t) \quad (8.174)$$

Equations (8.167) - (8.174) can be solved for the unknown variables:

$$\alpha_1(t)=\frac{1}{4}\rho_{i-1}^{*}(t)+\frac{13}{12}\rho_{i}^{*}(t)-\frac{5}{12}\rho_{i+1}^{*}(t)+\frac{1}{12}\rho_{i+2}^{*}(t) \quad (8.175)$$

$$\alpha_2(t)=\frac{-11\rho_{i-1}^{*}(t)+9\rho_i^{*}(t)+3\rho_{i+1}^{*}(t)-\rho_{i+2}^{*}(t)}{12L} \tag{8.176}$$

$$\alpha_3(t)=\frac{3\rho_{i-1}^{*}(t)-7\rho_i^{*}(t)+5\rho_{i+1}^{*}(t)-\rho_{i+2}^{*}(t)}{4L^2} \tag{8.177}$$

$$\alpha_4(t)=\frac{-\rho_{i-1}^{*}(t)+3\rho_i^{*}(t)-3\rho_{i+1}^{*}(t)+\rho_{i+2}^{*}(t)}{6L^3} \tag{8.178}$$

$$\beta_1(t)=\frac{11}{12}u_{j-1}^{*}(t)+\frac{5}{24}u_j^{*}(t)-\frac{1}{6}u_{j+1}^{*}(t)+\frac{1}{24}u_{j+2}^{*}(t) \tag{8.179}$$

$$\beta_2(t)=\frac{-43u_{j-1}^{*}(t)+69u_j^{*}(t)-33u_{j+1}^{*}(t)+7u_{j+2}^{*}(t)}{24L} \tag{8.180}$$

$$\beta_3(t)=\frac{2u_{j-1}^{*}(t)-5u_j^{*}(t)+4u_{j+1}^{*}(t)-u_{j+2}^{*}(t)}{2L^2} \tag{8.181}$$

$$\beta_4(t)=\frac{-u_{j-1}^{*}(t)+3u_j^{*}(t)-3u_{j+1}^{*}(t)+u_{j+2}^{*}(t)}{6L^3} \tag{8.182}$$

Substituting the unknown parameters into the basis functions yields:

$$\rho(x,t)\Big|_{-L}^{3L}=\left(\frac{1}{4}-\frac{11x}{12L}+\frac{3x^2}{4L^2}-\frac{x^3}{6L^3}\right)\rho_{i-1}^{*}(t)+\left(\frac{13}{12}+\frac{3x}{4L}-\frac{7x^2}{4L^2}+\frac{x^3}{2L^3}\right)\rho_i^{*}(t)+\left(-\frac{5}{12}+\frac{x}{4L}+\frac{5x^2}{4L^2}-\frac{x^3}{2L^3}\right)\rho_{i+1}^{*}(t)+\left(\frac{1}{12}-\frac{x}{12L}-\frac{x^2}{4L^2}+\frac{x^3}{6L^3}\right)\rho_{i+2}^{*}(t) \tag{8.183}$$

$$u(x,t)\Big|_{-.5L}^{3.5L}=\left(\frac{11}{12}-\frac{43x}{24L}+\frac{x^2}{L^2}-\frac{x^3}{6L^3}\right)u_{j-1}^{*}(t)+\left(\frac{5}{24}+\frac{23x}{8L}-\frac{5x^2}{2L^2}+\frac{x^3}{2L^3}\right)u_j^{*}(t)+\left(-\frac{1}{6}-\frac{11x}{8L}+\frac{2x^2}{L^2}-\frac{x^3}{2L^3}\right)u_{j+1}^{*}(t)+\left(\frac{1}{24}+\frac{7x}{24L}-\frac{x^2}{2L^2}+\frac{x^3}{6L^3}\right)u_{j+2}^{*}(t) \tag{8.184}$$

The fluxes leaving control volumes i and j can now be found:

$$\rho\left(t, x = L\right) = -\frac{1}{12}\rho_{i-1}^{*}\left(t\right) + \frac{7}{12}\rho_{i}^{*}\left(t\right) + \frac{7}{12}\rho_{i+1}^{*}\left(t\right) - \frac{1}{12}\rho_{i+2}^{*}\left(t\right) \tag{8.185}$$

$$\rho\left(t, x = \frac{3L}{2}\right) = -\frac{1}{24}\rho_{i}^{*}\left(t\right) + \frac{13}{12}\rho_{i+1}^{*}\left(t\right) - \frac{1}{24}\rho_{i+2}^{*}\left(t\right) \tag{8.186}$$

$$u\left(t, x = L\right) = -\frac{1}{24}u_{j-1}^{*}\left(t\right) + \frac{13}{12}u_{j}^{*}\left(t\right) - \frac{1}{24}u_{j+1}^{*}\left(t\right) \tag{8.187}$$

$$u\left(t, x = \frac{3L}{2}\right) = -\frac{1}{12}u_{j-1}^{*}\left(t\right) + \frac{7}{12}u_{j}^{*}\left(t\right) + \frac{7}{12}u_{j+1}^{*}\left(t\right) - \frac{1}{12}u_{j+2}^{*}\left(t\right) \tag{8.188}$$

8.4.3 Euler Equations

The one-dimensional, constant area Euler Equations are shown in differential form in equations (8.189) - (8.191) below.

$$\frac{\partial\left(\rho\left(x,t\right)A\right)}{\partial t} + \frac{\partial\left(\rho\left(x,t\right)Au\left(x,t\right)\right)}{\partial x} = 0 \tag{8.189}$$

$$\frac{\partial\left(\rho\left(x,t\right)Au\left(x,t\right)\right)}{\partial t} + \frac{\partial\left(\rho\left(x,t\right)Au\left(x,t\right)^{2} + P\left(x,t\right)A\right)}{\partial x} = 0 \tag{8.190}$$

$$\frac{\partial\left(\rho\left(x,t\right)Ae_{0}\left(x,t\right)\right)}{\partial t} + \frac{\partial\left(\rho\left(x,t\right)Au\left(x,t\right)h_{0}\left(x,t\right)\right)}{\partial x} = 0 \tag{8.191}$$

These equations are modified by defining the mass flux of gas traveling within the components, the pressure and the enthalpy as follows :

$$\dot{m}(x,t) = \rho(x,t)\, A u(x,t) \tag{8.192}$$

$$P(x,t) = (\gamma - 1)\rho(x,t)\left(e_0 - \frac{\dot{m}(x,t)^2}{2\rho(x,t)^2 A^2} \right) \tag{8.193}$$

$$h_0(x,t) = e_0(x,t) + \frac{P(x,t)}{\rho(x,t)} = \gamma e_0(x,t) + (1-\gamma)\frac{\dot{m}(x,t)^2}{2\rho(x,t)^2 A^2} \tag{8.194}$$

Applying (8.192) - (8.194) to equations (8.189) - (8.191) yields:

$$\frac{\partial(\rho(x,t)A)}{\partial t} + \frac{\partial \dot{m}(x,t)}{\partial x} = 0 \tag{8.195}$$

$$\frac{\partial \dot{m}(x,t)}{\partial t} + \frac{\partial\left((\gamma-1)\rho(x,t) A e_0(x,t) + \frac{\dot{m}(x,t)^2 (3-\gamma)}{2\rho(x,t)A} \right)}{\partial x} = 0 \tag{8.196}$$

$$\frac{\partial(\rho(x,t) A e_0(x,t))}{\partial t} + \frac{\partial\left(\gamma \dot{m}(x,t) e_0(x,t) + (1-\gamma)\frac{\dot{m}(x,t)^3}{2\rho(x,t)^2 A^2} \right)}{\partial x} = 0 \tag{8.197}$$

Beginning with the continuity equation, applying the model order reduction process from Section 5.2, we perform a spatial integration within the generic control volume:

$$\int_0^L \frac{\partial(\rho(x,t)A)}{\partial t} \cdot dx + \int_0^L \frac{\partial \dot{m}(x,t)}{\partial x} \cdot dx = 0 \tag{8.198}$$

Equation (8.198) simplifies to:

$$\int_0^L \frac{\partial\left(\rho(x,t)\,A\right)}{\partial t}\cdot dx = \dot{m}\left(t,x=0\right)-\dot{m}\left(t,x=L\right) \tag{8.199}$$

The spatial average value of ρ within control volume i can be defined as:

$$\rho_i^*\left(t\right)=\frac{1}{L}\int_0^L \rho\left(x,t\right)\cdot dx \tag{8.200}$$

Thus:

$$\frac{d\rho_i^*\left(t\right)}{dt}=\frac{1}{L}\int_0^L \frac{\partial\rho\left(x,t\right)}{\partial t}\cdot dx \tag{8.201}$$

Applying (8.201) to (8.199) yields:

$$AL\frac{d\rho_i^*\left(t\right)}{dt}=\dot{m}\left(t,x=0\right)-\dot{m}\left(t,x=L\right) \tag{8.202}$$

Next, integrating the conservation of energy about the same control volume yields:

$$\int_0^L \frac{\partial\left(\rho(x,t)\,Ae_0\left(x,t\right)\right)}{\partial t}\cdot dx+\int_0^L \frac{\partial\left(\gamma\dot{m}\left(x,t\right)e_0\left(x,t\right)+\left(1-\gamma\right)\dfrac{\dot{m}\left(x,t\right)^3}{2\rho\left(x,t\right)^2A^2}\right)}{\partial x}\cdot dx=0 \tag{8.203}$$

Equation (8.203) simplifies to:

$$\int_0^L \frac{\partial\left(\rho\left(x,t\right)Ae_0\left(x,t\right)\right)}{\partial t}\cdot dx = \gamma\dot{m}\left(t,x=0\right)e_0\left(t,x=0\right)+\left(1-\gamma\right)\frac{\dot{m}\left(t,x=0\right)^3}{2\rho\left(t,x=0\right)^2A^2}-\ldots$$
$$\gamma\dot{m}\left(t,x=L\right)e_0\left(t,x=L\right)-\left(1-\gamma\right)\frac{\dot{m}\left(t,x=L\right)^3}{2\rho\left(t,x=L\right)^2A^2} \tag{8.204}$$

The spatial average value of the product $\left(\rho e_0\right)$ within control volume i can be defined as:

$$\left(\rho e_0\right)_i^*\left(t\right)=\frac{1}{L}\int_0^L \rho\left(x,t\right)e_0\left(x,t\right)\cdot dx \tag{8.205}$$

Thus:

$$\frac{d\left(\rho e_0\right)_i^*\left(t\right)}{dt}=\frac{1}{L}\int_0^L \frac{\partial\left(\rho\left(x,t\right)e_0\left(x,t\right)\right)}{\partial t}\cdot dx \tag{8.206}$$

Applying (8.206) to (8.204) yields:

$$AL\frac{d\left(\rho e_0\right)_i^*\left(t\right)}{dt} = \gamma\dot{m}\left(t,x=0\right)e_0\left(t,x=0\right)+\left(1-\gamma\right)\frac{\dot{m}\left(t,x=0\right)^3}{2\rho\left(t,x=0\right)^2A^2}-\ldots$$
$$\gamma\dot{m}\left(t,x=L\right)e_0\left(t,x=L\right)-\left(1-\gamma\right)\frac{\dot{m}\left(t,x=L\right)^3}{2\rho\left(t,x=L\right)^2A^2} \tag{8.207}$$

Finally, integrating the momentum equation about a control volume that is staggered with respect to the continuity and energy volume yields:

$$\int_{.5L}^{1.5L} \frac{\partial \dot{m}(x,t)}{\partial t} \cdot dx + \int_{.5L}^{1.5L} \frac{\partial \left((\gamma - 1)\rho(x,t) A e_0(x,t) + \frac{\dot{m}(x,t)^2 (3-\gamma)}{2\rho(x,t) A} \right)}{\partial x} \cdot dx = 0 \quad (8.208)$$

Equation (8.208) simplifies to:

$$\int_{.5L}^{1.5L} \frac{\partial \dot{m}(x,t)}{\partial t} \cdot dx = (\gamma - 1)\rho\left(t, x = \frac{L}{2}\right) A e_0\left(t, x = \frac{L}{2}\right) + \frac{\dot{m}\left(t, x = \frac{L}{2}\right)^2 (3-\gamma)}{2\rho\left(t, x = \frac{L}{2}\right) A} - \ldots$$
$$(\gamma - 1)\rho\left(t, x = \frac{3L}{2}\right) A e_0\left(t, x = \frac{3L}{2}\right) - \frac{\dot{m}\left(t, x = \frac{3L}{2}\right)^2 (3-\gamma)}{2\rho\left(t, x = \frac{3L}{2}\right) A} \quad (8.209)$$

The spatial average value of $\dot{m}$ within control volume j can be defined as:

$$\dot{m}_j^*(t) = \frac{1}{L} \int_{.5L}^{2.5L} \dot{m}(x,t) \cdot dx \quad (8.210)$$

Thus:

$$\frac{d\dot{m}_j^*(t)}{dt} = \frac{1}{L} \int_{.5L}^{2.5L} \frac{\partial \dot{m}(x,t)}{\partial t} \cdot dx \quad (8.211)$$

Applying (8.211) to (8.209) yields:

$$L\frac{d\dot{m}_j^*(t)}{dt}=(\gamma-1)\rho\left(t,x=\frac{L}{2}\right)Ae_0\left(t,x=\frac{L}{2}\right)+\frac{\dot{m}\left(t,x=\frac{L}{2}\right)^2(3-\gamma)}{2\rho\left(t,x=\frac{L}{2}\right)A}-\ldots$$
$$(\gamma-1)\rho\left(t,x=\frac{3L}{2}\right)Ae_0\left(t,x=\frac{3L}{2}\right)-\frac{\dot{m}\left(t,x=\frac{3L}{2}\right)^2(3-\gamma)}{2\rho\left(t,x=\frac{3L}{2}\right)A} \tag{8.212}$$

Summarizing, we have the following three equations which can be closed through the definition of the Spatial Basis Functions.

$$AL\frac{d\rho_i^*(t)}{dt}=\dot{m}(t,x=0)-\dot{m}(t,x=L) \tag{8.213}$$

$$AL\frac{d(\rho e_0)_i^*(t)}{dt}=\gamma\dot{m}(t,x=0)e_0(t,x=0)+(1-\gamma)\frac{\dot{m}(t,x=0)^3}{2\rho(t,x=0)^2A^2}-\ldots$$
$$\gamma\dot{m}(t,x=L)e_0(t,x=L)-(1-\gamma)\frac{\dot{m}(t,x=L)^3}{2\rho(t,x=L)^2A^2} \tag{8.214}$$

$$L\frac{d\dot{m}_j^*(t)}{dt}=(\gamma-1)\rho\left(t,x=\frac{L}{2}\right)Ae_0\left(t,x=\frac{L}{2}\right)+\frac{\dot{m}\left(t,x=\frac{L}{2}\right)^2(3-\gamma)}{2\rho\left(t,x=\frac{L}{2}\right)A}-\ldots$$
$$(\gamma-1)\rho\left(t,x=\frac{3L}{2}\right)Ae_0\left(t,x=\frac{3L}{2}\right)-\frac{\dot{m}\left(t,x=\frac{3L}{2}\right)^2(3-\gamma)}{2\rho\left(t,x=\frac{3L}{2}\right)A} \tag{8.215}$$

8.4.3.1 Piecewise Constant Spatial Basis Function

The piecewise constant basis functions are defined within two separate sets of control volumes: the first contains a single control volume where basis functions are defined for the density and for the total internal energy; the second, staggered from the first, contains a single control volume for the mass flux basis function:

$$\rho(x,t)\Big|_0^L = \alpha_1(t) \tag{8.216}$$

$$e_0(x,t)\Big|_0^L = \beta_1(t) \tag{8.217}$$

$$\dot{m}(x,t)\Big|_{.5L}^{1.5L} = \chi_1(t) \tag{8.218}$$

Based upon these basis functions, the spatial average variables can be defined as:

$$\rho_i^*(t) = \frac{1}{L}\int_0^L \alpha_1 \cdot dx = \alpha_1(t) \tag{8.219}$$

$$(e_0)_i^*(t) = \frac{1}{L}\int_0^L \beta_1 \cdot dx = \beta_1(t) \tag{8.220}$$

$$\dot{m}_j^*(t) = \frac{1}{L}\int_{.5L}^{1.5L} \chi_1 \cdot dx = \chi_1(t) \tag{8.221}$$

Thus the basis functions can be written as:

$$\rho(x,t)\Big|_0^L = \rho_i^*(t) \tag{8.222}$$

$$e_0(x,t)\Big|_0^L = e_{0,i}^*(t) \tag{8.223}$$

$$\dot{m}(x,t)\Big|_{.5L}^{1.5L} = \dot{m}_j^*(t) \tag{8.224}$$

Furthermore, we can see that

$$(e_0\rho)_i^*(t) = \frac{1}{L}\int_0^L \alpha_1(t)\cdot\beta_1(t)\cdot dx = \alpha_1(t)\cdot\beta_1(t) \tag{8.225}$$

Such that:

$$(e_0\rho)_i^*(t) = e_{0,i}^*(t)\cdot\rho_i^*(t) \tag{8.226}$$

The fluxes leaving control volumes i and j can now be found:

$$\rho(t, x = L) = \rho_i^*(t) \tag{8.227}$$

$$\rho\left(t, x = \frac{3L}{2}\right) = \rho_{i+1}^*(t) \tag{8.228}$$

$$e_0(t, x = L) = e_{0,i}^*(t) \tag{8.229}$$

$$e_0\left(t, x = \frac{3L}{2}\right) = e_{0,i+1}^*(t) \tag{8.230}$$

$$\dot{m}\left(t, x = L\right) = \dot{m}_j^*\left(t\right) \tag{8.231}$$

$$\dot{m}\left(t, x = \frac{3L}{2}\right) = \dot{m}_j^*\left(t\right) \tag{8.232}$$

8.4.3.2 Piecewise Linear Spatial Basis Function

The piecewise linear basis functions are defined within two separate sets of control volumes: the first contains two adjacent control volumes where basis functions are defined for the density and for the total internal energy; the second, staggered from the first, contains two adjacent control volumes for the mass flux basis function:

$$\rho\left(x,t\right)\Big|_0^{2L} = \alpha_1\left(t\right) + \alpha_2\left(t\right)x \tag{8.233}$$

$$e_0\left(x,t\right)\Big|_0^{2L} = \beta_1\left(t\right) + \beta_2\left(t\right)x \tag{8.234}$$

$$\dot{m}\left(x,t\right)\Big|_{.5L}^{2.5L} = \chi_1\left(t\right) + \chi_2\left(t\right)x \tag{8.235}$$

Based upon these basis functions, the spatial average variables can be defined as:

$$\rho_i^*\left(t\right) = \frac{1}{L}\int_0^L \alpha_1\left(t\right) + \alpha_2\left(t\right)x \cdot dx = \alpha_1\left(t\right) + \frac{L}{2}\alpha_2\left(t\right) \tag{8.236}$$

$$\rho_{i+1}^*\left(t\right) = \frac{1}{L}\int_L^{2L} \alpha_1\left(t\right) + \alpha_2\left(t\right)x \cdot dx = \alpha_1\left(t\right) + \frac{3L}{2}\alpha_2\left(t\right) \tag{8.237}$$

$$e_{0,i}^{*}(t)=\frac{1}{L}\int_{0}^{L}\beta_1(t)+\beta_2(t)x\cdot dx=\beta_1(t)+\frac{L}{2}\beta_2(t) \tag{8.238}$$

$$e_{0,i+1}^{*}(t)=\frac{1}{L}\int_{L}^{2L}\beta_1(t)+\beta_2(t)x\cdot dx=\beta_1(t)+\frac{3L}{2}\beta_2(t) \tag{8.239}$$

$$\dot{m}_{j}^{*}(t)=\frac{1}{L}\int_{.5L}^{1.5L}\chi_1(t)+\chi_2(t)x\cdot dx=\chi_1(t)+L\chi_2(t) \tag{8.240}$$

$$\dot{m}_{j+1}^{*}(t)=\frac{1}{L}\int_{1.5L}^{2.5L}\chi_1(t)+\chi_2(t)x\cdot dx=\chi_1(t)+2L\chi_2(t) \tag{8.241}$$

Furthermore, we can see that

$$\left(e_0\rho\right)_i^{*}(t)=\frac{1}{L}\int_{0}^{L}\left(\alpha_1(t)+\alpha_2(t)x\right)\cdot\left(\beta_1(t)+\beta_2(t)x\right)\cdot dx \tag{8.242}$$

Such that:

$$\left(e_0\rho\right)_i^{*}(t)=\left(\frac{13}{12}\rho_i^{*}(t)-\frac{1}{12}\rho_{i+1}^{*}(t)\right)e_{0,i}^{*}(t)+\left(-\frac{1}{12}\rho_i^{*}(t)+\frac{1}{12}\rho_{i+1}^{*}(t)\right)e_{0,i+1}^{*}(t) \tag{8.243}$$

Equations (8.236) - (8.241) can be solved for the unknown variables:

$$\alpha_1(t)=\frac{3}{2}\rho_i^{*}(t)-\frac{1}{2}\rho_{i+1}^{*}(t) \tag{8.244}$$

$$\alpha_2(t)=\frac{-\rho_i^{*}(t)+\rho_{i+1}^{*}(t)}{L} \tag{8.245}$$

$$\beta_1(t) = \frac{3}{2} e_{0,i}^{*}(t) - \frac{1}{2} e_{0,i+1}^{*}(t) \tag{8.246}$$

$$\beta_2(t) = \frac{-e_{0,i}^{*}(t) + e_{0,i+1}^{*}(t)}{L} \tag{8.247}$$

$$\chi_1(t) = 2\dot{m}_j^{*}(t) - \dot{m}_{j+1}^{*}(t) \tag{8.248}$$

$$\chi_2(t) = \frac{-\dot{m}_j^{*}(t) + \dot{m}_{j+1}^{*}(t)}{L} \tag{8.249}$$

Substituting the unknown parameters into the basis functions yields:

$$\rho(x,t)\Big|_0^{2L} = \left(\frac{3}{2} - \frac{x}{L}\right)\rho_i^{*}(t) + \left(-\frac{1}{2} + \frac{x}{L}\right)\rho_{i+1}^{*}(t) \tag{8.250}$$

$$e_0(x,t)\Big|_0^{2L} = \left(\frac{3}{2} - \frac{x}{L}\right)e_{0,i}^{*}(t) + \left(-\frac{1}{2} + \frac{x}{L}\right)e_{0,i+1}^{*}(t) \tag{8.251}$$

$$\dot{m}(x,t)\Big|_{.5L}^{2.5L} = \left(2 - \frac{x}{L}\right)\dot{m}_j^{*}(t) + \left(-1 + \frac{x}{L}\right)\dot{m}_{j+1}^{*}(t) \tag{8.252}$$

The fluxes leaving control volumes i and j can now be found:

$$\rho(t, x = L) = \frac{\rho_i^{*}(t) + \rho_{i+1}^{*}(t)}{2} \tag{8.253}$$

$$\rho\left(t, x = \frac{3L}{2}\right) = \rho_{i+1}^{*}(t) \tag{8.254}$$

$$e_0\left(t, x = L\right) = \frac{e^*_{0,i}\left(t\right) + e^*_{0,i+1}\left(t\right)}{2} \tag{8.255}$$

$$e_0\left(t, x = \frac{3L}{2}\right) = e^*_{0,i+1}\left(t\right) \tag{8.256}$$

$$\dot{m}\left(t, x = L\right) = \dot{m}^*_j\left(t\right) \tag{8.257}$$

$$\dot{m}\left(t, x = \frac{3L}{2}\right) = \frac{\dot{m}^*_j\left(t\right) + \dot{m}^*_{j+1}\left(t\right)}{2} \tag{8.258}$$

8.4.3.3 Piecewise Quadratic Spatial Basis Function

The piecewise quadratic basis functions are defined within two separate sets of control volumes: the first contains three adjacent control volumes where basis functions are defined for the density and for the total internal energy; the second, staggered from the first, contains three adjacent control volumes for the mass flux basis function:

$$\rho\left(x,t\right)\Big|_{-L}^{2L} = \alpha_1\left(t\right) + \alpha_2\left(t\right)x + \alpha_3\left(t\right)x^2 \tag{8.259}$$

$$e_0\left(x,t\right)\Big|_{-L}^{2L} = \beta_1\left(t\right) + \beta_2\left(t\right)x + \beta_3\left(t\right)x^2 \tag{8.260}$$

$$\dot{m}\left(x,t\right)\Big|_{-.5L}^{2.5L} = \chi_1\left(t\right) + \chi_2\left(t\right)x + \chi_3\left(t\right)x^2 \tag{8.261}$$

Based upon these basis functions, the spatial average variables can be defined as:

$$\rho_{i-1}^{*}(t)=\frac{1}{L}\int_{-L}^{0}\alpha_1(t)+\alpha_2(t)x+\alpha_3(t)x^2\cdot dx=\alpha_1(t)-\frac{L}{2}\alpha_2(t)+\frac{L^2}{3}\alpha_3(t) \quad (8.262)$$

$$\rho_{i}^{*}(t)=\frac{1}{L}\int_{0}^{L}\alpha_1(t)+\alpha_2(t)x+\alpha_3(t)x^2\cdot dx=\alpha_1(t)+\frac{L}{2}\alpha_2(t)+\frac{L^2}{3}\alpha_3(t) \quad (8.263)$$

$$\rho_{i+1}^{*}(t)=\frac{1}{L}\int_{L}^{2L}\alpha_1(t)+\alpha_2(t)x+\alpha_3(t)x^2\cdot dx=\alpha_1(t)+\frac{3L}{2}\alpha_2(t)+\frac{7L^2}{3}\alpha_3(t) \quad (8.264)$$

$$e_{0,i-1}^{*}(t)=\frac{1}{L}\int_{-L}^{0}\beta_1(t)+\beta_2(t)x+\beta_3(t)x^2\cdot dx=\beta_1(t)-\frac{L}{2}\beta_2(t)+\frac{L^2}{3}\beta_3(t) \quad (8.265)$$

$$e_{0,i}^{*}(t)=\frac{1}{L}\int_{0}^{L}\beta_1(t)+\beta_2(t)x+\beta_3(t)x^2\cdot dx=\beta_1(t)+\frac{L}{2}\beta_2(t)+\frac{L^2}{3}\beta_3(t) \quad (8.266)$$

$$e_{0,i+1}^{*}(t)=\frac{1}{L}\int_{L}^{2L}\beta_1(t)+\beta_2(t)x+\beta_3(t)x^2\cdot dx=\beta_1(t)+\frac{3L}{2}\beta_2(t)+\frac{7L^2}{3}\beta_3(t) \quad (8.267)$$

$$\dot{m}_{j-1}^{*}(t)=\frac{1}{L}\int_{-.5L}^{.5L}\chi_1(t)+\chi_2(t)x+\chi_3(t)x^2\cdot dx=\chi_1(t)+L^2\chi_3(t) \quad (8.268)$$

$$\dot{m}_{j}^{*}(t)=\frac{1}{L}\int_{.5L}^{1.5L}\chi_1(t)+\chi_2(t)x+\chi_3(t)x^2\cdot dx=\chi_1(t)+L\chi_2(t)+\frac{13}{12}L^2\chi_3(t) \quad (8.269)$$

$$\dot{m}_{j+1}^{*}(t)=\frac{1}{L}\int_{1.5L}^{2.5L}\chi_1(t)+\chi_2(t)x+\chi_3(t)x^2\cdot dx=\chi_1(t)+2L\chi_2(t)+\frac{49}{12}L^2\chi_3(t) \quad (8.270)$$

Furthermore, we can see that

$$\left(e_0\rho\right)_i^*\left(t\right)=\frac{1}{L}\int_0^L\left(\alpha_1\left(t\right)+\alpha_2\left(t\right)x+\alpha_3\left(t\right)x^2\right)\cdot\left(\beta_1\left(t\right)+\beta_2\left(t\right)x+\beta_3\left(t\right)x^2\right)\cdot dx \quad (8.271)$$

Such that:

$$\begin{aligned}\left(e_0\rho\right)_i^*\left(t\right)=&\left(\frac{1}{45}\rho_{i-1}^*\left(t\right)-\frac{1}{360}\rho_i^*\left(t\right)-\frac{7}{360}\rho_{i+1}^*\left(t\right)\right)e_{0,i-1}^*\left(t\right)+\ldots\\&\left(-\frac{1}{360}\rho_{i-1}^*\left(t\right)+\frac{181}{180}\rho_i^*\left(t\right)-\frac{1}{360}\rho_{i+1}^*\left(t\right)\right)e_{0,i}^*\left(t\right)+\ldots\\&\left(-\frac{7}{360}\rho_{i-1}^*\left(t\right)-\frac{1}{360}\rho_i^*\left(t\right)+\frac{1}{45}\rho_{i+1}^*\left(t\right)\right)e_{0,i+1}^*\left(t\right)\end{aligned} \quad (8.272)$$

Equations (8.262) - (8.270) can be solved for the unknown variables:

$$\alpha_1\left(t\right)=\frac{1}{3}\rho_{i-1}^*\left(t\right)+\frac{5}{6}\rho_i^*\left(t\right)-\frac{1}{6}\rho_{i+1}^*\left(t\right) \quad (8.273)$$

$$\alpha_2\left(t\right)=\frac{-\rho_{i-1}^*\left(t\right)+\rho_i^*\left(t\right)}{L} \quad (8.274)$$

$$\alpha_3\left(t\right)=\frac{\rho_{i-1}^*\left(t\right)-2\rho_i^*\left(t\right)+\rho_{i+1}^*\left(t\right)}{2L^2} \quad (8.275)$$

$$\beta_1\left(t\right)=\frac{1}{3}e_{0,i-1}^*\left(t\right)+\frac{5}{6}e_{0,i}^*\left(t\right)-\frac{1}{6}e_{0,i+1}^*\left(t\right) \quad (8.276)$$

$$\beta_2\left(t\right)=\frac{-e_{0,i-1}^*\left(t\right)+e_{0,i}^*\left(t\right)}{L} \quad (8.277)$$

$$\beta_3(t) = \frac{e^*_{0,i-1}(t) - 2e^*_{0,i}(t) + e^*_{0,i+1}(t)}{2L^2} \tag{8.278}$$

$$\chi_1(t) = \frac{23}{24}\dot{m}^*_{j-1}(t) + \frac{1}{12}\dot{m}^*_j(t) - \frac{1}{24}\dot{m}^*_{j+1}(t) \tag{8.279}$$

$$\chi_2(t) = \frac{-3\dot{m}^*_{j-1}(t) + 4\dot{m}^*_j(t) - \dot{m}^*_{j+1}(t)}{2L} \tag{8.280}$$

$$\chi_3(t) = \frac{\dot{m}^*_{j-1}(t) - 2\dot{m}^*_j(t) + \dot{m}^*_{j+1}(t)}{2L^2} \tag{8.281}$$

Substituting the unknown parameters into the basis functions yields:

$$\rho(x,t)\Big|_{-L}^{2L} = \left(\frac{1}{3} - \frac{x}{L} + \frac{x^2}{2L^2}\right)\rho^*_{i-1}(t) + \left(\frac{5}{6} + \frac{x}{L} - \frac{x^2}{L^2}\right)\rho^*_i(t) + \left(-\frac{1}{6} + \frac{x^2}{2L^2}\right)\rho^*_{i+1}(t) \tag{8.282}$$

$$e_0(x,t)\Big|_{-L}^{2L} = \left(\frac{1}{3} - \frac{x}{L} + \frac{x^2}{2L^2}\right)e^*_{0,i-1}(t) + \left(\frac{5}{6} + \frac{x}{L} - \frac{x^2}{L^2}\right)e^*_{0,i}(t) + \left(-\frac{1}{6} + \frac{x^2}{2L^2}\right)e^*_{0,i+1}(t) \tag{8.283}$$

$$\dot{m}(x,t)\Big|_{-.5L}^{2.5L} = \left(\frac{23}{24} - \frac{3x}{2L} + \frac{x^2}{2L^2}\right)\dot{m}^*_{j-1}(t) + \left(\frac{1}{12} + \frac{2x}{L} - \frac{x^2}{L^2}\right)\dot{m}^*_j(t) + \left(-\frac{1}{24} - \frac{x}{2L} + \frac{x^2}{2L^2}\right)\dot{m}^*_{j+1}(t) \tag{8.284}$$

The fluxes leaving control volumes i and j can now be found:

$$\rho(t, x = L) = \frac{-\rho^*_{i-1}(t) + 5\rho^*_i(t) + 2\rho^*_{i+1}(t)}{6} \tag{8.285}$$

$$\rho\left(t, x=\frac{3L}{2}\right)=-\frac{1}{24}\rho_{i-1}^{*}(t)+\frac{1}{12}\rho_{i}^{*}(t)+\frac{23}{24}\rho_{i+1}^{*}(t) \tag{8.286}$$

$$e_0(t, x=L)=\frac{-e_{0,i-1}^{*}(t)+5e_{0,i}^{*}(t)+2e_{0,i+1}^{*}(t)}{6} \tag{8.287}$$

$$e_0\left(t, x=\frac{3L}{2}\right)=-\frac{1}{24}e_{0,i-1}^{*}(t)+\frac{1}{12}e_{0,i}^{*}(t)+\frac{23}{24}e_{0,i+1}^{*}(t) \tag{8.288}$$

$$\dot{m}(t, x=L)=-\frac{1}{24}\dot{m}_{j-1}^{*}(t)+\frac{13}{12}\dot{m}_{j}^{*}(t)-\frac{1}{24}\dot{m}_{j+1}^{*}(t) \tag{8.289}$$

$$\dot{m}\left(t, x=\frac{3L}{2}\right)=-\frac{1}{6}\dot{m}_{j-1}^{*}(t)+\frac{5}{6}\dot{m}_{j}^{*}(t)+\frac{1}{3}\dot{m}_{j+1}^{*}(t) \tag{8.290}$$

8.4.3.4 Piecewise Cubic Spatial Basis Function

The piecewise cubic basis functions are defined within two separate sets of control volumes: the first contains four adjacent control volumes where basis functions are defined for the density and for the total internal energy; the second, staggered from the first, contains four adjacent control volumes for the mass flux basis function:

$$\rho(x,t)\Big|_{-L}^{3L}=\alpha_1(t)+\alpha_2(t)x+\alpha_3(t)x^2+\alpha_4(t)x^3 \tag{8.291}$$

$$e_0(x,t)\Big|_{-L}^{3L}=\beta_1(t)+\beta_2(t)x+\beta_3(t)x^2+\beta_4(t)x^3 \tag{8.292}$$

$$\dot{m}(x,t)\Big|_{-.5L}^{3.5L}=\chi_1(t)+\chi_2(t)x+\chi_3(t)x^2+\chi_4(t)x^3 \tag{8.293}$$

Based upon these basis functions, the spatial average variables can be defined as:

$$\rho_{i-1}^{*}(t)=\frac{1}{L}\int_{-L}^{0}\alpha_1(t)+\alpha_2(t)x+\alpha_3(t)x^2+\alpha_4(t)x^3\cdot dx=\alpha_1(t)-\frac{L}{2}\alpha_2(t)+\frac{L^2}{3}\alpha_3(t)-\frac{L^3}{4}\alpha_4(t) \quad (8.294)$$

$$\rho_{i}^{*}(t)=\frac{1}{L}\int_{0}^{L}\alpha_1(t)+\alpha_2(t)x+\alpha_3(t)x^2+\alpha_4(t)x^3\cdot dx=\alpha_1(t)+\frac{L}{2}\alpha_2(t)+\frac{L^2}{3}\alpha_3(t)+\frac{L^3}{4}\alpha_4(t) \quad (8.295)$$

$$\rho_{i+1}^{*}(t)=\frac{1}{L}\int_{L}^{2L}\alpha_1(t)+\alpha_2(t)x+\alpha_3(t)x^2+\alpha_4(t)x^3\cdot dx=\alpha_1(t)+\frac{3L}{2}\alpha_2(t)+\frac{7L^2}{3}\alpha_3(t)+\frac{15L^3}{4}\alpha_4(t) \quad (8.296)$$

$$\rho_{i+2}^{*}(t)=\frac{1}{L}\int_{2L}^{3L}\alpha_1(t)+\alpha_2(t)x+\alpha_3(t)x^2+\alpha_4(t)x^3\cdot dx=\alpha_1(t)+\frac{5L}{2}\alpha_2(t)+\frac{19L^2}{3}\alpha_3(t)+\frac{65L^3}{4}\alpha_4(t) \quad (8.297)$$

$$e_{0,i-1}^{*}(t)=\frac{1}{L}\int_{-L}^{0}\beta_1(t)+\beta_2(t)x+\beta_3(t)x^2+\beta_4(t)x^3\cdot dx=\beta_1(t)-\frac{L}{2}\beta_2(t)+\frac{L^2}{3}\beta_3(t)-\frac{L^3}{4}\beta_4(t) \quad (8.298)$$

$$e_{0,i}^{*}(t)=\frac{1}{L}\int_{0}^{L}\beta_1(t)+\beta_2(t)x+\beta_3(t)x^2+\beta_4(t)x^3\cdot dx=\beta_1(t)+\frac{L}{2}\beta_2(t)+\frac{L^2}{3}\beta_3(t)+\frac{L^3}{4}\beta_4(t) \quad (8.299)$$

$$e_{0,i+1}^{*}(t)=\frac{1}{L}\int_{L}^{2L}\beta_1(t)+\beta_2(t)x+\beta_3(t)x^2+\beta_4(t)x^3\cdot dx=\beta_1(t)+\frac{3L}{2}\beta_2(t)+\frac{7L^2}{3}\beta_3(t)+\frac{15L^3}{4}\beta_4(t) \quad (8.300)$$

$$e_{0,i+2}^{*}(t)=\frac{1}{L}\int_{2L}^{3L}\beta_1(t)+\beta_2(t)x+\beta_3(t)x^2+\beta_4(t)x^3\cdot dx=\beta_1(t)+\frac{5L}{2}\beta_2(t)+\frac{19L^2}{3}\beta_3(t)+\frac{65L^3}{4}\beta_4(t) \quad (8.301)$$

$$\dot{m}_{j-1}^{*}(t)=\frac{1}{L}\int_{-.5L}^{.5L}\chi_1(t)+\chi_2(t)x+\chi_3(t)x^2+\chi_4(t)x^3\cdot dx=\chi_1(t)+\frac{L^2}{12}\chi_3(t) \quad (8.302)$$

$$\dot{m}_j^*(t)=\frac{1}{L}\int_{.5L}^{1.5L}\chi_1(t)+\chi_2(t)x+\chi_3(t)x^2+\chi_4(t)x^3\cdot dx=\chi_1(t)+L\chi_2(t)+\frac{13}{12}L^2\chi_3(t)+\frac{5}{4}L^3\chi_4(t) \quad (8.303)$$

$$\dot{m}_{j+1}^*(t)=\frac{1}{L}\int_{1.5L}^{2.5L}\chi_1(t)+\chi_2(t)x+\chi_3(t)x^2+\chi_4(t)x^3\cdot dx=\chi_1(t)+2L\chi_2(t)+\frac{49}{12}L^2\chi_3(t)+\frac{17}{2}L^3\chi_4(t) \quad (8.304)$$

$$\dot{m}_{j+2}^*(t)=\frac{1}{L}\int_{2.5L}^{3.5L}\chi_1(t)+\chi_2(t)x+\chi_3(t)x^2+\chi_4(t)x^3\cdot dx=\chi_1(t)+3L\chi_2(t)+\frac{109}{12}L^2\chi_3(t)+\frac{111}{4}L^3\chi_4(t) \quad (8.305)$$

Furthermore, we can see that

$$\left(e_0\rho\right)_i^*(t)=\frac{1}{L}\int_0^L\left(\alpha_1(t)+\alpha_2(t)x+\alpha_3(t)x^2+\alpha_4(t)x^3\right)\left(\beta_1(t)+\beta_2(t)x+\beta_3(t)x^2+\beta_4(t)x^3\right)\cdot dx \quad (8.306)$$

Such that:

$$\begin{aligned}\left(e_0\rho\right)_i^*(t)=&\left(\frac{59}{6048}\rho_{i-1}^*(t)+\frac{59}{5040}\rho_i^*(t)-\frac{53}{2016}\rho_{i+1}^*(t)+\frac{73}{15120}\rho_{i+2}^*(t)\right)e_{0,i-1}^*+\ldots\\&\left(\frac{59}{5040}\rho_{i-1}^*(t)+\frac{10391}{10080}\rho_i^*(t)-\frac{257}{5040}\rho_{i+1}^*(t)+\frac{17}{2016}\rho_{i+2}^*(t)\right)e_{0,i}^*+\ldots\\&\left(-\frac{53}{2016}\rho_{i-1}^*(t)-\frac{257}{5040}\rho_i^*(t)+\frac{941}{10080}\rho_{i+1}^*(t)-\frac{9}{560}\rho_{i+2}^*(t)\right)e_{0,i+1}^*(t)+\ldots\\&\left(\frac{73}{15120}\rho_{i-1}^*(t)+\frac{17}{2016}\rho_i^*(t)-\frac{9}{560}\rho_{i+1}^*(t)+\frac{17}{6048}\rho_{i+2}^*(t)\right)e_{0,i+2}^*(t)\end{aligned} \quad (8.307)$$

Equations (8.294) - (8.305) can be solved for the unknown variables:

$$\alpha_1(t)=\frac{1}{4}\rho_{i-1}^*(t)+\frac{13}{12}\rho_i^*(t)-\frac{5}{12}\rho_{i+1}^*(t)+\frac{1}{12}\rho_{i+2}^*(t) \quad (8.308)$$

$$\alpha_2(t)=\frac{-11\rho^*_{i-1}(t)+9\rho^*_i(t)+3\rho^*_{i+1}(t)-\rho^*_{i+2}(t)}{12L} \tag{8.309}$$

$$\alpha_3(t)=\frac{3\rho^*_{i-1}(t)-7\rho^*_i(t)+5\rho^*_{i+1}(t)-\rho^*_{i+2}(t)}{4L^2} \tag{8.310}$$

$$\alpha_4(t)=\frac{-\rho^*_{i-1}(t)+3\rho^*_i(t)-3\rho^*_{i+1}(t)+\rho^*_{i+2}(t)}{6L^3} \tag{8.311}$$

$$\beta_1(t)=\frac{1}{4}e^*_{0,i-1}(t)+\frac{13}{12}e^*_{0,i}(t)-\frac{5}{12}e^*_{0,i+1}(t)+\frac{1}{12}e^*_{0,i+2}(t) \tag{8.312}$$

$$\beta_2(t)=\frac{-11e^*_{0,i-1}(t)+9e^*_{0,i}(t)+3e^*_{0,i+1}(t)-e^*_{0,i+2}(t)}{12L} \tag{8.313}$$

$$\beta_3(t)=\frac{3e^*_{0,i-1}(t)-7e^*_{0,i}(t)+5e^*_{0,i+1}(t)-e^*_{0,i+2}(t)}{4L^2} \tag{8.314}$$

$$\beta_4(t)=\frac{-e^*_{0,i-1}(t)+3e^*_{0,i}(t)-3e^*_{0,i+1}(t)+e^*_{0,i+2}(t)}{6L^3} \tag{8.315}$$

$$\chi_1(t)=\frac{11}{12}\dot{m}^*_{j-1}(t)+\frac{5}{24}\dot{m}^*_j(t)-\frac{1}{6}\dot{m}^*_{j+1}(t)+\frac{1}{24}\dot{m}^*_{j+2}(t) \tag{8.316}$$

$$\chi_2(t)=\frac{-43\dot{m}^*_{j-1}(t)+69\dot{m}^*_j(t)-33\dot{m}^*_{j+1}(t)+7\dot{m}^*_{j+2}(t)}{24L} \tag{8.317}$$

$$\chi_3(t)=\frac{2\dot{m}^*_{j-1}(t)-5\dot{m}^*_j(t)+4\dot{m}^*_{j+1}(t)-\dot{m}^*_{j+2}(t)}{2L^2} \tag{8.318}$$

$$\chi_4(t) = \frac{-\dot{m}^*_{j-1}(t) + 3\dot{m}^*_j(t) - 3\dot{m}^*_{j+1}(t) + \dot{m}^*_{j+2}(t)}{6L^3} \tag{8.319}$$

Substituting the unknown parameters into the basis functions yields:

$$\rho(x,t)\Big|_{-L}^{3L} = \left(\frac{1}{4} - \frac{11x}{12L} + \frac{3x^2}{4L^2} - \frac{x^3}{6L^3}\right)\rho^*_{i-1}(t) + \left(\frac{13}{12} + \frac{3x}{4L} - \frac{7x^2}{4L^2} + \frac{x^3}{2L^3}\right)\rho^*_i(t) + \ldots$$
$$\left(-\frac{5}{12} + \frac{x}{4L} + \frac{5x^2}{4L^2} - \frac{x^3}{2L^3}\right)\rho^*_{i+1}(t) + \left(\frac{1}{12} - \frac{x}{12L} - \frac{x^2}{4L^2} + \frac{x^3}{6L^3}\right)\rho^*_{i+2}(t) \tag{8.320}$$

$$e_0(x,t)\Big|_{-L}^{3L} = \left(\frac{1}{4} - \frac{11x}{12L} + \frac{3x^2}{4L^2} - \frac{x^3}{6L^3}\right)e^*_{0,i-1}(t) + \left(\frac{13}{12} + \frac{3x}{4L} - \frac{7x^2}{4L^2} + \frac{x^3}{2L^3}\right)e^*_{0,i}(t) + \ldots$$
$$\left(-\frac{5}{12} + \frac{x}{4L} + \frac{5x^2}{4L^2} - \frac{x^3}{2L^3}\right)e^*_{0,i+1}(t) + \left(\frac{1}{12} - \frac{x}{12L} - \frac{x^2}{4L^2} + \frac{x^3}{6L^3}\right)e^*_{0,i+2}(t) \tag{8.321}$$

$$\dot{m}(x,t)\Big|_{-.5L}^{3.5L} = \left(\frac{11}{12} - \frac{43x}{24L} + \frac{x^2}{L^2} - \frac{x^3}{6L^3}\right)\dot{m}^*_{j-1}(t) + \left(\frac{5}{24} + \frac{23x}{8L} - \frac{5x^2}{2L^2} + \frac{x^3}{2L^3}\right)\dot{m}^*_j(t) + \ldots$$
$$\left(-\frac{1}{6} - \frac{11x}{8L} + \frac{2x^2}{L^2} - \frac{x^3}{2L^3}\right)\dot{m}^*_{j+1}(t) + \left(\frac{1}{24} + \frac{7x}{24L} - \frac{x^2}{2L^2} + \frac{x^3}{6L^3}\right)\dot{m}^*_{j+2}(t) \tag{8.322}$$

The fluxes leaving control volumes i and j can now be found:

$$\rho(t, x = L) = \frac{-\rho^*_{i-1}(t) + 7\rho^*_i(t) + 7\rho^*_{i+1}(t) - \rho^*_{i+2}(t)}{12} \tag{8.323}$$

$$\rho\left(t, x = \frac{3L}{2}\right) = -\frac{1}{24}\rho^*_i(t) + \frac{13}{12}\rho^*_{i+1}(t) - \frac{1}{24}\rho^*_{i+2}(t) \tag{8.324}$$

$$e_0\left(t, x=L\right)=\frac{-e^*_{0,i-1}\left(t\right)+7e^*_{0,i}\left(t\right)+7e^*_{0,i+1}\left(t\right)-e^*_{0,i+2}\left(t\right)}{12} \tag{8.325}$$

$$e_0\left(t, x=\frac{3L}{2}\right)=-\frac{1}{24}e^*_{0,i}\left(t\right)+\frac{13}{12}e^*_{0,i+1}\left(t\right)-\frac{1}{24}e^*_{0,i+2}\left(t\right) \tag{8.326}$$

$$\dot{m}\left(t, x=L\right)=-\frac{1}{24}\dot{m}^*_{j-1}\left(t\right)+\frac{13}{12}\dot{m}^*_{j}\left(t\right)-\frac{1}{24}\dot{m}^*_{j+1}\left(t\right) \tag{8.327}$$

$$\dot{m}\left(t, x=\frac{3L}{2}\right)=-\frac{1}{12}\dot{m}^*_{j-1}\left(t\right)+\frac{7}{12}\dot{m}^*_{j}\left(t\right)+\frac{7}{12}\dot{m}^*_{j+1}\left(t\right)-\frac{1}{12}\dot{m}^*_{j+2}\left(t\right) \tag{8.328}$$

8.5 Numerical Methods Derivations

8.5.1 Linear Convection Equation

Derivations are presented for the first order upwind method and the Lax-Wendroff method as applied to the Linear Convection Equation [16,17].

8.5.1.1 First Order Upwind

The Linear Convection Equation, is shown in differential form in equation (8.329) below.

$$\frac{\partial u}{\partial t}+c\cdot\frac{\partial u}{\partial x}=0 \tag{8.329}$$

The spatial derivative is replaced by a first order upwind approximation, while the time derivative is replaced by the forward Euler approximation.

$$\frac{\partial u}{\partial x} = \frac{u_i^n - u_{i-1}^n}{\Delta x} \tag{8.330}$$

$$\frac{\partial u}{\partial t} = \frac{u_i^{n+1} - u_i^n}{\Delta t} \tag{8.331}$$

Applying (8.330) and (8.331) to (8.329) and rearranging yields the first order upwind method for the Linear Convection equation in (8.332). Note that the equation has been derived with a combined space and time discretization and thus is shown in a fully discrete form.

$$u_i^{n+1} = u_i^n + c\frac{\Delta t}{\Delta x}\left(u_{i-1}^n - u_i^n\right) \tag{8.332}$$

8.5.1.2 Lax-Wendroff

The Linear Convection Equation, is shown in differential form in equation (8.333) below.

$$\frac{\partial u}{\partial t} + c \cdot \frac{\partial u}{\partial x} = 0 \tag{8.333}$$

Differentiating equation (8.333) with respect to time yields:

$$\frac{\partial^2 u}{\partial t^2} + c \cdot \frac{\partial^2 u}{\partial t \partial x} = 0 \tag{8.334}$$

Differentiating equation (8.333) with respect to distance yields:

$$\frac{\partial^2 u}{\partial x \partial t} + c \cdot \frac{\partial^2 u}{\partial x^2} = 0 \tag{8.335}$$

Combining (8.334) and (8.335) yields:

$$\frac{\partial^2 u}{\partial t^2} = c^2 \frac{\partial^2 u}{\partial x^2} \tag{8.336}$$

The Taylor series expansion of u at position x, at time $n+1$ can be shown to be:

$$u_i^{n+1} = u_i^n + \Delta t \left(\frac{\partial u}{\partial t} \right)_i + \frac{\Delta t^2}{2} \left(\frac{\partial^2 u}{\partial t^2} \right)_i + O\left(\Delta t^3 \right) \tag{8.337}$$

Neglecting terms higher than second order and applying (8.333) and (8.336) to (8.337) yields:

$$u_i^{n+1} = u_i^n - c\Delta t \left(\frac{\partial u}{\partial x} \right)_i + \frac{c^2 \Delta t^2}{2} \left(\frac{\partial^2 u}{\partial x^2} \right)_i \tag{8.338}$$

The central difference approximations for the first and second order spatial derivatives can be defined as:

$$\frac{\partial u}{\partial x} = \frac{u_{i+1}^n - u_{i-1}^n}{2\Delta x} \tag{8.339}$$

$$\frac{\partial^2 u}{\partial x^2} = \frac{u_{i+1}^n - 2u_i^n + u_{i-1}^n}{\Delta x^2} \tag{8.340}$$

Applying (8.339) and (8.340) to (8.338) and rearranging yields the Lax-Wendroff method for the Linear Convection equation in (8.341). Note that this method includes a combined space and time discretization, yielding fully discrete equations. The time discretization is known as the Cauchy-Kowalewski time discretization [17].

$$u_i^{n+1} = u_i^n - c\Delta t\left(\frac{\partial u}{\partial x}\right)_i + \frac{c^2\Delta t^2}{2}\left(\frac{\partial^2 u}{\partial x^2}\right)_i \tag{8.341}$$

8.5.2 Linear Euler Equations

Derivations are presented for the first order upwind method and the Lax-Wendroff method as applied to the linear Euler Equations. The upwind method must be supplemented with Flux Vector Splitting in order to properly distinguish between the leftward and rightward traveling waves.

8.5.2.1 First Order Upwind with Flux Vector Splitting

The linear Euler equations are presented in (8.342) and (8.343) below.

$$\frac{\partial \rho}{\partial t} + u_0\frac{\partial \rho}{\partial x} + \rho_0\frac{\partial u}{\partial x} = 0 \tag{8.342}$$

$$\frac{\partial u}{\partial t} + u_0\frac{\partial u}{\partial x} + \frac{c^2}{\rho_0}\frac{\partial \rho}{\partial x} = 0 \tag{8.343}$$

Arranging (8.342) and (8.343) into matrix notation:

$$\frac{\partial U}{\partial t} + A\frac{\partial U}{\partial x} = 0 \tag{8.344}$$

$$U = \begin{bmatrix} \rho \\ u \end{bmatrix} \tag{8.345}$$

$$A = \begin{bmatrix} u_0 & \rho_0 \\ \dfrac{c^2}{\rho_0} & u_0 \end{bmatrix} \tag{8.346}$$

The eigenvalues and eigenvectors of the Jacobian matrix A can be seen to be:

$$Eigenvalues = \lambda = \begin{bmatrix} u_0 - c \\ u_0 + c \end{bmatrix} \tag{8.347}$$

$$Eigenvectors = \begin{bmatrix} \rho_0 \\ -c \end{bmatrix}, \begin{bmatrix} \rho_0 \\ c \end{bmatrix} \tag{8.348}$$

As detailed in [17], the Flux Vector Splitting method divides the eigenvalues into positive and negative values and enters them into diagonal matrices. Thus:

$$\lambda^+ = \begin{bmatrix} 0 & 0 \\ 0 & u_0 + c \end{bmatrix} \tag{8.349}$$

$$\lambda^- = \begin{bmatrix} u_0 - c & 0 \\ 0 & 0 \end{bmatrix} \tag{8.350}$$

Next, define a matrix K containing the eigenvectors:

$$K = \begin{bmatrix} \rho_0 & \rho_0 \\ -c & c \end{bmatrix} \tag{8.351}$$

The split form of the Jacobian Matrices can then be defined as:

$$A^+ = K\lambda^+ K^{-1} = \begin{bmatrix} \frac{u_0 + c}{2} & \frac{\rho_0 (u_0 + c)}{2a} \\ \frac{c(u_0 + c)}{2\rho_0} & \frac{u_0 + c}{2} \end{bmatrix} \tag{8.352}$$

$$A^- = K\lambda^- K^{-1} = \begin{bmatrix} \frac{u_0 - c}{2} & \frac{\rho_0 (c - u_0)}{2c} \\ \frac{c(c - u_0)}{2\rho_0} & \frac{u_0 - c}{2} \end{bmatrix} \tag{8.353}$$

The positive and negative fluxes can thus be defined as:

$$F^+ = A^+ U = \begin{bmatrix} \frac{(u_0 + c)(c\rho + \rho_0 u)}{2c} \\ \frac{(u_0 + c)(c\rho + \rho_0 u)}{2\rho_0} \end{bmatrix} \tag{8.354}$$

$$F^- = A^- U = \begin{bmatrix} \frac{(u_0 - c)(c\rho - \rho_0 u)}{2c} \\ \frac{(c - u_0)(c\rho - \rho_0 u)}{2\rho_0} \end{bmatrix} \tag{8.355}$$

Using the relations defined above, the governing partial differential equations can be re-written as:

$$\frac{\partial \rho}{\partial t}+\left(\frac{u_0+c}{2}\right)\left(\frac{\partial \rho}{\partial x}\right)_+ +\left\{\frac{\rho_0\left(u_0+c\right)}{2c}\right\}\left(\frac{\partial u}{\partial x}\right)_+ +\left(\frac{u_0-c}{2}\right)\left(\frac{\partial \rho}{\partial x}\right)_- +\left\{\frac{\rho_0\left(c-u_0\right)}{2c}\right\}\left(\frac{\partial u}{\partial x}\right)_- =0 \quad (8.356)$$

$$\frac{\partial u}{\partial t}+\left\{\frac{c\left(u_0+c\right)}{2\rho_0}\right\}\left(\frac{\partial \rho}{\partial x}\right)_+ +\left(\frac{u_0+c}{2}\right)\left(\frac{\partial u}{\partial x}\right)_+ +\left\{\frac{c\left(c-u_0\right)}{2\rho_0}\right\}\left(\frac{\partial \rho}{\partial x}\right)_- +\left(\frac{u_0-c}{2}\right)\left(\frac{\partial u}{\partial x}\right)_- =0 \quad (8.357)$$

The spatial partial derivatives with a subscript + can now be discretized using a first order upwind approximation, while those with a – subscript can be discretized using a first order downwind approximation. The time derivative is discretized using a first order Euler time discretization. These steps are left to the reader.

8.5.2.2 Lax-Wendroff

The linear Euler equations are presented in (8.358) and (8.359) below.

$$\frac{\partial \rho}{\partial t}+u_0\frac{\partial \rho}{\partial x}+\rho_0\frac{\partial u}{\partial x}=0 \quad (8.358)$$

$$\frac{\partial u}{\partial t}+u_0\frac{\partial u}{\partial x}+\frac{c^2}{\rho_0}\frac{\partial \rho}{\partial x}=0 \quad (8.359)$$

Differentiating (8.358) and (8.359) with respect to time yields:

$$\frac{\partial^2 \rho}{\partial t^2}+u_0\frac{\partial^2 \rho}{\partial t\partial x}+\rho_0\frac{\partial^2 u}{\partial t\partial x}=0 \quad (8.360)$$

$$\frac{\partial^2 u}{\partial t^2}+u_0\frac{\partial^2 u}{\partial t\partial x}+\frac{c^2}{\rho_0}\frac{\partial^2 \rho}{\partial t\partial x}=0 \quad (8.361)$$

Differentiating (8.358) and (8.359) with respect to distance yields:

$$\frac{\partial^2 \rho}{\partial x \partial t} + u_0 \frac{\partial^2 \rho}{\partial x^2} + \rho_0 \frac{\partial^2 u}{\partial x^2} = 0 \tag{8.362}$$

$$\frac{\partial^2 u}{\partial x \partial t} + u_0 \frac{\partial^2 u}{\partial x^2} + \frac{c^2}{\rho_0} \frac{\partial^2 \rho}{\partial x^2} = 0 \tag{8.363}$$

Combining (8.360) and (8.362) together and (8.361) and (8.363) together yields:

$$\frac{\partial^2 \rho}{\partial t^2} = u_0 \left(u_0 \frac{\partial^2 \rho}{\partial x^2} + \rho_0 \frac{\partial^2 u}{\partial x^2} \right) + \rho_0 \left(u_0 \frac{\partial^2 u}{\partial x^2} + \frac{c^2}{\rho_0} \frac{\partial^2 \rho}{\partial x^2} \right) \tag{8.364}$$

$$\frac{\partial^2 u}{\partial t^2} = u_0 \left(u_0 \frac{\partial^2 u}{\partial x^2} + \frac{c^2}{\rho_0} \frac{\partial^2 \rho}{\partial x^2} \right) + \frac{c^2}{\rho_0} \left(u_0 \frac{\partial^2 \rho}{\partial x^2} + \rho_0 \frac{\partial^2 u}{\partial x^2} \right) \tag{8.365}$$

The Taylor series expansion of ρ and u at position x, at time $n+1$ can be shown to be:

$$\rho_i^{n+1} = \rho_i^n + \Delta t \left(\frac{\partial \rho}{\partial t} \right)_i + \frac{\Delta t^2}{2} \left(\frac{\partial^2 \rho}{\partial t^2} \right)_i + O\left(\Delta t^3 \right) \tag{8.366}$$

$$u_i^{n+1} = u_i^n + \Delta t \left(\frac{\partial u}{\partial t} \right)_i + \frac{\Delta t^2}{2} \left(\frac{\partial^2 u}{\partial t^2} \right)_i + O\left(\Delta t^3 \right) \tag{8.367}$$

Neglecting terms higher than second order and applying (8.364), (8.365), (8.358) and (8.359) to (8.366) and (8.367) yields:

$$\rho_i^{n+1} = \rho_i^n - \Delta t\left(u_0 \frac{\partial \rho}{\partial x} + \rho_0 \frac{\partial u}{\partial x} \right) + \frac{\Delta t^2}{2}\left(\left({u_0}^2 + c^2 \right) \frac{\partial^2 \rho}{\partial x^2} + 2u_0 \rho_0 \frac{\partial^2 u}{\partial x^2} \right) \tag{8.368}$$

$$u_i^{n+1} = u_i^n - \Delta t\left(u_0 \frac{\partial u}{\partial x} + \frac{c^2}{\rho_0} \frac{\partial \rho}{\partial x} \right) + \frac{\Delta t^2}{2}\left(\left({u_0}^2 + c^2 \right) \frac{\partial^2 u}{\partial x^2} + \frac{2u_0 c^2}{\rho_0} \frac{\partial^2 \rho}{\partial x^2} \right) \tag{8.369}$$

The central difference approximations for the first and second order spatial derivatives can be defined as:

$$\frac{\partial \rho}{\partial x} = \frac{\rho_{i+1}^n - \rho_{i-1}^n}{2\Delta x} \tag{8.370}$$

$$\frac{\partial^2 \rho}{\partial x^2} = \frac{\rho_{i+1}^n - 2\rho_i^n + \rho_{i-1}^n}{\Delta x^2} \tag{8.371}$$

$$\frac{\partial u}{\partial x} = \frac{u_{i+1}^n - u_{i-1}^n}{2\Delta x} \tag{8.372}$$

$$\frac{\partial^2 u}{\partial x^2} = \frac{u_{i+1}^n - 2u_i^n + u_{i-1}^n}{\Delta x^2} \tag{8.373}$$

Applying these relations to (8.368) and (8.369) yields the Lax-Wendroff method for the linear Euler equations. Note that this method includes a combined space and time discretization, yielding fully discrete equations. The time discretization is known as the Cauchy-Kowalewski time discretization [17].

$$\rho_i^{n+1} = \rho_i^n - \frac{\Delta t}{2\Delta x}\left(u_0\left(\rho_{i+1}^n - \rho_{i-1}^n\right) + \rho_0\left(u_{i+1}^n - u_{i-1}^n\right)\right) + \ldots$$
$$\frac{\Delta t^2}{2\Delta x^2}\left(\left({u_0}^2 + c^2\right)\left(\rho_{i+1}^n - 2\rho_i^n + \rho_{i-1}^n\right) + 2u_0\rho_0\left(u_{i+1}^n - 2u_i^n + u_{i-1}^n\right)\right) \tag{8.374}$$

$$u_i^{n+1} = u_i^n - \Delta t\left(\frac{u_0}{2\Delta x}\left(u_{i+1}^n - u_{i-1}^n\right) + \frac{c^2}{\rho_0 2\Delta x}\left(\rho_{i+1}^n - \rho_{i-1}^n\right)\right) + \ldots$$
$$\frac{\Delta t^2}{2\Delta x^2}\left(\left({u_0}^2 + c^2\right)\left(u_{i+1}^n - 2u_i^n + u_{i-1}^n\right) + \frac{2u_0c^2}{\rho_0}\left(\rho_{i+1}^n - 2\rho_i^n + \rho_{i-1}^n\right)\right) \tag{8.375}$$

BIBLIOGRAPHY

1. Heywood, J., *"Internal Combustion Engine Fundamentals",* McGraw-Hill, New York, 1988.

2. Ferguson, C., "*Internal Combustion Engines: Applied Thermosciences"*, John Wiley & Sons, Inc., New York, 2001.

3. Stone, R., "*Introduction to Internal Combustion Engines*", Society of Automotive Engineers, Warrendale, Pa, 1999.

4. Guzzella, L., "*Introduction to Modeling and Control of Internal Combustion Engine Systems*" Springer, New York, 2004.

5. Ramos, J., "*Internal Combustion Engine Modeling*", Hemisphere Publishing Corporation, New York, 1989.

6. Blair, G., "*Design and Simulation of Four Stroke Engines*", Society of Automotive Engineers, Warrendale, Pa, 1999.

7. Basshuysen, R., Schafer, F., *"Internal Combustion Engine Handbook: Basics, Components, Systems, and Perspectives",* SAE International, Warrendale, Pa, 2002

8. Glassman, I., *"Combustion"* Academic Press Inc., San Diego, California, 1987.

9. Shapiro, A., "*The Dynamics and Thermodynamics of Compressible Fluid Flow*", John Wiley and Sons, 1977.

10. Moran, M., *"Fundamentals of Engineering Thermodynamics",* John Wiley & Sons, Inc., 2000.

11. Anderson, J.D., "*Modern Compressible Flow: with Historical Perspective*", McGraw-Hill, 2003.

12. Winterbone, D., Pearson, R., "*Theory of Engine Manifold Design: Wave Action Methods for IC Engines*". Professional Engineering Publishing, 2000.

13. Benson, R., "*The Thermodynamics and Gas Dynamics of Internal Combustion Engines*", Oxford University Press, New York, 1982.

14. Anderson, J.D., "*Computational Fluid Dynamics*", McGraw-Hill, 2002.

15. Leveque, and R., "*Numerical Methods for Conservation Laws*", Birkhauser Verlag, 1992.

16. Hirsch, C., "*Numerical Computation of Internal and External Flows: The Fundamentals of Computational Fluid Dynamics*", Elsevier, 2007.

17. Laney, C., "*Computational Gasdynamics*", Cambridge University Press, 1998.

18. Toro, E., "*Riemann Solvers and Numerical Methods for Fluid Dynamics*", Springer, 1999.

19. Doebelin, E., "*System Dynamics: Modeling, Analysis, Simulation, Design*" Marcel Dekker, Inc., 1998.

20. Doebelin, E., "*System Modeling and Response: Theoretical and Experimental Approaches*", John Wiley and Sons, 1980.

21. Karnopp, D., Margolis, R., Rosenberg, R., "*System Dynamics: A Unified Approach*". John Wiley and Sons, 1990.

22. Palm III, W., "*System Dynamics*" McGraw-Hill, 2005.

23. Close, C., "*Modeling and Analysis of Dynamic Systems*", John Wiley and Sons, 2002.

24. Brown, F., "*Engineering System Dynamics: A Unified Graph-Centered Approach*", CRC Press Taylor and Francis Group, 2007.

25. Ogata, K., "*Modern Control Engineering*". Prentice Hall, 1990.

26. Guezennec, Y., ME 730 Course Notes, The Ohio State University, 2005.

27. Rizzoni, G., ME 781 Course Notes, The Ohio State University, 2006.

28. Lee, B., "Methodology for the Static and Dynamic Model Based Engine Calibration and Optimization" Ph.D. Dissertation, The Ohio State University, 2005.

29. Dawson, J., "An experimental and Computational Study of Internal Combustion Engine Modeling for Controls Oriented Research" Ph.D. Dissertation, The Ohio State University, 2005.

30. Canova, M., “Fluid Systems Dynamics Modeling for Control: Internal Combustion Engine Studies”, Ph.D. Dissertation, University of Parma, 2006.

31. Chiodi, M., “An innovative 3-D-CFD-Approach towards Virtual Development of Internal Combustion Engines” Ph.D. Dissertation, University of Stuttgart, 2010.

32. Gamma Technologies, GT-Power. http://www.gtisoft.com.

33. CD-adapco, STAR-CD. http://www.cd-adapco.com.

34. Khalighli, B., El Tahry, S.H. Haworth, D.C., and Huebler, M.S., “Computation and Measurement of Flow and Combustion in a Four-Valve Engine with Intake Variations”, SAE Paper 950287, 1995.

35. Kuo, T-W. and Chang, S., “Three-dimensional Steady Flow Computations in Manifold-Type Junctions and a Comparison with Experiment”, SAE Paper 932511, 1993

36. Zeleznik, F., B. McBride, “Modeling the Internal Combustion Engine”, NASA Reference Publication 1094, 1985.

37. Arsie, I., C. Pianese, G. Rizzo, M. Gambino, “Validation of a Thermodynamic Model for Spark Ignition Engines Oriented to Control Applications”, 3rd International Conference on “Internal Combustion Engines: Experiments and Modeling” Capri, September, 1997.

38. Ricardo (WAVE), http://www.ricardo.com.

39. Watson, N., “Turbocharging the Internal Combustion Engine”, John Wiley and sons, New York, 1982.

40. Powell, B., “A Dynamic Model for Automotive Engine Control Analysis” Proc. Of 18th IEEE Conference on Decision and Control pp.120-126, 1979.

41. Dobner, D., “A Mathematical Engine Model for Development of Dynamic Engine Control”, SAE Technical Paper 800054.

42. Dobner, D, “An Engine Model for Dynamic Engine Control Development”, ASME Paper No. WA4-11:15, 1986.

43. Cook J., Powell, B., “Modeling of an Internal Combustion Engine for Control Analysis”, Proceedings of the American Control Conference, 1987.

44. B. K. Powell and J. A. Cook, “Nonlinear low frequency phenomenological engine modeling and analysis,”*Proceedings of the American Control Conference,* pp.332-340, Minneapolis, MN, June, 1987.

45. J. J. Moskwa and J. K Hedrick, “Modeling and validation of automotive engines for control algorithm development,” Advanced Automotive Technologies-1989, pp.237-247, ASME DSC-vol.13.

46. Delosh, R., Brewer, K., Buch, L., Ferguson, T., and Tobler, W., “Dynamic Computer Simulation of a Vehicle with Electronic Engine Control”, SAE Paper 810447, 1981.

47. Hendricks, E. and Sorenson, S. C., “Mean Value Modeling of Spark Ignition Engines”, SAE Paper 900616, 1990.

48. Hendricks, E. and Vesterholm, T., “The Analysis of Mean Value SI Engine Models”, SAE Paper 920682, 1992.

49. Stefanopoulou, A., Cook, J., Freudenberg, J., Grizzle, J., Haghgooie, M., and Szpak, P., “Modeling and Control of a Spark Ignition Engine with Variable Cam Timing”, Proceedings of the American Control Conference, pp. 2576-2581, 1995.

50. Baruah, P., “A Simulation Model for Transient Operation of Spark-Ignition Engines”, SAE Paper 900682, 1990.

51. Hendricks, E., Sorenson, S., “SI Engine Controls and Mean Value Engine Modeling”, SAE Paper 910258, 1991.

52. Moskwa, J., Hedrick, K., “Modeling and Validation of Automotive Engines for Control Algorithm Development”. ASME Journal of Dynamic Systems, Measurement and Control, 1992.

53. Hendricks, E., Chevalier, A., Jensen, M., Sorenson, S., Trumpy, D., and Asik, J., “Modeling of the Intake Manifold Filling Dynamics”, SAE Paper 960037, 1996.

54. Hendricks, E., “Engine Modeling for Control Applications: A Critical Survey”, MECCANICA, vol.32, no.5, Kluwer Acad.Publ., October 1997.

55. Fons, M., Muller, M., Chevalier, A., Vigild, C., Hendricks, E., and Sorenson, S., “Mean Value Engine Modeling of an SI Engine with EGR”, SAE Paper 1999-01-0909, 1999.

56. Chevalier A., Muller M., Hendricks E., “On the Validity of Mean Value Engine Models During Transient Operation”, SAE paper 2000-01-1261.

57. Andersson, P., Eriksson, L., Nielsen, L., “Modeling and Architectural Examples of Model Based Engine Control”, *Proceedings of the* 2*nd Conference on Computer Science and System Engineering, 19*99.

58. Stefanopoulou, A., Cook, J., Grizzle, J., and Freudenberg, J., “Control-Oriented Model of a Dual Equal Variable Cam Timing Spark Ignition Engine”, ASME Journal of Dynamic Systems, Measurement, and Control, Vol. 120, pp. 257-266, 1998.

59. Ashhab, M., Stefanopoulou, A., Cook, J., Levin, M., “Control-Oriented Model for Camless Intake Process (Part I)”, ASME Journal of Dynamic Systems, Measurement, and Control, Vol. 122, pp. 122-130, 2000.

60. Grizzle, J., Cook, J., Milam, W., “Improved Cylinder Air Charge Estimation for Transient Air Fuel Ratio Control”, ASME Journal of Dynamic Systems, Measurement and Control, Vol. 126, 2004.

61. J. J. Moskwa and M. Kao. Turbocharged Diesel Engine Modeling for Nonlinear Engine Control and State Estimation. *ASME Journal of Dynamic Systems, Measurement and Control, 1995*.

62. Guzzella, L.. Amstutz, A., “Control of Diesel Engines”, IEEE Control Systems Magazine, Vol. 8, No. 9, 1998.

63. Fekete, N., Nester, U., Gruden, I., Powell, J., “Model-Based Air-Fuel Ratio Control of a Lean Multi-Cylinder Engine”, SAE Paper 950846, 1995.

64. Turin, R., Geering, H., “Model Based Adaptive Fuel Control in an SI Engine”, SAE Paper 940374, 1994.

65. Canova, M., “A Development and Validation of a Control-Oriented Library for the Simulation of Automotive Engines”, International Journal of Engine Research, Vol. 5, No. 3, 2004.

66. Canova, M., Midlam-Mohler, S., Guezennec, Y., Rizzoni, G., "Mean Value Modeling and Analysis of HCCI Diesel Engines with External Mixture Formation", ASME Journal of Dynamic Systems, Measurement and Control, Vol. 131, No. 11, 2009.

67. Canova, M., Fiorani, M., Gambarotta, A., Tonetti, M., “A Real-Time Model of a Small Turbocharged Multijet Diesel Engine: Application and Validation”, 7th International Conference on Engines for Automobile, Italy.

68. Canova, M., Gambarotta, A., “Automotive Engine Modeling for Real-Time Control Using an Object-Oriented Simulation Library”, International Conference on Control and Diagnostics in Automotive Applications, 2003.

69. Berta, G., Canova, M., Casoli, P., Gambarotta, A., “A Control-Oriented Model for the Simulation of Turbocharged Diesel Engines”, 2nd Intl. Workshop on Modeling, Emissions and Control of Automotive Engines, 2002.

70. Ko, J., Guezennec, Y., Radwan, A., Rizzoni, G. and Choi, W.-C., “A Rapid Engine Prototyping Methodology: Linking Geometry, Flow Field, Combustion, Performance and Control”, 2001 ASME Symposium on Advanced Automotive Technologies, 2001.

71. Lee, B., Guezennec, Y., G., Rizzoni, G., Trombley, D. and Liu, S., “Development and Validation of Control-Oriented Model of an SIDI Engine”, Proc. 2003 ASME IMECE, Symposium on Advanced Automotive Technologies, 2003.

72. M. Hopka, D. Upadhyay, Y. Guezennec, G. Rizzoni, “Identification of a Mean-Value Model for a Modern Diesel Engine for Control Design”, Proc. 2003 ASME IMECE, Symposium on Advanced Automotive Technologies, 2003.

73. Canova, M, Garzarella, L., Ghisolfi, M., Midlam-Mohler, S., Guezennec, Y. and Rizzoni, G., “A Mean-Value Model of a Turbo-Charged HCCI Diesel Engine with External Mixture Formation, 7th International Conference on Engines for Automobiles, 2005.

74. Smith, L., T. Fickenscher, R. Osborne, “Engine Breathing – Steady Speed Volumetric Efficiency and Its Validity under Transient Engine Operation” SAE Paper: 1999-01-0212.

75. Miotti, A., R. Scattolini, A. Musi, C. Siviero. “Integrated Breathing Model and Multi-Variable Control Approach for Air Management in Advanced Gasoline Engine” SAE Paper: 2006-01-0658.

76. Dudek, K., Montello, B., Meyer, J., Midlam-Mohler, S., Guezennec, Y., Yurkovich, S., “Rapid Engine Calibration for Volumetric Efficiency and Residuals by Virtual Engine Mapping”, International Congress on Virtual Power Train Creation, 2007.

77. Lee, B. and Guezennec, Y., “Advanced Math-Based Engine Calibration and Control System Design”, Proc. FISITA ’06, 2006.

78. Fiaschetti, J., Narasimhamurthi, N., “A Descriptive Bibliography of SI Engine Modeling and Control”, SAE Paper: 950986, 1995.

79. Moraal P., Grizzle J., Cook J., An Observer Design for Single-Sensor Individual Cylinder Pressure Control, 32nd IEEE Conference on decision and control, 1993.

80. Benson, R., R., Gar., and D. Woollatt, “A Numerical Solution of unsteady Flow Problems”, International Journal of Mechanical Science, Vol. 6, pp 117-144, 1964.

81. Benson, R., Annand, W., Baruah, P., “A Simulation Model Including Intake and Exhaust Systems for a Single Cylinder Four-Stroke Cycle Spark Ignition Engine”, International Journal of Mechanical Science, Pergamon Press, Vol. 17, pp. 97-124, 1975.

82. A. Onorati. “Prediction of the Acoustical Performances of Muffling Pipe Systems by the Method of Characteristics”. Journal of Sound and Vibration 171(3), 1994.

83. D'Errico G. and Onorati A, (2006), “Thermo-Fluid Dynamic Modelling of a Six-Cylinder Spark Ignition Engine with a Secondary Air Injection System”, International Journal of Engine Research, Vol. 7, No 1, pp. 1-16.

84. Pearson, R., Winterbone, D., “A Rapid Wave Action Simulation Technique for Intake Manifold Design”, SAE Paper 900676, 1990.

85. Winterbone, D., Pearson, R., “The Simulation of Gas Dynamics in Engine Manifolds Using Nonlinear Symmetric Difference Schemes”, Proceedings of the Institution of Mechanical Engineers, Part C: Journal of Mechanical Engineering Science, Vol. 211, No. 8, 1997.

86. Morel, T., Silvestri, J., Goerg, K., Jebasinski, R., “Modeling of Engine Exhaust Acoustics” SAE Paper: 1999-01-1665.

87. Riemann, B. "*Gesammelte Mathematische Werke*", Second Edition Teubner, Leipzig, 1892.

88. P. Lax and B. Wendroff. “Systems of Conservation Laws”, Communications of Pure and Applied Mathematics, Vol 13, 1960.

89. MacCormack, R., “The Effect of Viscosity in Hypervelocity Impact Cratering”, AIAA Paper, 69-354, 1969.

90. Courant, R., Friedrichs, K., Lewy, H., “On Partial Difference Equations of Mathematical Physics,” IBM Journal 11,215-234, 1967 (English translation of the original work, “Uber die Partiellen Differenzengleichungen der Mathematischen Physik,” Math. Ann. 100, 32-74, 1928).

91. Morel, T., R. Keribar, J. Silvestri, Swahiduzzaman, “Integrated Engine/Vehicle Simulation and Control” SAE Paper: 1999-01-0907.

92. Ciesla, C., R. Keribar, T. Morel, “Engine/Powertrain/Vehicle Modeling Tool Applicable to All Stages of the Design Process” SAE Paper: 2000-01-0934.

93. Stobart, R., A. May, B.J. Challen, T. Morel, “New Tools for Engine Systems Development” IFAC Annual Reviews in Control 23 (1999) 106-116.

94. P. Bromnick, “Development of a Model Predictive Controller for Engine Idle Speed Using CPower” SAE Paper 1999-01-1171.

95. Hoops, C., “Development of Procedures and Tools for Calibration of I.C Engine Combustion Models” B.S. Honors Thesis, The Ohio State University, 2009.

96. Montgomery, D.C. “Design and Analysis of Experiments” John Wiley and Sons, 2000.

97. Lee, B., Y. Guezennec, *Rapid Engine Mapping and Modeling*, U.S. Patent 2007/0265805 A1, 2007.

98. S. Gordon and B. J. McBride, “Computer Program for Calculation of Complex Chemical, Equilibrium Composition, Rocket Performance, Incident and Reected Shocks, and Chapman-Jouguet Detonations", NASA publication SP-273, 1971.

99. JANAF Thermochemical Tables", U.S National Bureau of Standards Publications NSRDS-NBS 37, June 1971.

100. Chen S. K., and Flynn, P. F., “Development of Single Cylinder Compression Ignition Research Engine”, SAE Paper 650733

101. He, X., Liu, S., and Asada, H., “Modeling of Vapor Compression Cycles for Multivariable Feedback Control of HVAC Systems,” ASM.E J. of Dynamic Systems, Measurement, and Control, Vol. 119, pp. 183-191, June 1997.

102. Gruhle, W.D., and Isermann, R., “Modeling and Control of a Refrigerant Evaporator,” ASME Journal of Dynamic Systems, Measurement, and Control, Vol. 107, pp. 235-239, June 1980.

103. Aalto, H., “Transfer Functions for Natural Gas Pipeline Systems”, Proceedings of the IFAC 17th World Congress, 2008.

104. Gravdahl, J., Egeland, O., “Centrifugal Compressor Surge and Speed Control”, IEEE Transactions on Control systems Technology, Vol. 7, No. 5, 1999.

105. Chapman, K., Abbaspour, M., “Virtual Pipeline System Testbed to Optimize the U.S. Natural Gas Transmission Pipeline System”, Technology Status Assessment Report, The Department of Energy Strategic Center for Natural Gas, June 2002.

106. Mohitpour, M., Thompson, W., Asante, B., “The Importance of Dynamic Simulation on the Design and Optimization of Pipeline Transmission Systems”, Proceedings of the International Pipeline Conference, 1996.

107. Osiadacz, A., “Different Transient Models- Limitations, Advantages and Disadvantages”, 28th Annual Meeting PSIG (Pipeline Simulation Interest Group), 1996.

108. Zhou, J., Adewumi, M., “Simulation of Transient Flow in Natural Gas Pipelines”, 27th Annual Meeting PSIG (Pipeline Simulation Interest Group), 1995.

109. Chapman, K., Abbaspour, M., “Nonisothermal Transient Flow in Natural Gas Pipeline”, Journal of Applied Mechanics, Vol. 75, Issue 3, 2008.

110. Heath, M., Blunt, J., “Dynamic Simulation Applied to the Design and Control of a Pipeline Network”, J. Inst. Of Gas Engineers, Vol. 9, pp. 261, 279, 1969.

111. Wylie, E., Stoner, M., Streeter, V., “Network System Transient Calculation by Implicit Methods”, Soc. Pet. Eng. J., Vol. 3, pp 356, 362, 1971.

112. Emmons, H., Pearson, C., Grant H., “Compressor Surge and Stall Propagation”, Trans. ASME, vol. 77, pp. 455–469, 1955.

113. Gu, G., Sparks, A., Banda, S., “An Overview of Rotating Stall and Surge Control for Axial Flow Compressors”, IEEE Transactions on Control Systems Technology, Vol. 7, No. 6, 1999.

114. Greitzer, E., “Surge and Rotating Stall in Axial Flow Compressors”, Part I, II. Journal of Engineering for Power, 98:190–198, 1976.

115. Moore F., Greitzer, E., “A Theory of Post-Stall Transients in Axial Compressors - Part I: Development of the Equations” ASME J. Engr. Gas Turbines Power, vol. 108, pp. 68–76, 1986.

116. Gravdahl, J., Egeland, O., “Centrifugal Compressor Surge and Speed Control”, IEEE Transactions on Control systems Technology, Vol. 7, No. 5, 1999.

117. Gravdahl J., Egeland, O., “Compressor Surge and Rotating Stall: Modeling and Control”, Advances in Industrial Control, Springer-Verlag, London, 1999.

118. Weeks, R., Moskwa, J., “Automotive Engine Modeling for Real-Time Control Using MATLAB/SIMULINK”, SAE Paper: 950417, 1995.

119. Cipollone, R., Sciarretta, A., “The Quasi-Propagatory Model: A New Approach for Describing Transient Phenomena in Engine Manifolds”, SAE Paper 2001-01-0579, 2001.

120. Cipollone, R., Martella, L., Scarpone, L., Valente, R., “A New Modeling to Predict the Fluid Dynamic Transient Phenomena in ICE Ducts”, SAE Paper 2008-01-2389, 2008.

121. Karnopp, D., “Pseudo Bond Graphs for Thermal Energy Transport”, Journal of Dynamic Systems, Measurement and Control, Vol. 100, 1978.

122. Margolis, D., “Bond Graph Fluid Line Models for Inclusion with Dynamic Systems Simulation”, Journal of the Franklin Institute, Vol. 308, No. 3, 1979.

123. Karnopp, D., “State Variables and Pseudo Bond Graphs for Thermofluid Systems”, Journal of Dynamic Systems, Measurements and Control, Vol. 101, 1979.

124. Tan, J., Stelson, K., Janni, K., “Compressible-Flow Modeling with Pseudo Bond Graphs”. Journal of Dynamic Systems, Measurements and Controls, Vol. 116, 1994.

125. Strand, K., Engja. H., “Bond Graph Interpretation of One-Dimensional Fluid Flow”. Journal of the Franklin Institute 328, 1991.

126. Brown, F., “Non-iterative evaluation of multiphase thermal compliances in bond graphs”, I MECH E Journal of Systems and Control Engineering, 2001.

127. Margolis, D., “Bond Graphs for 1-Dimensional Duct Flows Using Nonlinear Finite Lumps”. 2003 International Conference on Bond Graph Modeling and Simulation, 2003.

128. Brown, F., “Kinetic Energy in Convection Bond Graphs” International Conference on Bond Graph Modeling, 2003.

129. Currie, I., “*Fundamental Mechanics of Fluids*” Marcel Dekker, Inc, New York, 2003.

130. Woschni, G., “A Universally Applicable Equation for the Instantaneous Heat Transfer Coefficient in the Internal Combustion Engine” SAE Paper 670931.

131. Bargende, M. “Ein Gleichungsansatz zur Berechnung der instationären Wandwärmeverluste im Hochdruckteil von Ottomotoren” Dissertation, TH Darmstadt, 1990.

132. Moler, C., “Numerical Computing with Matlab” Society for Industrial and Applied Mathematics, 2004.

133. Chatterjee, A., “An Introduction to the Proper Orthogonal Decomposition”, Current Science Vol. 78, No. 7, 10, 2000.

134. Kerschen, G., Golinval, J., Vakakis, A., Bergman, L., “The Method of Proper Orthogonal Decomposition for Dynamical Characterization and Order Reduction of Mechanical Systems: An Overview”, Nonlinear Dynamics 41, 147–169, 2005.

135. Feeny, B., Kappagantu, R., On the Physical Interpretation of Proper Orthogonal Modes in Vibration, Journal of Sound and Vibration, Volume 211, Issue 4, 9, Pages 607-616, 1998.

136. Han, S., Feeny, B., “Application of Proper Orthogonal Decomposition to Structural Vibration Analysis”, Mechanical Systems and Signal Processing, Vol. 17, No 5, pp. 989-100, 2003.

137. Berkooz, G., Holmes, P., and Lumley, J., “The Proper Orthogonal Decomposition in the Analysis of Turbulent Flows” Annual Review of Fluid Mechanics, Vol. 25, 1993, pp. 539.

138. LeGresley, P., Alonso, J., “Investigation of Nonlinear Projection for POD Based Reduced Order Models for Aerodynamics" AIAA Paper 2001-0926, 2001.

139. Cazemier, W., Verstappen, R., Veldman, A., “Proper Orthogonal Decomposition and Low-Dimensional Models for Driven Cavity Flows”, Physics of Fluids, Vol. 10, No. 7, 1998.